UNIVERSITÀ DEGLI STUDI DI NAPOLI FEDERICO II

International PhD Program on:

Novel Technologies for Materials, Sensors and Imaging

XXIII cycle

Realization and characterization of silicon nitride thin films embedding Si nanoparticles

Emilia Maria Esposito

Tutor: Dr. Lucia Vittoria Mercaldo

This thesis describes the research activity of E. M. Esposito during the three years of the International PhD program on Novel Technologies for Materials, Sensors and Imaging (TIMSI – XXIII cycle) offered by University “Federico II” of Napoli (Italy). The Scholarship was financed by ENEA under a signed Agreement with the University. The activity was performed at ENEA - Portici Research Center in the “Photovoltaic Technologies Section” (now “Portici Technical Unit”), supported by the Italian Ministry of Education, University and Research through FIRB Fotoenergia RBIP06N57B project and by the Italian Ministry of Economic Development in the framework of the Operating Agreement with ENEA for Research on the Electric System.

to *my little Annamaria*

Contents

Introduction

A great deal of interest is nowadays focused on nanostructured materials. Production and manipulation of nanoparticles in many cases is still an art and the exciting results obtained in many laboratories are waiting for new technological solutions to be reproduced on a large, economically convenient, scale. The efforts towards the development of efficient production, manipulation, and characterization methods in view of possible applications should not lead to overlook the fact that nanostructures and nanostructured materials are very interesting from a fundamental point of view and that a basic comprehension is a necessary background for development of any nano-technology.

The complexity of the nano-physics is due to its dimensional scale. Indeed, the nanometer scale induces drastic changes in the physical behavior of matter. The properties of low dimension structures depend on the number of their constituents: by controlling the size of the nanoparticles one can change the electronic, optical, structural and chemical characteristics of an aggregate. Moreover, by assembling nanostructures, one can produce a material with novel functional and structural properties.

In particular silicon nanoparticles embedded in dielectric matrix have received great attention over the last ten years for possible optoelectronic applications. Much interest is focused on silicon nanostructures because of their emission properties in the visible range at room temperature, which could lead to promising memory applications and to future generation optoelctronic devices directly integrated into silicon chips. Indeed, even if bulk silicon has an indirect optical gap and low PL efficiency, significant light emission is observed from low-dimensional silicon, where the selection rules for optical transitions, deriving from translational symmetry, are broken, and at the same time non-radiative rates are reduced. Moreover, due to quantum confinement, the enlargement of the gap moves the light emission to the visible range.

Along with the emission properties, the absorption of Si nanostructures might prove useful. The possibility of engineering new materials with tailored band gap, which absorb photons in dedicated energy ranges, by assembling Si quantum dots within appropriate dielectric matrixes, can be exploited in the photovoltaic field, to implement the so-called "third generation" tandem solar cells [the structure, proposed by Green at UNSW (Australia), is presented in chapter 1]. The tandem approach directly addresses the fundamental loss mechanisms in conventional single band-gap solar cell, namely the inability to absorb photons with energies lower than the band-gap and the losses by thermalisation of the photons with energy exceeding the band-gap; and the proposed structure has the advantage of being entirely made of silicon and its dielectric compounds, all abundant and non-toxic elements.

Besides the other possible applications of such interesting material class, this work configures itself right in the framework of the research and development activity, carried out at ENEA - Portici Research Center in the "Thin-film Si solar cells" group, on nanostructured materials for new generation photovoltaics. In order to realize a working all-silicon tandem cell, quantum confinement in silicon nanoparticles (that could be both amorphous or crystalline) needs to be achieved. This means that certain aspects of the quantum dot material need to be demonstrated including control of dot size, band-gap control, enhanced optical absorption and adequate electronic transport. Once these material properties are established, the next step would be the formation of a working quantum dot solar cell involving doping or some other rectification mechanism. Given a working quantum dot cell, the final step would involve the interconnection of cells, likely through a tunnelling layer. Needless to say the path to a working all-silicon tandem cell based on silicon quantum dots is a challenging one.

As material system, silicon nitride has been selected as host matrix in this work. Different paths have been followed. First of all the possibility of producing Si nanoparticles in silicon nitride thin films in-situ via PECVD by choosing appropriate deposition regimes has been investigated. This is a particularly promising route for the evident advantage of possible use of low

cost substrates and classical thin film silicon solar cell architecture. At the same time we have followed a slightly more conventional (and somewhat safer) path that requires a post-deposition annealing step to induce Si precipitation within the Si-rich dielectric film. In this case we have explored the possibility of reducing temperature and duration of the treatments with respect to literature values.

From the characterization point of view, the work focuses on some of the fundamental requirements for achieving an all silicon tandem solar cell. The basis for this approach is quantum confinement in silicon quantum dots. In order to verify quantum confinement, it is necessary to demonstrate a correlation between structural and optical properties of silicon nanoparticles. Experimentally, one of the primary ways to shows this correlation is with size dependent photoluminescence. Therefore, a lot of effort has been put into investigating the mechanisms governing the photoluminescence of the fabricated materials.

Summarizing, the objectives of this thesis can be so itemized:

1. To investigate convenient and reliable formation of silicon nanoparticles in silicon nitride films.
2. To investigate the underlying photoluminescence mechanism for silicon nanoparticles in silicon nitride.
3. To improve upon the characterisation of silicon nanoparticles embedded in silicon nitride (especially through non-destructive techniques, like Raman spectroscopy).

The manuscript is organized as follows:

- In chapter 1, a brief introduction to possible applications of the proposed material system for microelectronics, photonics and photovoltaics is given.
- Chapter 2 reviews key effects of reduced dimensionality with particular emphasis on the case of Si nanoparticles in silicon nitride. Also, appropriate characterization techniques (photoluminescence, optical absorption, FTIR, Raman spectroscopy, and EFTEM) are discussed and details on the conditions used in our experiments are given.

- Chapter 3 is dedicated to as-grown SiN_x thin films deposited by PECVD. In particular possible spontaneous growth of Si nanoparticles is investigated. The effect of some processing parameters on structural and optical properties of the films is reported. In particular photoluminescence properties are deeply investigated at different excitation energies and temperatures.
- In chapter 4 the annealing effects (temperature range 500 – 1100°C) are studied. The evolution of Raman, FTIR, room temperature photoluminescence, and optical absorption spectra has been investigated and results from EFTEM analysis are reported. Also, an extensive Raman analysis has been performed, allowing us to point out the significant potentialities of this technique when investigating Si nanoparticles as opposed to destructive and time consuming TEM.
- Finally, the main findings of this thesis are highlighted in the conclusions.

CHAPTER 1

Silicon quantum dots applications

Nanoparticles are of great scientific interest as they are effectively a bridge between bulk materials and atomic or molecular structures. A bulk material has constant physical properties regardless of its size, but at the nano-scale this is often not the case. Size dependent properties are present such as quantum confinement in semiconductor particles, surface Plasmon resonance in some metal particles and super paramagnetism in magnetic materials. When a semiconductor structure is reduced to nanometric sizes (1 – 10 nm), the electron and the hole become spatially confined, and cannot be described any more by planar wave-functions, but as a superposition of them, their wave-functions becoming wave-packets. Moreover, due to the boundary conditions, only certain wave-functions with precise wavelengths can be supported by the material. Therefore the energy of the confined particles becomes quantized. In addition, since the position of the particles can be determined with less indetermination with respect to the bulk, as a result of the Heisenbergs uncertainty principle, the momentum of the particles suffers a greater indetermination. This determines an increase in the minimum energy level available to the particles. Indeed, in nanostructured silicon, both the electron and the hole are characterized by higher energies, thus producing an increase of the nanocrystal energy-gap with respect to bulk silicon.

The study of nanostructured materials and in particular the analysis of silicon quantum dots (Si-QDs) embedded in dielectric matrix is important, given the possibility to exploit this systems to obtain new functions in novel devices for microelectronics [1, 2], photonics [3] and photovoltaics, such as nanocrystal

memories, silicon based light emitting devices and new materials with engineered bandgap.

1.1 Si quantum dots for memory application

The ability to embed Si nanostructures in dielectric matrix, in particular in Si-based material, is an important achievement, given the possibility to exploit this system to obtain new functions for the realization of high-scaled integrated circuits [1, 2, 4, 5], in the so-called Very Large Scale Integration (VLSI) technology. Until now, this world has lived on the basis of a continuous evolution and upgrading of technologies which have consolidated a great maturity and understanding in the years, such as oxidation, ion implantation, self-aligned silicide processes, intermediate dielectrics, metallization, etc. However, now VLSI has entered in the nanotechnology era and the feature sizes decrease about every two years by a factor 0.7 from one generation to the following. The trend of MOSFET scaling coupled with size facing fundamental physical limits has implied a new approach, going from an evolutionary to a revolutionary method. This is accelerating the introduction of new technologies that include both new materials and advanced MOSFET structures. A particular challenge is represented by the scalability of non volatile memories (NVM) [6], which imposes additional constraints on process integration and structure design, since NVM structures, that require relatively high voltages must be incorporated into CMOS technology that works at low voltage. Typically, non volatility is achieved by storing and sensing the charge on a floating gate (see fig. 1.1). The dielectric between the floating gate and the control gate (the so called ONO, acronym of oxide-nitride-oxide stack) must scale with the tunnel dielectric to maintain adequate coupling to the control gate. The tunnel dielectric must be thin enough to allow charge transfer to the floating gate at reasonable voltage levels and thick enough to avoid charge loss when in read or off modes.

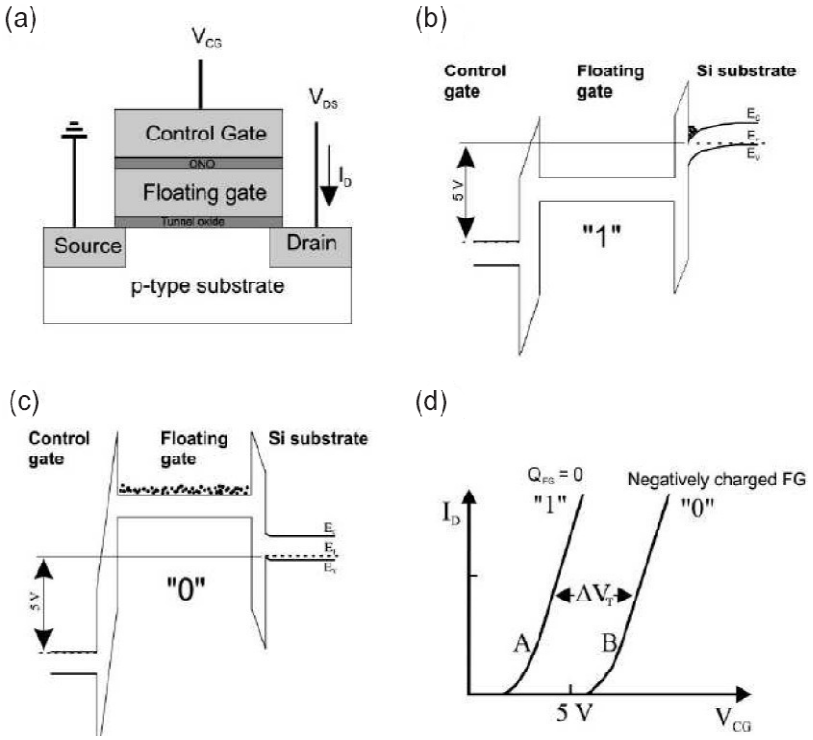

Figure 1. 1 - Schematic structure and working principle of a non-volatile semiconductor memory (NVM) cell: the Flash. **(a)** Cell structure, i.e. an n-MOSFET with the gate dielectric containing a floating gate, electrically completely insulated from the environment. **(b), (c)** Charge states of the floating gate (empty or filled), which in the simplest versions of NVMs are the two logic states of the bit. In this case a single cell is a bit. **(d)** Sensing of the floating gate charge state, performed by simply measuring the drain current under well defined bias conditions.

The aggressive scaling of the Flash devices seen so far [7] is pushing this technology towards a wall made of multiple technological key issues. Among these, the reliability constraints, in particular the requirement of 10-year non-volatility, is of primary importance for both high-density NVMs (stand-alone) and for NVMs integrated with logic (the so-called embedded NVMs), widely used in portable consumer electronics (mobile phones, mp3 players, digital photography, USB drivers), automotive, and other digital applications. Even in the present Flash memories, ensuring non-volatility for all bits after program / erase cycling is a challenge from the view point of manufacturing and yield. The finite probability of having a cluster of two or three defects in the tunnel

oxide, producing a huge local increase of the tunnel current (namely, Stress Induced Leakage Current, often indicated by its acronym, SILC), determines the anomalous failure bits, which are widely recognized as the most important concern in Flash devices. The amplitude of the SILC increases when the tunnel oxide is thinned, limiting the oxide scaling. To extend Flash scalability, existing research efforts are exploring a variety of basic memory mechanisms [7, 8, 9, 10]. These mechanisms include charge isolated by surrounding dielectrics, charge held in place by Coulomb blockade potentials, chemical phenomena, magnetic phenomena, and material phase changes. Among them, the use of discrete-trap storage nodes in conventional Flash memory technology has been invoked as one of the key items for Flash memories. The basic idea of the discrete-trap mechanism is to replace the floating gate (FG) by many discrete trapping centres, as illustrated in fig. 1.2.

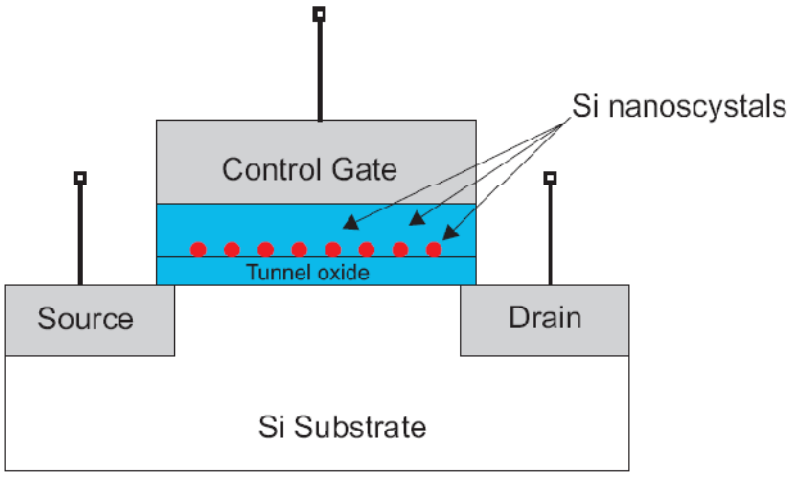

Figure 1. 2 – Sketch of a nanocrystal memory.

1.2 Si quantum dots for optoelectronics devices

Silicon microphotonics is a rapidly growing technology which tries to merge on a single chip photonics and silicon microelectronic components [11]. Silicon is by far the most suitable material for microelectronics. Indeed, it is an

abundant element, its crystallinity is unparalleled by III-V composite materials, and it has very good electrical, thermal and mechanical stability. Anyway for a long time, silicon has been considered unsuitable for optical application, due to the indirect nature of its electronic bandgap. Indeed, once an electron-hole pair is created inside bulk silicon, the radiative recombination producing a 1.1 eV photon necessitates of a phonon in order to conserve crystal momentum. Hence the emission of a photon is a three-particles process (electron, hole and phonon) and is characterized by very small rates, bringing to radiative lifetimes of the order of ~ 1 ms. This is too long if compared to the recombination times of the order of μs or even ns characterizing some non-radiative transitions. In order to solve this problem, many routes have been followed. Among these, silicon based nanostructured crystals have shown great potentialities. In fact, beside the increase of the nanocrystal energy-gap, another effect of quantum confinement is the increase in the probability associated with an optical transition. Indeed, due to the reduced size, the translational symmetry of the system is no more satisfied and, as a consequence, the crystal momentum is no more a good quantum number. This allows for vertical, direct band to band, no-phonon transition to become more probable [12]. Moreover, the density of states for system of decreasing dimensionality becomes more and more atomic-like as far as the number of dimensions involved in the confinement is increased. Going from three-dimensional to zero-dimensional (quantum dots) systems, the density of states tends to resemble the Diracs delta function, producing an increase in the probability of a photon to be emitted in a exciton recombination process. For this aspect, Si nanocrystals seem to be the most promising candidates for optical application.

Beside the theoretical expectation, the main limiting step of the silicon based technology seems to be represented by the absence of an efficient Si light source. In the last decade, an intense research activity has been devoted towards the study of different approaches able to solve the physical inability of Si to act as an efficient light emitter [13, 14]. In particular, since the discovery of intense visible light emission in porous Si by Canham at the beginning of the 1990's [15], a lot of work has been done in studying Si nanostructures which

comprehend porous Si [15 - 17], Si nanocrystals produced with several different techniques namely, high-dose Si implantation in SiO_2 [18 - 20], laser ablation [21, 22], gas evaporation [23], sputter deposition [24, 25], also in form of Si/insulator multilayers [26, 27]. Recently, the formation of Si-QQDs by high-temperature annealing of sub-stoichiometric SiO_x or SiN_x thin films has been reported [26, 28]. This work demonstrated that the luminescence signal from the QDs increases when increasing the annealing temperature and that the light is emitted from the Si-QDs embedded in the amorphous SiO_2 or Si_3N_4 matrix formed after the high-temperature annealing. Moreover, a dependence of the luminescence properties on the crystal size in qualitative agreement with the carrier quantum confinement theory was found [29].

1.3 Si quantum dots for photovoltaic applications

The most innovative approaches in photovoltaics ("third generation") try to directly address the fundamental loss mechanisms in conventional solar cells in order to find ways of surpassing their inherent limiting efficiencies. The aim is to surpass, through novel solar cell designs, the efficiency performance associated with silicon wafer based "first generation" technologies while maintaining the low fabrication costs normally associated with thin film "second generation" technologies. Several third generation approaches have been proposed for achieving these goals.

Today wafer-based crystalline silicon solar cells dominate the marketplace. However this technology has an inherent high material cost, hence there is a significant advantage in improving the efficiency per cost in such material. "Second-generation" thin-film technologies are regularly presented as a promising option for cost-effective solar cells, with a wide variety of choices in terms of device design and fabrication. Thin-film solar cell technologies have the potential for producing cheaper devices on a large scale. However, there are fundamental limitations associated with defects and impurities in thin films.

Several approaches, with the so-called "third generation photovoltaics", have been proposed to substantially increase the energy conversion efficiency of solar cells, including: band gap engineering of Si based materials for all-Si tandems, hot carrier cells using quantum dots, and up- and down-conversion of incident photons [28 - 31]. Schematically in figure 1.3, the possible module production costs per unit area and the energy conversion efficiency ranges for the three generations is shown [32].

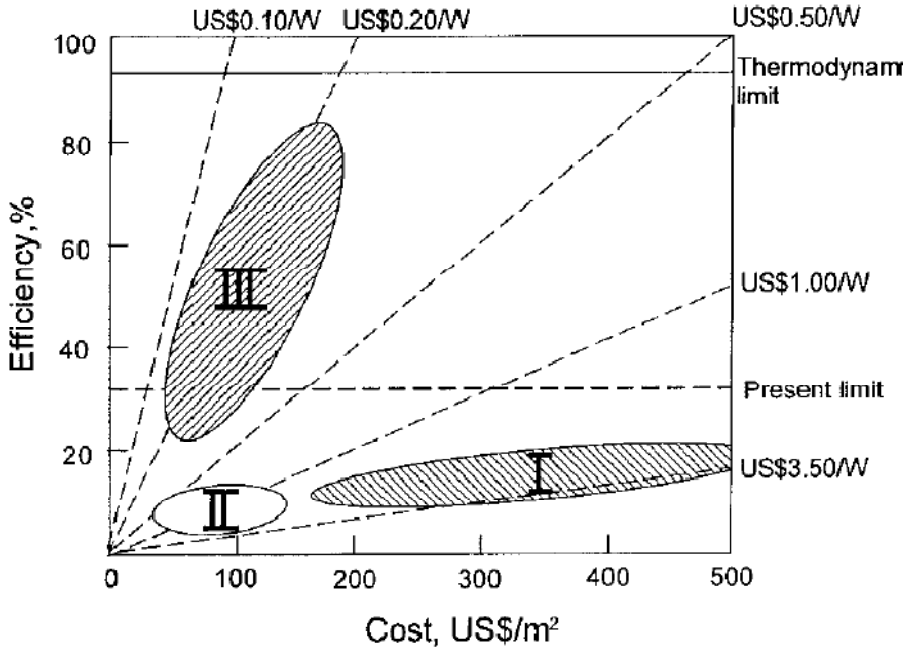

Figure 1. 3 - Efficiency and cost projections for first-, second- and third-generation photovoltaic technology (wafers, thin-films, and advanced thin-films, respectively) [32].

Recent reports have suggested that tandem cells based on silicon nanocrystals embedded in oxides, nitrides or carbides of silicon may be possible [33 - 36]. With such materials, in principle, a bandgap engineering could be achieved so that each cell in the multi-junction stack would be optimized for a different part of the incident spectrum. Investigation of structural, optical and electrical properties of Si-QDs within dielectric matrices is necessary in order to understand material properties for the proposed tandem cell applications. This thesis is intended to contribute to the expanding body of knowledge,

concerning tunability of optical and structural properties of Si-QDs in silicon nitride matrix for third generation photovoltaics devices and more in general for all next-generation optoelectronic applications.

1.3.1 Loss Mechanisms

A conventional photovoltaic cell is basically a shallow *p-n* junction semiconductor diode. The operation of the solar cell can be described by two main processes: photogeneration and charge separation. The solar cell absorbs photons from sunlight and converts them into electron-hole pairs. In this photogeneration process, one decisive parameter is the bandgap energy, E_g, of the semiconductor. Figure 1.4 shows a schematic of an energy-band diagram for a *p-n* junction solar cell under illumination with a voltage (V) applied across the cell and with relevant loss mechanisms indicated. The impact of these loss mechanisms on cell efficiency will now be discussed.

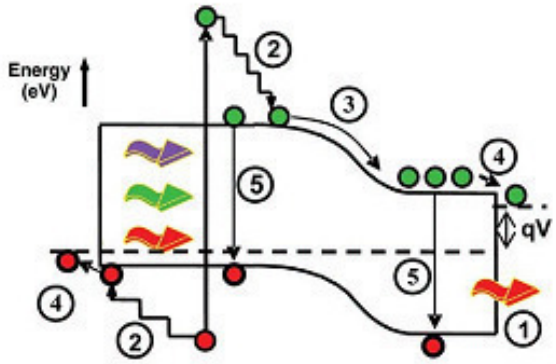

Figure 1. 4 - Loss processes in a standard solar cell: **(1)** non absorption of below-bandgap photons; **(2)** lattice thermalisation loss; **(3)** and **(4)** junction and contact voltage losses; **(5)** recombination loss (radiative recombination is unavoidable).

A crucial property for a solar cell material is its ability to absorb photons. The lower photon energy cut-off for absorption in a semiconductor is determined by its bandgap. The first loss mechanism (1) highlighted in figure 1.4 is

associated with sub-bandgap energy photons which have insufficient energy to be absorbed by the cell and thus do not contribute to carrier generation.

In a semiconductor solar cell, the absorption of a photon with energy greater than or equal to the bandgap of the material causes an electron to be excited from the valence band to the conduction band, leaving behind a hole in the valence band. Any energy greater than the bandgap imparted to the electron and hole by the photon is lost as the pair relaxes back to the band-edges. This loss mechanism (2) is often referred to as a thermalisation loss since the excess energy is transferred to phonons and is essentially wasted as heat. It also represents the dominant loss mechanism, limiting the photovoltaic efficiency to 44% for a material with an optimal bandgap [37]. Thermalisation (2) and sub-bandgap photon (1) losses are the two most important photovoltaic power loss mechanisms. These fundamental losses are associated with the solar cell material and cannot be avoided in traditional cell design. The other loss mechanisms, junction losses (3), contact losses (4) and recombination losses (5), can be minimized through optimization of cell design and processing. An example of a highly optimized device design is UNSW's world record silicon PERL cell at 25% [38], approaching the 29% efficiency limit for a silicon solar cell. In order to surpass photovoltaic conversion efficiency limits, novel approaches which mitigate thermalisation losses and / or sub-bandgap energy photon losses are required. Addressing these challenges is at the heart of third generation photovoltaics.

1.3.2 Proposed approaches for very high efficiency devices

Various third generation approaches have been proposed:

a) hot carrier cells,
b) multiple exciton generation,
c) impurity photovoltaics and multiband cells,
d) photon up and down conversion,

e) thermo-photovoltaic and thermo-photonic conversion,
f) tandem cells.

Each of these approaches will now be briefly discussed. For a more detailed discussion the reader is referred to the works of Green and references therein [32, 39].

a) Hot carrier cells address thermalisation losses. These cells are meant to capture photo-excited carriers before they have a chance to thermalise with the lattice. Carriers must therefore move through the cell quickly or their cooling rates need to be slowed down. Energy selective contacts are also required in order to extract these 'hot' carriers.
b) The concept of generation of multiple electron-hole pairs per photon involves the use of high energy photons and thus addresses thermalisation losses. The idea is to ensure that the excess energy of photo-excited electron-hole pairs is used to create other electron-hole pairs instead of it being lost as heat. One possibility is to make use of impact ionization.
c) Impurity photovoltaics and multiband cells address sub-bandgap energy photon losses. In standard solar cells, photon excitation of carriers involves transitions between the conduction and valence bands. Incorporating impurity levels or bands within the bandgap could in principle be used to capture sub-bandgap photons. A photo-excited electron could use the impurity level as a 'stepping stone' to the conduction band. Of course, the challenge is to ensure that such levels do not act as recombination centres which would hurt photovoltaic performance.
d) Photon conversion employs luminescent materials to alter incident photons so as to enhance absorption in the cell. Down-conversion involves the conversion of one higher energy photon into two lower energy photons. This approach addresses thermalisation losses. Up-conversion involves converting two lower energy photons into one higher energy photon. This solution addresses sub-bandgap photon losses.

e) Thermo-photovoltaic and thermo-photonic conversion concepts use an intermediary solar absorber to reduce the energy of photons impinging on a solar cell, thus avoiding thermalisation losses. In thermo-photovoltaic conversion, reradiated photons from the absorber are collected by the solar cell and any low energy photon can be reflected back to the absorber to be recycled. In thermo-photonic conversion the absorber is replaced with a light emitting diode which will ideally emit photons with energies above its bandgap for supplied electrons with sub-bandgap energies.

f) Tandem cells are composed of multiple solar cells with different bandgaps, where each cell absorbs a separate range of photon energies from the incident solar spectrum. By stacking individual cells on top of one another, with increasing bandgaps from the bottom to the top, each cell acts as a spectral filter for the subsequent cell. This approach minimizes both thermalisation and sub-bandgap photon losses as higher energy photons are absorbed by the higher bandgap cells and the lower energy photons by the lower bandgap cells in the stack. The challenges for implementing tandem cells include: developing suitable bandgap materials in combination with compatible fabrication and processing techniques, matching the current outputs of the individual series-connected cells, and interconnecting the cells via tunnelling junctions. These processing requirements make tandem cells expensive to manufacture. Tandem cells are the only successfully implemented third generation concept devices to date. A recent example is the GaInP/ GaAs/ InGaAs triple tandem cell with efficiency of 35.8% [38].

1.3.3 All-Silicon Tandem Solar Cell

Although tandem cells have been successfully implemented, design constraints require the use of expensive materials and processing steps. A more attractive

alternative would be to find a way to use silicon in a tandem cell design. Silicon has the benefit of being a non-toxic, abundant and widely used material in the photovoltaics industry. Silicon also stands out as a photovoltaic material since its bandgap is very close to the optimal value for a single *p-n* junction solar cell. Furthermore, its bandgap is also close to the optimal value required for the bottom cell in a 2 or 3 cell tandem [37, 40]. One tandem device approach, making use of silicon's qualities, is the all-silicon tandem cell proposed by Green, which incorporates silicon quantum dot material [35]. Figure 1.5 shows a schematic of an all-silicon quantum dot superlattice tandem solar cell with three components making use of superlattices of Si-QDs.

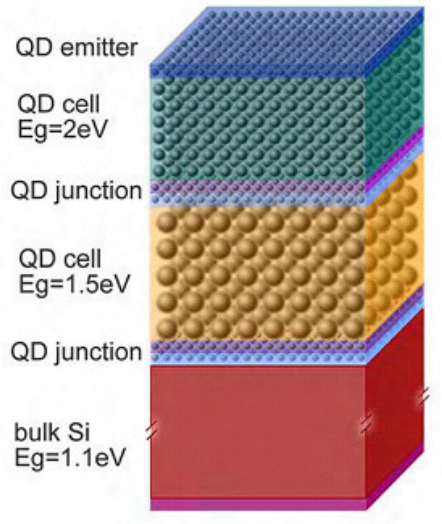

Figure 1. 5 – Schematic of the all-silicon quantum dot superlattice tandem solar cell as proposed by Green (After Green [40]).

Two silicon quantum dot thin film cells with high effective bandgaps are stacked onto a standard single junction silicon solar cell. The effective bandgaps of the two upper cells would be tuned by the size of the quantum dots, via quantum confinement. The upper cells could be composed of silicon quantum dots embedded in a higher bandgap material like silicon oxide, nitride or carbide. A two cell all-silicon tandem would require a top cell with an effective bandgap close to 1.7 eV in order to push the theoretical upper efficiency level to 42.5% [40]. For a three cell all-silicon stack, 1.5 eV and 2.0

eV effective bandgaps would be required for the middle and upper cells, respectively, in order to push the upper efficiency limit to 47.5% [40].

CHAPTER 2

Si-QDs properties and appropriate characterization techniques

One of the important features of semiconductor nanostructures is the flexibility in controlling and designing the properties of such materials [1 - 3], including controlling the size [4, 5], constructing artificial structures [6, 7] and using various doping [8]. Such nanostructures exhibit structural, electronic and optical properties that are unique and different from both macroscopic materials and isolated molecules. In nanostructures, normally 1 to 50 nanometres in scale, the dimensions are commensurate with the De Broglie wavelength of the charge carriers, so that quantum confinement effects become important and the properties of the semiconductors are significantly modified.
In this chapter some properties and appropriate characterization techniques of Si nanoclusters will be introduced.

2.1 Radiative recombination in crystalline silicon

The luminescence from a semiconductor is generally the result of an electron-hole pair radiative recombination. The photon energy is equal to the energy released in the recombination. Since photon momentum is negligible, its emission requires either direct recombination or generation (absorption) of a phonon for momentum conservation. Semiconductors are therefore commonly

divided into two distinct categories depending on the nature of their energy band-gap (fig. 2.1).

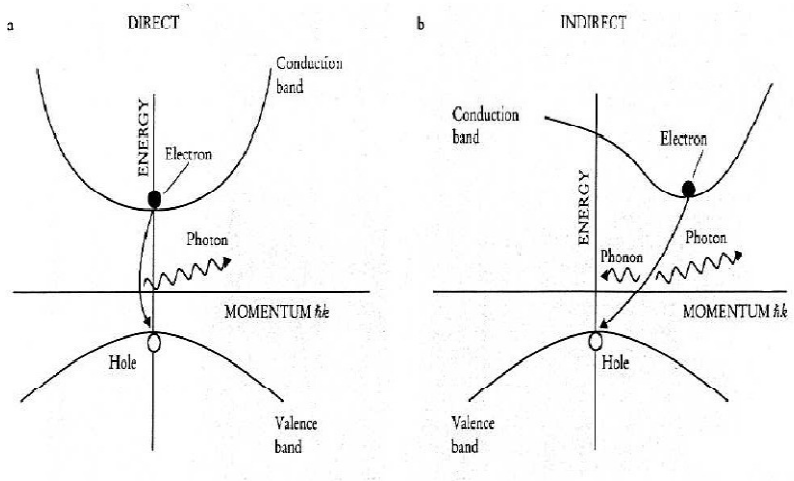

Figure 2. 1 - Schematic of direct and indirect band-gap semiconductors.

In direct band-gap semiconductor the minimum of the conduction band and the maximum of the valence band are coincident in the *k*-space of the crystalline momentum (e.g. GaAs). On the other hand, silicon has an indirect band-gap and the maximum of the valence band and the minimum of the conduction band appear not to coincide; its band structure is shown in fig. 2.2.

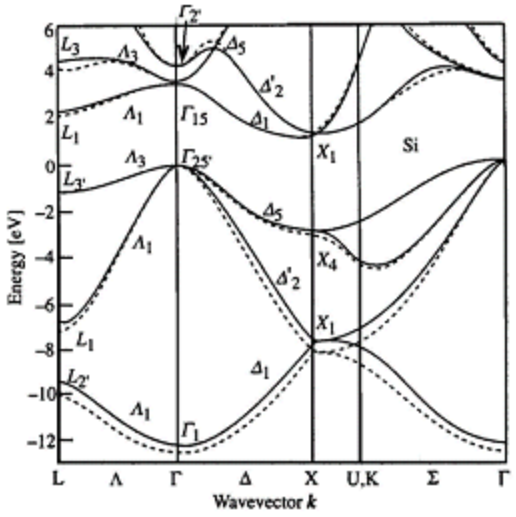

Figure 2. 2 - The band structure of silicon along the X(100) direction and L(111) direction.

Thus, radiative recombination in silicon requires a phonon, which significantly reduces the probability and rate of these processes, resulting in a radiative lifetime of about 10 ms above 20 K [9, 10] to be compared with radiative lifetimes for direct band-gap semiconductors of the order of 100 ns. The τ_{rad} is given by:

$$\tau_{rad} = \frac{1}{B(n_0+\Delta n)} \qquad (2.1)$$

where B is the coefficient for radiative recombination, n_0 the dopant density for *p*-type or *n*-type material and Δn the injected carrier density. At the same time, there are competing non radiative processes, such as Shockley-Hall-Read (SHR) recombination through deep traps due to the presence of defects or impurities in the crystal (see fig. 2.3) [11, 12], characterized by minority carrier lifetime in the low-injection regime given by:

$$\tau_{SHR} = \frac{1}{N_T \nu_{th} \sigma_T} \qquad (2.2)$$

where N_T is the density of traps, ν_{th} is the thermal velocity of the minority carriers and σ_T is the capture cross-section for the minority carriers. The lifetime for the SHR recombination is at room temperature often of the order of 100 μs. This is much shorter than the radiative recombination lifetime for *e-h* pairs in silicon, indicating that non-radiative recombinations are much more probable.

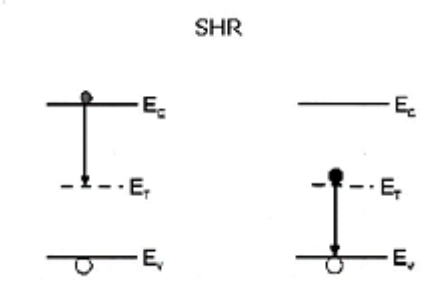

Figure 2. 3 - Recombination / generation processes of *e-h* pairs in crystalline silicon by means of intermediate trap centres.

Furthermore in heavily doped *p*-type and *n*-type silicon *e-h* pairs can recombine through Auger processes (see fig. 2.4) where the energy of the *e-h* pair is given to a third particle such as an electron (*eeh* Auger recombination for *n*-type Si) or a hole (*ehh* Auger recombination for *p*-type Si). Non-radiative Auger recombination provides the fastest deexcitation path [13].
The lifetime τ_{Auger} for an Auger process is determined by:

$$\tau_{Auger} = \frac{1}{C_p p_0^2} \qquad (2.3) \qquad \text{or} \qquad \tau_{Auger} = \frac{1}{C_p n_0^2} \qquad (2.4)$$

where C_p and C_n are the Auger coefficients for the *ehh* (recombination of a *e-h* pair and excitation of a hole) and *eeh* (*e-h* recombination and excitation of an electron) and p_0 and n_0 are the dopant concentrations. Typical values for the lifetime for the Auger recombination are $\tau_{Auger} \approx 10$ µs for a dopant concentration of 10^{18} cm^{-3}.

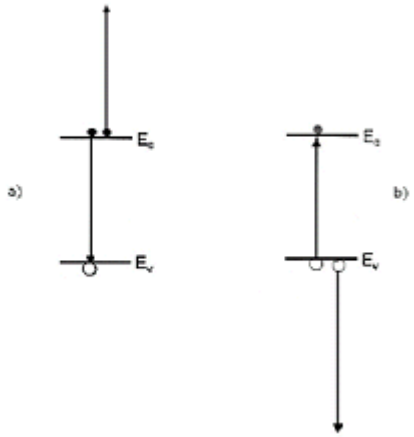

Figure 2. 4 - Auger recombination process involving free carriers (*eeh* or *ehh*).

Since all the above described recombination processes act in parallel, the total lifetime is given by

$$\frac{1}{\tau} = \frac{1}{\tau_{rad}} + \frac{1}{\tau_{SRH}} + \frac{1}{\tau_{Auger}} \qquad (2.5)$$

and the quantum efficiency is:

$$\eta = \frac{\tau_{nonrad}}{\tau_{nonrad}+\tau_{rad}} \qquad (2.6)$$

where τ_{nonrad} is the lifetime for the non radiative processes.
The efficiency of light emission from crystalline Si is low (10^{-6} - 10^{-7}) at room temperature, since the non-radiative recombination processes are faster. It can be increased either by reducing the radiative lifetime or by increasing the non-radiative lifetime (i.e. suppressing non-radiative processes).

2.2 Silicon nanocrystals

The above considerations demonstrate that crystalline silicon is unsuitable as light emitting source, because of the many non radiative phenomena that dominate above the radiative recombination of *e-h* pairs. In order to increase the quantum efficiency, one could act by limiting the movement of an exciton by confining it in a limited space, so reducing the probability to encounter a defect, and consequently, the incidence of the non-radiative phenomena. If we confine the excitons in a very small region, having dimensions of the orders of a few nanometres, we may also increase the radiative recombination rate and, consequently, the quantum efficiency. In fact, for this range of the size, the properties of matter completely change. Since the order of magnitude of the electron and hole De Broglie's wavelength (~ 1 nm) is comparable with the confinement dimension, they behave as particles in a box and the problem can be solved by quantum mechanics. As a consequence, the confinement effect in a region of nanometric size is referred to as quantum confinement effect, and the physical structure in which the quantum confinement of excitons occurs is termed as a nanostructured material. In order to circumvent the inability of crystalline silicon for optoelectronic applications we can follow the route of the quantum confinement of excitons in Si-nanostructures. Quantum confinement

of excitons may occur in only one dimension, in two dimensions or in all the three dimensions, depending on the shape of nanostructures.

At each confinement direction corresponds a radical change in the wave function of the particle and, as a consequence, a series of discrete levels appears. By considering that in bulk crystal a carrier is free to move in every direction, in a *2-D* structure there are only two directions for the movement, while the third direction determines the quantum confinement direction. In a *1-D* structure the free movement is possible in only one of the three directions, while in the two remaining directions quantum confinement occurs. In a *0-D* structure there is a total confinement in each direction and the considered particle cannot move freely anymore. *2-D* nanostructures, also termed as quantum wells, can be obtained by depositing layers of different materials having nanometric dimensions (see fig. 2.5); for example, in Si/Si_3N_4 multilayers Si_3N_4 layers act as a barrier, while excitons are confined in the Si layers. *1-D* structures are also refereed as quantum wires and can be obtained by lithographic processes (see fig. 2.5). *0-D* structures are named quantum dots and can be obtained by means of different techniques such as chemical vapour deposition, ion implantation, sputter deposition etc. Si nanocrystals embedded in Si_3N_4 are an example of *0-D* nanostructures (see fig. 2.5).

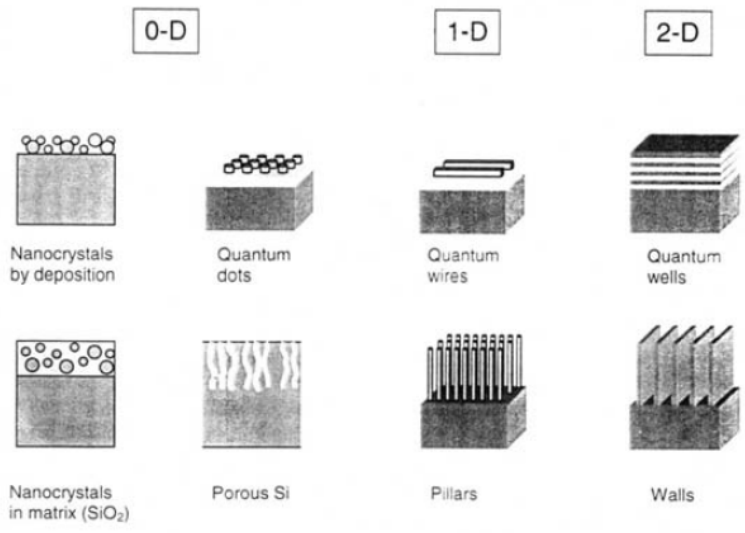

Figure 2. 5 - Classification of low-dimensional structures.

As a results of quantum confinement in the different directions there is a change in the wave function describing the behaviour of electrons and holes, and consequently also the number of states per unit energy, i.e. the density of state (*DOS*), changes as a function of the energy *E* of the particle, as illustrated in fig. 2.6. In the case of a bulk material, the density of states increases with the energy of the particle following a parabolic law, being the *DOS* proportional to $E^{1/2}$. Quantum confinement in one direction determines a step-like increase of the *DOS* function with the energy. Totally different is the *DOS* function in the case of a *1-D* nanostructure, where the number of state decreases following the $E^{-1/2}$ law as the energy increases. Finally, in the case of a *0-D* structure the function, in the ideal case, is formed by deltas marking the presence of discrete levels.

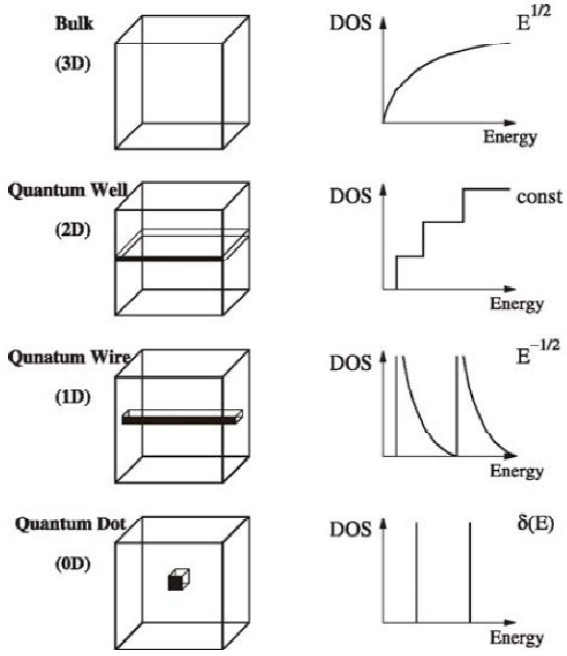

Figure 2. 6 - Schematic of the low-dimensional structure and the density of states (*DOS*) as a function of the energy for a particle constrained to move in the bulk, in a Q-well, in Q-wire and in a Q-dot.

The first experimental evidence that Si nanostructures can really constitute a fundamental step towards the development of a Si based optoelectronics was the observation by Canham and co-workers of a strong room temperature

luminescence from porous silicon. Porous silicon is made by silicon crystallites having nanometric dimensions, where non-radiative processes are almost ineffective since the *e-h* pairs move in a limited space. As a result, a quantum efficiency of more than 10% at room temperature and 50% at low temperatures [14] can be reached.

Porous silicon gives a photoluminescence emission in the visible or near infrared region, with a photoluminescence peak shifting in the blue region as the porosity is increased. The use of porous silicon has several drawbacks, determined by its brittleness and by the instability connected to the aging process. In fact, an oxidation process due to air exposure reduces the Si nanocrystals dimensions and blue shifts the PL peak, reducing also drastically the PL intensity. As a consequence the research has moved towards more stable Si nanostructures and in particular to Si nanocrystals (nc) embedded in a dielectric matrix, such as silicon oxide, nitride or carbide.

Si-nc are complex systems and several models have been proposed in order to explain their optical properties and the band structure; however a general disagreement remains between experimental findings and theoretical calculations, though all models lead to an increase of the band-gap with decreasing crystallite size due to the quantum confinement, as schematically shown in fig. 2.7. The effect is observable as the nanocrystal size becomes smaller than 10 nm.

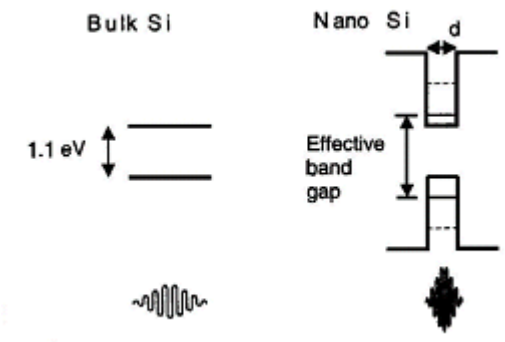

Figure 2. 7 - The increase of the band-gap with decreasing crystallite size due to the quantum confinement.

The simplest model we can consider to explain the quantum confinement effect recurs to the effective mass approximation (EMA). According to this approximation, electrons and holes in a semiconductor are described as independent particles with an effective mass, m_e^* and m_h^* respectively, determined by the convexity of the band edge structure.

By using this model a Si-nc is thought as a spherical potential well that bounds an exciton by means of a high and wide potential barrier determined by the dielectric matrix.

In the EMA approximation, a characteristic length of the system, used to establish the presence of quantum confinement effects, is the Bohr radius of the exciton, defined as:

$$a_b = \frac{4\pi h^2 \varepsilon_r \varepsilon_0}{m^* e^2} \qquad (2.7)$$

where m^* is the reduced mass of the electron-hole pair, e is the electric charge of the electron, ε_r is the relative dielectric constant of Si, ε_o the dielectric constant of vacuum and h is the Planck's constant. Quantum confinement effects occur if the dimension of the nanoparticle is comparable or smaller than the Bohr radius of the exciton, that is equal to 4.3 nm for bulk silicon. We can distinguish a weak confinement for Si-nc whose size is larger than a_b and a strong confinement occurring in Si-nc having dimensions smaller than a_b. The effective mass approximation can be illustrated through the simple case of confinement in a nanoparticle with linear dimension L_x, L_y, L_z, where the band-gap is given by the expression:

$$E_{np} = E_{Si-bulk} + \frac{\hbar^2 \pi^2}{2}\left(\frac{1}{m_e^*} + \frac{1}{m_h^*}\right)\left(\frac{1}{L_x^2} + \frac{1}{L_y^2} + \frac{1}{L_z^2}\right) \qquad (2.8)$$

where $E_{Si\text{-}bulk}$ = 1.1eV, while m_e^* e m_h^* are respectively the effective mass of electron and hole. By this expression it is evident that the energy necessary to generate an electron-hole pair increases by decreasing the size of the system [15 - 17].

2.3 Array of Si-QDs in a dielectric matrix

In order to engineer the band-gap of a material, an array of quantum dots would be required. Ideally, in an ensemble of quantum dots, quantization effects would be preserved if individual dots are isolated from each other. However, carrier transport requires that adjacent dots be in close enough proximity to allow for the overlap of their electron wavefunctions. As a first order approximation, an ensemble of quantum dots could be represented as an array of rectangular potential wells.

The wavefunction of a confined electron in a potential well, at a quantized energy level *E*, will penetrate into the barrier with an exponential decay. The coefficient for such a decay into a rectangular barrier of width *L* is described by the attenuation constant,

$$\alpha = \frac{\sqrt{2m^*(V_0 - E)}}{\hbar} \qquad (2.9)$$

where V_0 is the potential of the barrier. In this case the transmission coefficient, *T*, or penetrability of the wavefunction into the barrier, is

$$T \approx e^{-2\alpha L} = \exp\left\{-\frac{2}{\hbar}[2m^*(V_0 - E)]^{1/2}L\right\} \qquad (2.10)$$

With appreciable overlap of electron wavefunctions of adjacent potential wells, energy minibands may form, thus creating a superlattice.

In terms of silicon quantum dots, such an arrangement may be achieved by embedding silicon nanocrystals within a higher band-gap material. From an engineering point of view, obvious choices include silicon's own oxide, nitride and carbide. The schematic in figure 2.8 represents the bulk band alignments for silicon with SiC, Si_3N_4, and SiO_2.

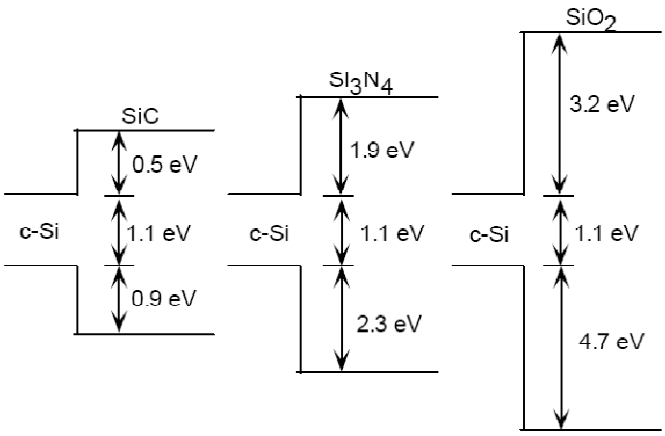

Figure 2.8 – Schematic of conduction and valence band offsets between crystalline silicon and SiC, Si_3N_4, and SiO_2. Adapted from Green et al. [18].

While a higher potential barrier results in enhanced confinement, it also reduces the penetration of the electron wavefunction into the barrier, thus lowering the transmission or tunnelling probability. In a superlattice structure, higher potential barriers would reduce the overlap of wavefunctions from adjacent potential wells and inhibit the formation of minibands. The choice of barrier material therefore results in a compromise between degree of confinement and ability for carrier transport.

Silicon nanocrystals embedded in a silicon dioxide matrix have received a great deal of attention, however concerns over their limited PL energy range [19, 20] and the difficulties of carrier transport due to the high band-gap of SiO_2, have prompted investigations of silicon nitride as more suitable matrix material, that is the topic of this thesis.

2.4 Silicon Nanoparticles in Silicon Nitride

Silicon nanocrystals embedded in a silicon dioxide matrix have received a great deal of attention, however concerns over their limited PL energy range [19, 20] and the difficulties of carrier transport due to the high band-gap of SiO_2, have prompted investigations of silicon nitride as a more suitable matrix

material. This section will provide a review of reported works on silicon nanocrystals in nitride, with an emphasis on observed PL behaviour suggesting quantum confinement effects.

2.4.1 Amorphous Silicon Nanoparticles in Nitride

Some research efforts have been made looking at the formation of amorphous silicon nanoparticles embedded in silicon nitride. Photoluminescence emission suggesting confinement effects has been reported. These results are briefly reviewed here and will provide a wider context for discussion of existing ambiguities with PL from silicon nanocrystals.

Park et al. reported the formation of amorphous silicon nanocrystals in nitride films grown by PECVD using nitrogen-diluted 5% silane and additional nitrogen as reactant gases [21, 22]. Films were deposited at 300°C with no additional thermal treatment required to induce nanoparticle formation. The N_2 flow rate was varied from 100 to 800 sccm and was used to control the growth rate of the film and the amorphous nanoparticle sizes. The average nanoparticle sizes, as determined from transmission electron microscopy, were reported as varying from 2.4 down to 1.3 nm for increasing N_2 flow rates. A PL blue shift was observed with decreasing nanoparticle size and this behaviour was attributed to quantum confinement.

The PL peak positions were fitted to a simplified effective mass model, $E = E_{bulk} + C/d^2$, where E_{bulk} is the band gap for the bulk material, d is the nanoparticle diameter and C is a "confinement" fitting term. A good fit to the data was achieved with the following expression: $E = 1.56 + 2.40/d^2$. The fitted bulk band gap is very close to that of amorphous silicon although the significance of the C value was not addressed.

Wang et al. reported the formation of amorphous silicon nanoparticles in thick (1.2 μm) silicon nitride films grown on cold substrates by plasma enhanced chemical vapour deposition with a SiH_4, N_2 and H_2 gas mixture, followed by a

low temperature anneal [23]. Control over nanoparticle size and PL emission was reported for N_2/SiH_4 flow ratios varied from 1.0 to 5.5. A PL emission blueshift was observed for films grown with these increasing N_2/SiH_4 ratios followed by a 500°C annealing for 2 minutes in an N_2/Ar ambient. The PL emission peaks ranged from ~ 650 nm to ~ 450 nm. A corresponding change in nanoparticle sizes, as determined from transmission electron microscopy, from 4.5 to 1.5 nm was also reported with increasing N_2/SiH_4 flow ratios.

While these results suggest confinement effects, a PL blueshift was also observed for lower annealing temperatures with no change in nanoparticle sizes. This blue shift was attributed to a reordering of bonds at the interface with an increase in Si-H bonding.

Wang et al. attributed the PL behaviour of these films to a combination of the surface chemistry of the nanoparticles and quantum confinement.

2.4.2 Si Nanocrystals in Nitride

Various techniques have been used for the growth of silicon nanocrystals in silicon nitride. The different processing conditions and parameters employed make comparison of results rather difficult.

Molinari et al. reported the formation of silicon nanocrystals in thick nitride films (200 nm) deposited by ion beam assisted evaporation followed by a high vacuum anneal for temperatures ≥ 950°C [24, 25]. Nanocrystal formation was verified using Raman spectroscopy, TEM, and X-ray diffraction. It is clear from TEM analysis that the solid phase crystallization in these thick films results in a wide distribution of nanocrystal sizes.

Silicon nanocrystal formation has also been reported by Yang et al. for nitride films grown by N_2^+ ion beam sputtering of silicon wafers followed by a furnace anneal in a N_2 ambient at 950°C [26]. Nanocrystal formation was verified via limited TEM data and PL results were reported as a function of the excess silicon in the film, not nanocrystal sizes.

Cho et al. reported the formation of silicon nanocrystals in nitride via high temperature annealing (110°C) of silicon nitride multilayer structures deposited both by reactive magnetron co-sputtering and radio frequency plasma enhanced chemical vapour deposition [27]. TEM results suggest control over nanocrystal size is achieved via the multilayer structure.

Silicon nanocrystals embedded in nitride have also been grown onto cold substrates by e-beam evaporation of silicon into an inductively coupled plasma using an N_2/H_2 gas mixture [28]. Clear evidence of nanocrystal formation by this technique was provided by TEM imaging and electron diffraction. Room temperature PL was observed, but no nanocrystal size dependence behaviour was reported.

Dal Negro et al. reported the formation of silicon nanocrystals from silicon-rich silicon nitride films grown by PECVD with a SiH_4/N_2 gas mixture and subsequently annealed at 700°C [29]. Nanocrystal formation was verified via Raman spectroscopy and TEM imaging.

Kim et al. reported in-situ growth of silicon nanocrystals embedded in silicon nitride prepared by plasma enhanced chemical vapour deposition (fig. 2.9). The size of the nanocrystals were reportedly controlled by the SiH_4 to N_2 gas flow ratios [30].

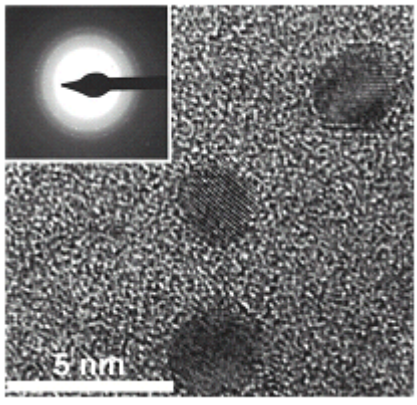

Figure 2. 9 - HRTEM image of crystalline Si-QDs. The inset shows the ring patterns for the electron diffraction from the crystalline Si-QDs [31].

The observed PL peak positions were fitted to a simplified effective mass model, $E = E_{bulk} + C/d^2$, as reported in the previous section. A good fit to the data was achieved with the following expression: $E = 1.16 + 11.8/d^2$. The fitted bulk band gap is very close to that of crystalline silicon although the significance of the *C* value was not addressed.

In-situ formation of silicon nanocrystals was also achieved with PECVD deposition using a SiH_4 and NH_3 gas mixture [31]. A PL shift from 1.73 to 2.77 eV was reported by adjusting the NH_3 flow rate and the chamber pressure. In other words, an increase in NH_3/SiH_4 ratio resulted in a blue shift of the PL energy. A fit to the PL data using the same EMA expression as above gave $E = 1.13 + 13.9/d^2$, quite similar to the results of the previous study (fig. 2.10).

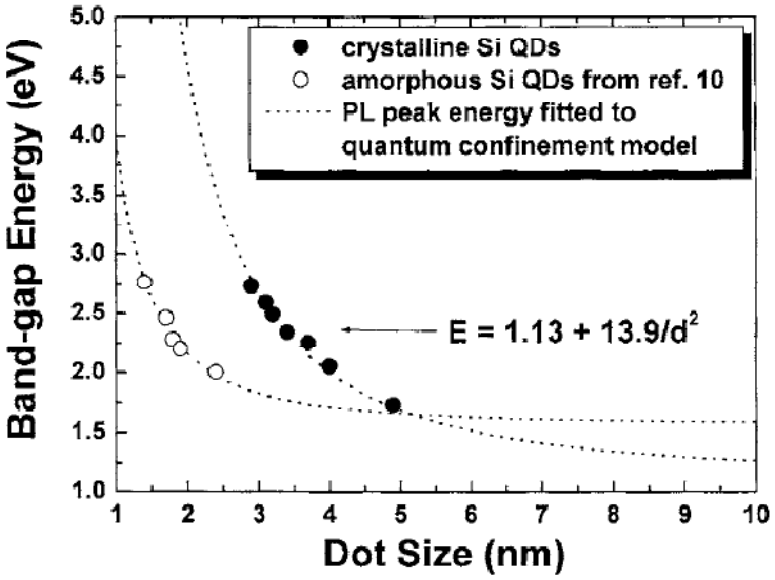

Figure 2. 10 - PL peak Energy for crystalline Si-QDs as a function of dot size *d*. Dotted lines are fitted curves for *a*Si-QDs and *c*Si-QDs. The filled and open circles are data points for crystalline and amorphous Si-QDs, respectively [31].

Approaches requiring annealing steps have shown similar PL results.

While the formation of silicon nanocrystals has been achieved by various techniques, clear experimental evidence of quantum confinement effects remains an issue.

2.5 Characterization techniques

In order to experimentally verify quantum confinement effects in nanostructures a clear correlation between structural and optical properties must be unambiguously demonstrated. One challenge lies in the fact that no single characterization technique can provide a clear and definitive structural picture of silicon nanocrystals embedded in an amorphous matrix, except for the destructive and time-consuming transmission electron microscopy (TEM) analysis. Moreover, the presence of nanoparticles is not enough to conclude that some observed properties are governed by quantum confinement. As a result, complimentary techniques must be applied in parallel.

In this thesis, the optical characterization is primarily performed by measuring photoluminescence and absorption spectra. Fourier transform infrared (FTIR) spectroscopy is also employed to monitor molecular changes in the nitride films when changing the material stoichiometry and after the thermal treatments required for nanocrystal formation. Energy-filtered transmission electron microscopy (EFTEM) and Raman spectroscopy are used as structural / morphological characterization tools. These two techniques allow for the verification of formation Si nanoparticles (both amorphous and crystalline).

2.5.1 Photoluminescence

Photoluminescence (PL) is a widely used technique for investigating quantum confinement. Spectroscopic PL involves the excitation of a sample with a monochromatic source in order to excite electrons into higher energy states than they would otherwise occupy under equilibrium conditions. When this electron makes a transition back down to a lower energy state, the energy difference can be emitted as a photon. In principle PL can therefore be used to determine the band-gap of a material provided the excitation source is of high enough energy to excite electrons from the valence band to the conduction

band. However, the presence of any defect states can alter the radiative transitions and convolute or dominate the measured spectrum. This limitation must be considered when interpreting PL data.

In our studies, room temperature photoluminescence has been excited at different excitation energies: at high energy (compared to the absorption edge), with the 325 nm line of a He - Cd laser source, and at low energy, with the 514 nm line of Ar^+. PL emission has been also studied at different temperatures, from room temperature down to 12K, with the 458 nm line of an Ar^+ laser. Different setups have been used in the three cases. With excitation at 325 nm the PL response is collected by an optic guide and registered in the visible range by a calibrated CCD spectrometer (OCEAN-OPTICS S2000). The measurement at 514 nm is performed with a Renishaw inVia Raman microscope.

With excitation at 458 nm, light emission is detected with a Jobin-Yvon iHR320 spectrometer coupled to a liquid nitrogen-cooled CCD Hamamatsu camera (fig. 2.11). This characterization has been performed at the Lyon Institute of Nanotechnology (INL) in France.

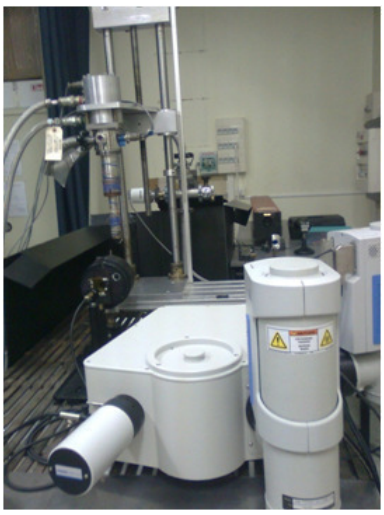

Figure 2. 11 – Experimental PL setup at 458 nm.

In all cases the spectra were corrected for the spectral response of the system. This characterization has been performed on samples deposited on c-Si substrates.

2.5.2 Absorption spectra

A spectrophotometer is used to measure the reflectance and transmittance (in the same spot) of samples in order to determine their absorption properties in the spectral range 200 – 1500 nm using thin films deposited on quartz substrate that is transparent in this wavelength range (quartz absorption spectra is shown in fig. 2.12).

The absorption spectrum of a semiconductor is directly related to its band structure. Fundamental absorption involves the transition of an electron from the valence band to the conduction band. Experimentally, fundamental absorption results in a steep edge in the absorption spectrum and is directly related to the energy gap of the semiconductor [32].

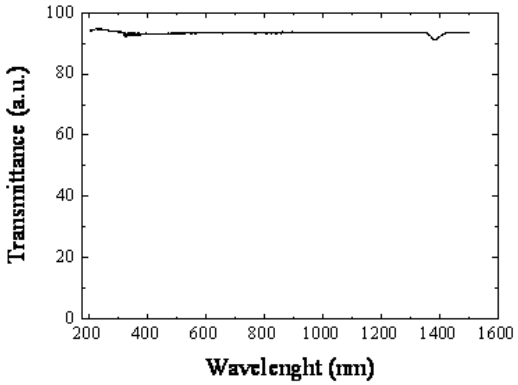

Figure 2. 12 – Transmittance spectrum of quartz.

Absorption is described by a coefficient, $\alpha(\hbar\omega)$, which describes the decay of light intensity, *I*, as it propagates a distance, *x*, through a material as described in the following expression:

$$\frac{dI}{dx} = -\alpha I \qquad (2.11)$$

For a slab of material with a thickness, *d*, the absorbed intensity, or Absorptivity, when ignoring interference in the slab is given by [33]

$$A = (1 - R)[1 - \exp(-\alpha d)] \qquad (2.12)$$

Following the conservation of energy,

$$R + T + (1 - R)[1 - \exp(-\alpha d)] = 1 \qquad (2.13)$$

Therefore the absorption coefficient, can be written as:

$$\alpha = \frac{1}{d}\ln\left(\frac{1-R}{T}\right) \qquad (2.14)$$

One of the simplest ways for taking into account the quartz substrate is through the rather expression [34]:

$$\alpha(\lambda) = \frac{1}{d}\ln\left[\frac{T_Q(1-R(\lambda))}{T(\lambda)}\right] \qquad (2.15)$$

where T_Q is the quartz transmittance (fig. 2.12). In this case, multiple reflections are neglected (but they should be fairly irrelevant because of the quite low reflectance values).

In any case, the overall indetermination on alfa is lower than 5% (including the errors on *d*, *T* and *R*).

Experimentally, the alfa values were obtained by extracting both the normal transmittance and the 8° reflectance spectra in the 200 – 1500 nm wavelength range by using a Perkin Elmer λ-900 UV/visible/Near-Infrared spectrophotometer equipped with an integrating sphere. Particular care was

used to extract transmittance and reflectance spectra from the same area of the sample and also to avoid misalignment during the acquisition.

In figure 2.13, literature data for the absorption coefficient of a-$Si_{1-x}N_x$ films with different atomic composition is reported [35]. Here the data extends deep in the below-gap region where other techniques are required to estimate alfa. The continuous lines and the symbols represent the data from spectrophotometry (*T* - *R* data) and from photothermal deflection spectrometry (PDS data), respectively.

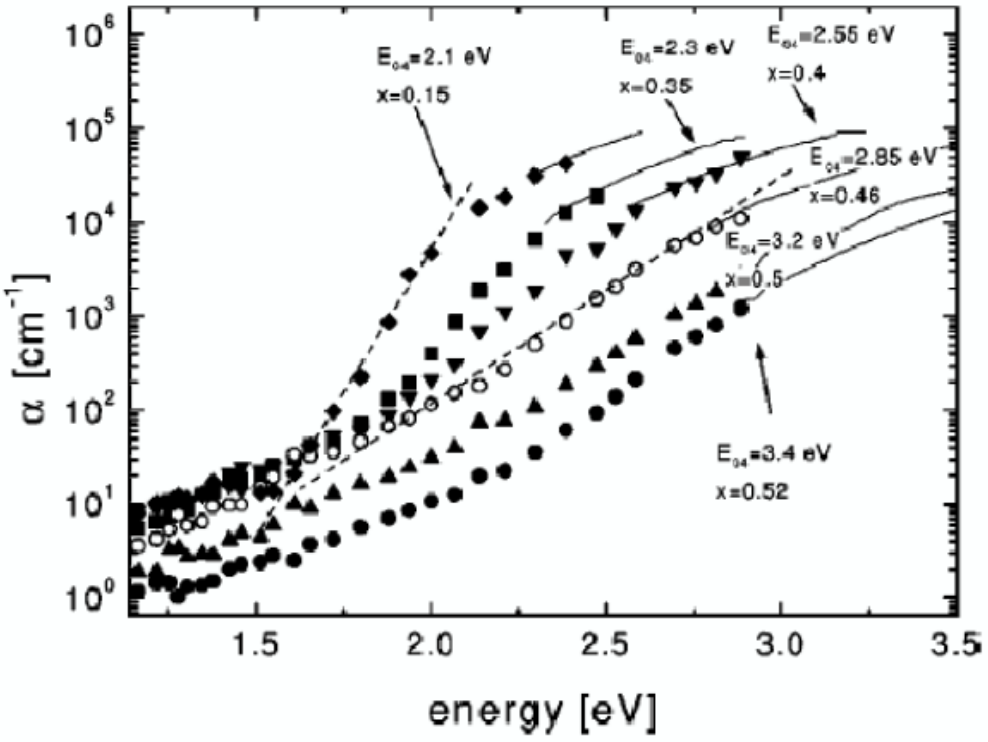

Figure 2. 13 – Absorption coefficient distribution for a-Si_{1-x} N_x films with different atomic composition. The continuous lines and the symbols represent the *T* - *R* and PDS data, respectively. The composition and the optical gap E_{04} (energy for which the absorption coefficient is 10^4 cm^{-1}) are indicated for each curve (from ref. [35]).

It is straightforward to observe that N incorporation causes a monotonical enhancement of the optical gap. Moreover, for Si-rich materials we can distinguish three typical regions:

1) the fundamental absorption region (high energy), involving extended states in conduction and valence bands;
2) the exponential tail region (intermediate energy), mainly due to static disorder , characterized by the Urbach energy (E_U), namely the logarithmic slope of the absorption distribution;
3) the excess absorption region (low energy) essentially due to defects.

2.5.3 FTIR spectroscopy

Fourier transform infrared spectroscopy (FTIR), is a non-destructive technique for determining the nature of chemical bonds present within a material and quantifying them. Its principle is based on the interaction between infrared radiation and matter [36, 37].

When an ensemble of atoms comes together to form a molecule various mechanical vibrational modes become possible [38]. These molecular vibrations tend to occur in the infra-red energy range. The frequencies of these vibrations can be used to identify distinct bonding configurations.

By submitting a sample to scan the infrared spectrum, the intensity absorbed by it will vary depending on the nature of its chemical bonds. The obtained spectra represent at each wavelength the ratio of transmitted intensities, with or without sample. It is then possible to determine the absorbance A and the absorption [36, 37]. The transmitted intensity through the sample is defined as:

$$I = I_0 e^{-\alpha d} \qquad (2.16)$$

where I is the transmitted intensity, I_0 is the incident intensity, α is the absorption coefficient of sample and d is the thickness of the sample.

Because of perturbation caused by dipole / dipole interactions, the spectra show broadened peaks (absorption bands). The wavelength, the shape and intensity of observed absorption bands in the FTIR spectra are characteristic of the

molecular structure of the sample. This technique can also be quantitative in determining the peak area of absorption. The intensity of the absorption at a characteristic wavelength is related to the concentration of chemical bonds.

The basic optical component of Fourier transform spectrometers is a Michelson interferometer.

At the output of the interferometer, the modulated beam is reflected towards the sample, where each wavelength is absorbed more or less. The detector converts this new interference signal into an electrical one. Comparing the final and the initial (preliminary measurement without sample) spectrum, it is possible to determine directly the spectral absorption of the sample.

All FTIR spectra presented in this thesis were obtained using a Perkin Elmer Spectrum Gx spectrometer (the setup is shown in fig. 2.14). Measurements are performed in transmission mode and all the FTIR spectra in this thesis are presented as Absorbance spectra, that is defined as;

$$A = -\log\left[\frac{I_{Sample}}{I_{Reference}}\right] \qquad (2.17)$$

where I_{Sample} and $I_{Reference}$ are the transmitted intensities for the sample and the reference. In this thesis the sample is the silicon nitride film on a silicon wafer, while the reference is a silicon wafer.

The transmittance of the silicon wafer is therefore subtracted from that of the film-on-wafer sample in order to extract the film's spectra. As will be shown in Chapter 3 and 4, FTIR is ideally suited to monitor molecular bonding changes in silicon nitride films due to annealing treatments.

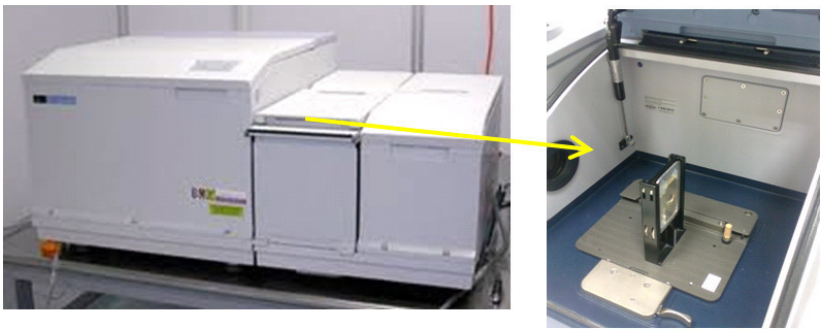

Figure 2. 14 – FTIR experimental setup. **Zoom:** Acquisition mode of measurement (Transmission mode).

Amorphous silicon nitride films have signature vibrational modes which are infra-red active (the modes are listed in Table 2.1).

Table 2. 1 – Typical infra-red vibrational modes for amorphous silicon nitride.

Peak	**Peak position (cm-1)**	**Reference**
Si-N symmetric stretch	490	[39, 40]
Si-H wag-rocking	650	[40]
Si-N asymmetric stretch	830	[39, 40]
Si-O stretching	1080	[39]
N-H bending	1180	[39, 40]
Si-H stretching	2300	[39 - 41]
N-H stretching	3340	[39, 40]

2.5.4 Raman spectroscopy

Raman spectroscopy is a powerful analytical technique based on the analysis of the inelastic scattering of light interacting with the material under test [42]. This method can be applied either to gas, liquid or solid state materials. Raman spectroscopy provides spectra characteristic of molecular vibrations (or of phonons in solids) that can be used for sample identification and / or phase quantification. A Raman spectrum represents the intensity of the scattered light

as a function of the shift in frequency (i.e. energy) from the excitation light frequency. This "Raman shift" is directly linked to the vibrational energy of the bonds between the atoms within the probed material. More specifically, in the case of silicon thin films, Raman spectroscopy is particularly well suited to discriminate between the amorphous phase and the crystalline phase. Therefore, this analysis technique allows one to quantify the degree of crystallinity of samples.

The main advantage of Raman spectroscopy is to be a fast and non-destructive tool. Indeed, no sample preparation is required and this non-contact experimental technique enables characterization of samples while avoiding sample contamination or deterioration.

2.5.4.1 The Raman scattering process

In quantum mechanics the scattering is described as an excitation to a virtual state lower in energy than a real electronic transition with nearly coincident de-excitation and a change in vibrational energy. The scattering event occurs in 10^{-14} seconds or less. The virtual state description of scattering is shown in Figure 2.15.

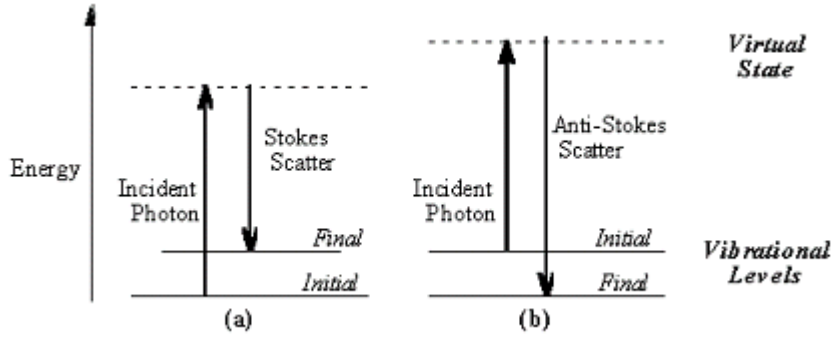

Figure 2. 15 – Energy level diagram for Raman scattering; **(a)** Stokes Raman scattering **(b)** anti-Stokes Raman scattering.

The energy difference between the incident and scattered photons is represented by the arrows of different lengths in figure 2.15. Numerically, the

energy difference between the initial and final vibrational levels, $\bar{\nu}$,or Raman shift in wavenumbers (cm^{-1}), is calculated through equation:

$$\bar{\nu} = \frac{1}{\lambda_{incident}} - \frac{1}{\lambda_{scattered}} \qquad (2.18)$$

in which, $\lambda_{incident}$ and $\lambda_{scattered}$ are the wavelengths (in cm) of the incident and Raman scattered photons, respectively. The vibrational energy is ultimately dissipated as heat. Because of the low intensity of Raman scattering, the heat dissipation does not cause a measurable temperature rise in a material.

At room temperature the thermal population of vibrational excited states is low, although not zero. Therefore, the initial state is the ground state, and the scattered photon will have lower energy (longer wavelength) than the exciting photon. This Stokes shifted scatter is what is usually observed in Raman spectroscopy. Figure 2.15 (a) depicts Raman Stokes scattering. A small fraction of the molecules are in vibrationally excited states. Raman scattering from vibrationally excited molecules leaves the molecule in the ground state. The scattered photon appears at higher energy, as shown in figure 2.15 (b). This anti-Stokes-shifted Raman spectrum is always weaker than the Stokes-shifted spectrum, but at room temperature it is strong enough to be useful for vibrational frequencies less than about 1500 cm^{-1}. The Stokes and anti-Stokes spectra contain the same frequency information.

A schematic Raman spectrum may appear as figure 2.16. In the example spectrum, notice that the Stokes and anti-Stokes lines are equally displaced from the Rayleigh line, and that the anti-Stokes line is much less intense than the Stokes line.

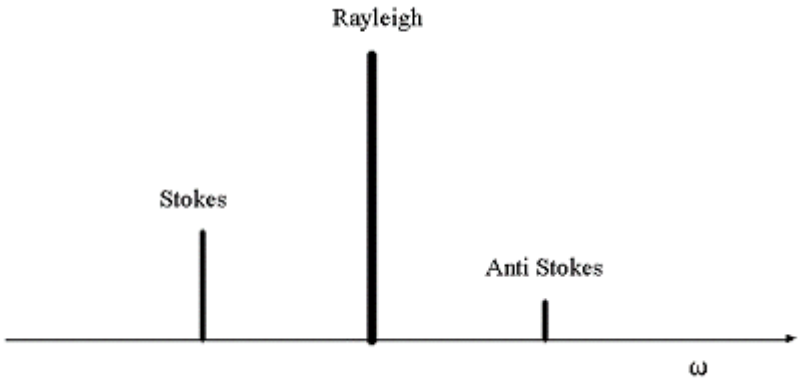

Figure 2. 16 – Schematic of a Raman spectrum.

2.5.4.2 Raman spectroscopy on Si-nanoparticles

Among the various investigation techniques, Raman spectroscopy is a very sensitive tool for probing semiconductor nanostructures and in particular Si-QDs. Here, the vibrational properties of the nanostructures, i.e., the acoustic and optical phonon modes in confined systems, and the interaction with a photon and the modification of selection rules play a fundamental role for the understanding of a basic scattering process with a short wavevector [43 - 45]. From an experimental point of view, with reference to the specific case of Si bulk crystal, the Raman spectrum, exhibits a peak at 520 cm^{-1}, due to the optical phonon dispersion curves, with a line-width, Γ. In nanocrystals, valuable experimental information can be obtained by the Raman spectroscopy, as a function of the size, through the energy shift of the Raman peak and the correspondent line broadening, both size dependent. In order to obtain a good interpretation of these experimental data, several models have been developed, among them the microscopic force model [46], the bond polarization model [47], the spatial correlation model [48]. In some cases, phenomenological approaches, considering optical and / or acoustic phonons, have been attempted [46, 49, 50].

However, none of these models gives a satisfactory description of the phonon confinement within the dot, capable to determine simultaneously the frequency shift and the line-width. Often, poor agreement between experimental data and theoretical calculations has been obtained, although some phenomenological models give the right trend of the Raman shift as a function of the size, using ad hoc confinement phonon functions. These theoretical models will be presented in chapter 4.

In the case of silicon thin films, Raman spectroscopy can be easily utilized for monitoring the crystallinity. Indeed, the different phases (amorphous or crystalline) result in different peaks on a Raman spectrum. The position and the width of the peaks strongly depend on the size and structure of the nanocrystal according to dispersion of localized modes. Its position approximates to 520 cm^{-1} when the size of the crystal cluster grows up [51].

Figure 2.17 shows typical Raman spectra (i.e. Stokes peaks) measured on a crystalline silicon (*c*-Si) wafer and on various silicon thin films. The Raman spectrum of c-Si (Fig. 2.17 (a)) exhibits a narrow peak centred at 520 cm^{-1}. This peak corresponds to the position of the Transverse Optic (TO) mode in crystalline silicon. There is no translation symmetry in amorphous solids, therefore, the law of conservation of momentum vanishes, and Raman spectrum of amorphous silicon is characterized by the density of phonon states, which has a broad maximum near 480 cm-1 (fig. 2.17 (c)). This is characteristic of the TO mode of the amorphous silicon phase. Finally, the Raman spectrum in Fig. 2.17 (b) is something in between the two cases corresponding to a mixed material with amorphous phase and nanocrystalline phase.

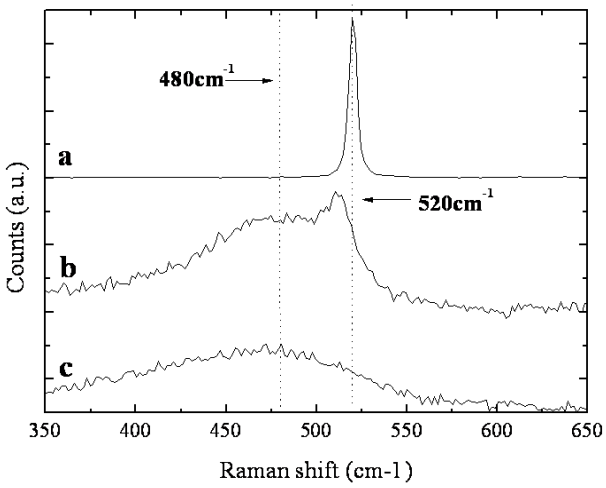

Figure 2.17 – Examples of Raman spectra taken on different samples. **(a)** a *c*-Si wafer, **(b)** a sample with mixed phases, and **(c)** an *a*-Si:H sample.

The Raman measurements in this work have been performed using a Renishaw inVia Reflex Raman microscope functioning in backscattering configuration using usually the 514 nm line of an Ar^+ laser (fig. 2.18).

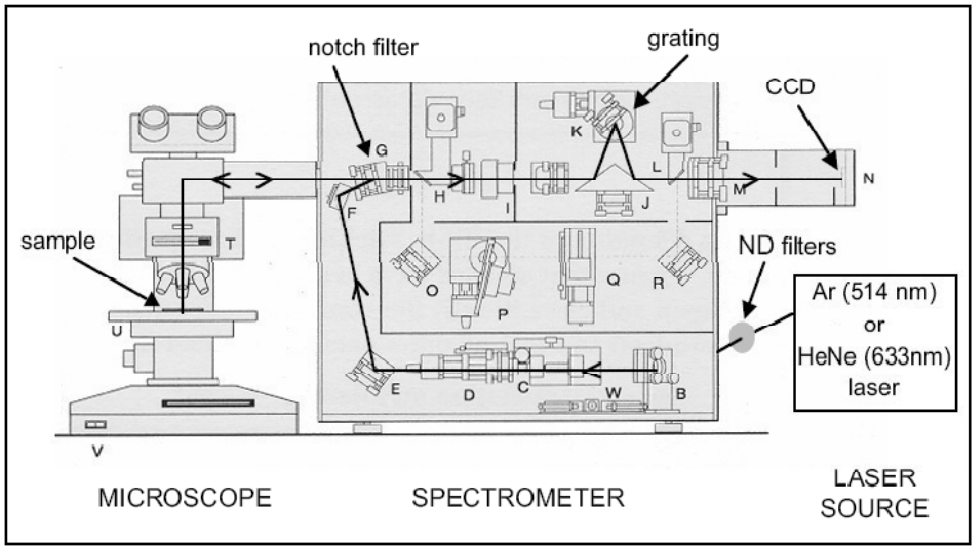

Figure 2. 18 - Illustration (taken from [52]) of the Renishaw Raman imaging microscope, with the spectrometer door removed (to show the main assemblies inside).

In Raman microscopy the sample is illuminated with a laser beam focused through a conventional optical microscope, and the light backscattered by the material is analyzed by the Raman spectrometer coupled to the microscope. The incident power was kept low to avoid crystallization and distortion of the spectra due to laser heating. Our Raman system gives also the possibility to excite using the 633 nm line of He - Ne laser.
This characterization has been performed on films deposited on quartz substrates.

2.5.5 EFTEM

An energy filtered transmission electron microscope (EFTEM) allows to investigate in detail the morphologic properties of Si nanoclusters embedded in a dielectric matrix and to correlate the structural results with the optical properties of the system. This microscope of new generation allows us to obtain information about the nanocluster density, the crystalline and amorphous fraction and the concentration of aggregated Si atoms.
The EFTEM is the most versatile and performing analytic microscope for high-resolution characterization of nano-aggregates, whether in amorphous phase or embedded in an host material. The necessity to use an EFTEM instead of a Conventional Transmission Electron Microscopy (CTEM), is due to the fact that the latter technique generally requires the Si-NDs in the crystalline, rather than in the amorphous phase. In order to understand how to take advantage by these electrons we have to know how beam electrons interact with the sample.
When a very thin sample is illuminated with a beam of high-energy electrons, a majority of the electrons will pass unhindered through the sample but some will interact via electrostatic forces with the constituent atoms, being scattered elastically or inelastically. The former involves Coulomb interaction with an atomic nucleus, the latter, interaction with the atomic electrons of inner or outer-shell surrounding each nucleus.

Elastically scattered electrons can only be lost from the image by large-angle scattering outside the objective aperture. Thus image contrast is popularly understood to arise from creation of an intensity deficit in regions of large scattering or 'mass thickness' where these large-angle scattered rays are intercepted by objective aperture. The theory which describes this process is the theory of incoherent imaging [53]. By comparison, the high-resolution transmission electron microscopy is a close analogue to the optical phase-contrast microscope Electrons scattered inelastically as a result of energy loss and wavelength change in the specimen, are brought to a focus plane far distant from the viewing screen showing the elastic image. This out-of-focus 'inelastic', as far as CTEM, contributes only with a uniform background to the in-focus elastic image [54], instead, for the EFTEM case it will provide a tremendous amount of both structural and chemical information.

The energy-filtering transmission electron microscope is a conventional transmission electron microscope (fig. 2.19 (a)) equipped with an energy filtering apparatus mounted in-column or post-column, fig. 2.19 (b) and (c) respectively.

This filter allows us to select, by an energy-selecting slit, a portion of the energy-loss electrons for imaging. Thus, a chemical mapping of all species present in the sample is easily achieved with the very high spatial resolution, typical of the TEM.

Therefore this analytical technique is particularly suitable to characterize Si-nc embedded in dielectric matrix, since it is sensitive only to the presence of the elements and not to their phase, crystalline or amorphous, and works very well in case of Si nanograins in SiN_x since the Plasmon energy loss in Si (~ 16 eV) is well separated from the Plasmon energy loss in silicon nitride (~ 24 eV). Figure 2.20 reports a comparison between two images of an identical portion of the sample obtained applying the two different techniques: dark field and energy filtered microscopy.

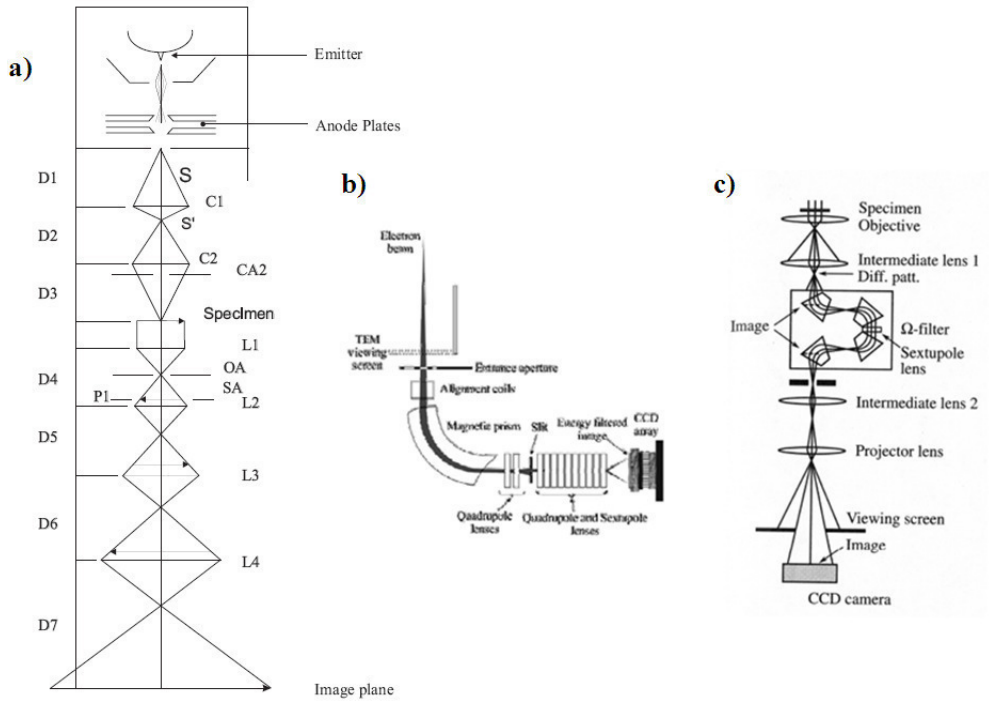

Figure 2. 19 – (a) Ray diagram of an Electron Transmission Microscope operating at high magnification; **(b)** The post-column Gatan Imaging Filter attached to the TEM column after the imaging lenses, beneath the viewing screen. **(c)** Ray paths through the filter system inserted in the imaging lens system of the LEO TEM.

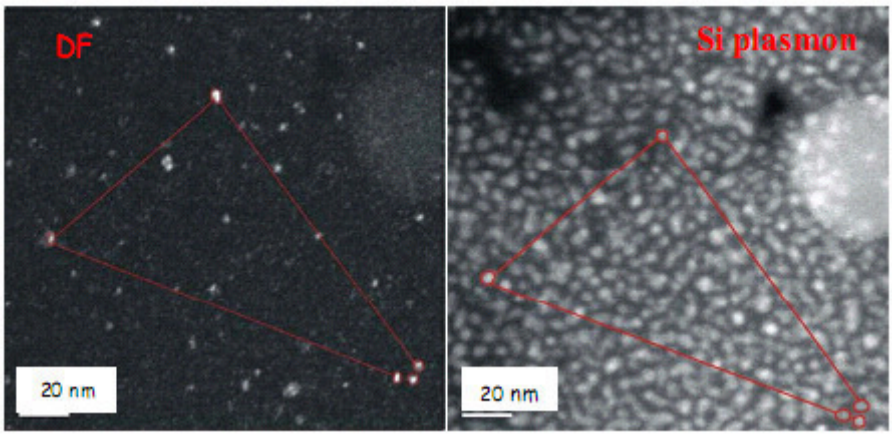

Figure 2. 20 - A comparison between two images of an identical portion of a sample containing Si-nc obtained applying the dark field and the energy filtered transmission electron microscopy techniques.

In the dark field image the contrast in the image is due to those electrons diffracted by crystalline planes, which satisfy the Bragg law:

$$n\lambda = 2d \sin\theta \qquad (2.19)$$

here λ is the wavelength associated to the incoming electrons, d is the distance between the reflecting atomic planes, n is an integer number and θ is the incidence angle. In these conditions, only strongly diffracting regions of the specimen would appear bright relative to the surrounding.

The energy filtered picture instead has been achieved by selecting those electrons that have lost energy via plasmonic-interaction with the Si present in the sample. The EFTEM picture, being a chemical map, reveals as bright spots all the Si precipitates within the sample without regard whether they are crystalline or amorphous and without regard of the relative angle between the crystalline planes and the incident beam. On the contrary, the dark field image presents only a small fraction of those crystalline grains which have their [111] planes in almost exact Bragg condition.

In the present work, the EFTEM investigation was carried out with a 200kV Jeol 2010F microscope equipped with Schottky field-emission electron gun, an ultrahigh-resolution objective lens pole piece with a small spherical aberration coefficient (C_s = 0.5mm), and a Gatan imaging filter (GIF).

This investigation has been operated by the Italian Research Council - IMM at Catania, and it was performed on samples deposited on c-Si substrate.

CHAPTER 3

Properties of as-deposited SiN_X thin films

Quantum dots, and silicon quantum dots in particular, can be grown by several methods. A well-established approach consists in depositing alternating layers of stoichiometric Si-based material (silicon oxide, nitride or carbide) and silicon-rich layers of the same material, and afterwards performing high temperature treatments (≥ 1100°C) [1, 2]. This procedure has the advantage of allowing to easily control the dot size by fixing the Si-rich layer thickness. However, quantum confinement effect has been also shown in as-deposited SiN_x thin films fabricated by plasma enhanced chemical vapour deposition (PECVD) at 300°C, where spontaneous formation of Si nanostructures has been evidenced through TEM analysis (with no need of post-deposition high temperature annealing) [3, 4]. This approach is particularly promising, since it allows for use of low cost substrates and in principle makes the use of such nano-engineered materials easily feasible within classical thin film silicon solar cell architectures.

In this chapter the possible spontaneous formation of homogeneously-distributed silicon quantum dots in silicon nitride films grown by PECVD is investigated. The films have been characterized by optical absorption, photoluminescence (PL), Raman spectroscopy and energy-filtered transmission electron microscopy (EFTEM). The evolution of the various properties when changing deposition parameters like gas flow rates and chamber pressure will be discussed.

3.1 SiN_x growth by PECVD

The silicon nitride films presented in this thesis have been deposited both on transparent substrates (glass, quartz) and on *c*-Si wafers, in a PECVD chamber working at standard frequency (13.56 MHz) within a cluster tool deposition system (MVSystems Inc., Golden, Colorado USA) (fig. 3.1).

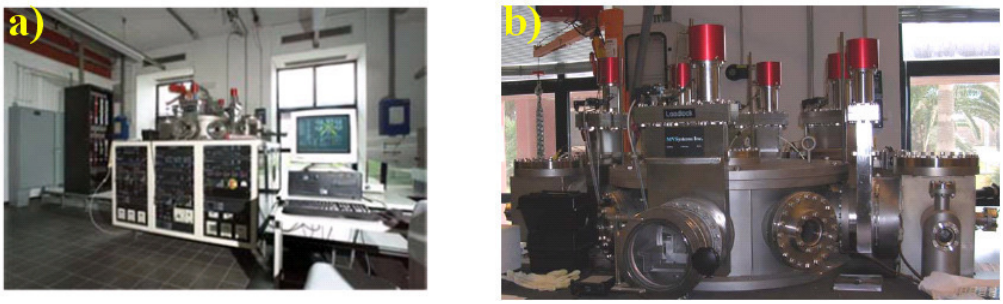

Figure 3. 1 – a) MVSystems Inc. (USA) cluster tool system; **b)** Zoom on the deposition chambers and load lock.

Two different gas mixtures have been considered: SiH_4 and N_2 in one case and SiH_4, N_2 and NH_3 in the other. The two types of samples will be called nitrogen-type and ammonia-type (or N_2-type and NH_3-type) respectively.

The reactant gases are introduced into the evacuated chamber and there dissociated, with the resultant species driven toward the heated substrate held at 300°C in all cases. The electrode configuration consists of a 13 cm × 13 cm powered electrode and a 11 cm × 11 cm substrate carrier as the grounded electrode. The inter-electrode distance is kept at 17 mm, and the gas supply is a simple cross-flow geometry.

A low growth rate regime, that seems to be a key condition to promote the formation of nanostructures [5], has been selected. This regime is characterized by low power (fixed at 0.3 W) and gaseous mixtures highly diluted in nitrogen, with the gas flow rates changed in appropriate ranges. It has indeed been claimed that inhomogeneous growth, with spontaneous aggregation of Si quantum dots, is promoted in this regime by formation of Si dangling bonds

acting as nucleation sites for the aggregation of silicon clusters in silicon nitride films during the growth process. In particular, the increase of N_2 or NH_3 flow rate (at fixed SiH_4 flow rate) or the decrease of deposition pressure was shown to influence size and density of Si QDs by enhancing the creation of such sites and then favouring the realization of densely packed but smaller silicon clusters around them (fig. 3.2) [6].

For the N_2-type samples a SiH_4 flow rate of 0.2 sccm has been used, whereas the N_2 flow rate has been varied in the range 8 - 180 sccm. In the other case a fixed flow rate for SiH_4 and N_2 (2 sccm and 40 sccm respectively), and a variable flow rate for NH_3 in between 1.5 and 9 sccm have been used. For both types of samples the large N_2 flow rate serves to dilute the gas mixture (in order to keep the growth rate low), while its change in the first case and the variable NH_3 flow rate in the other case allow to control the silicon content in the layers. In all cases the thickness of the films, evaluated with a step profiler, has been kept around 200 nm [7, 8]. Depending on the deposition conditions, growth rate values in between 0.4 and 0.7 Å/s have been obtained for the samples grown with N_2. Larger values, in between 1.2 and 1.5 Å/s have been obtained in the other case, due to the larger silane flow rate and the use of ammonia, easier to dissociate.

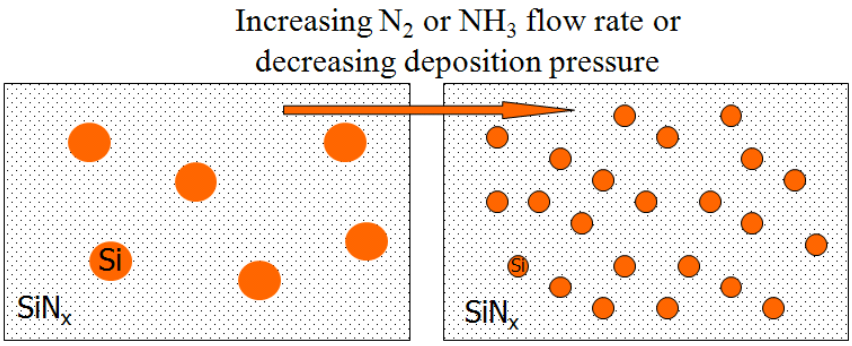

Figure 3. 2 – Schematic of the in-situ growth of Si-QDs with different gas flow rates or deposition pressure.

The samples deposited on glass/quartz change from highly transparent to yellowish / brown colour when the N_2 or NH_3 flow rate is reduced, or the pressure is increased, as shown in fig 3.3. Such variation is an evidence of the increasing silicon content in the films making the material less transparent to the radiation. Correspondently, the refraction index of the films, evaluated from the interference fringes in the transmittance spectra located around 600 - 700 nm, gradually increases from 1.9, close to the value of stoichiometric silicon nitride [9], to 3.4, typical of silicon rich silicon nitride.

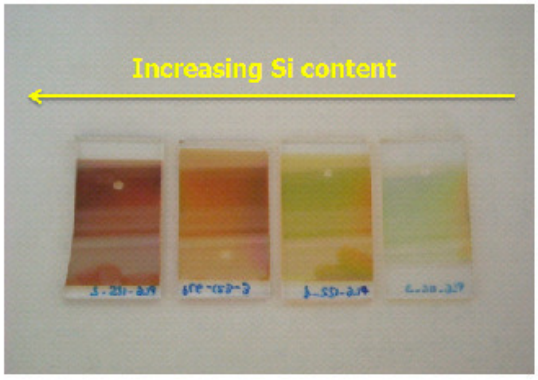

Figure 3. 3 – Change of colour when decreasing the N_2 or NH_3 flow rate or increasing the deposition pressure.

3.2 Photoluminescence data and quantum confinement

Spectroscopic photoluminescence is an extensively used tool to explore quantum confinement effects from nanostructures. As previously mentioned in chapter 2, investigation of quantum confinement from silicon nanocrystals typically relies on PL measurements as a first step. In this paragraph, the PL evolution from silicon nitride films is monitored when changing either the gas mixture or the gas pressure.

3.2.1 Evolution of photoluminescence when varying the gas mixture

In this section the effects of the N_2 and NH_3 flow rate changes (in the ranges 8 – 180 sccm and 1.5 – 9 sccm, respectively) at fixed pressure (0.5 Torr) are reported.

All the samples show room temperature luminescence in the visible range. The evolution of the PL peak position for N_2-type and NH_3-type sample series is shown in fig. 3.4 (a) and (b) respectively. The PL spectra are characterized by one clear emission peak (a double peak is observed only for the sample grown with the highest N_2 flow rate). When changing the stoichiometry of the films, a blueshift is observed for decreasing silicon content, realized by increasing the N_2 flow rate (a) or the NH_3 flow rate (b).

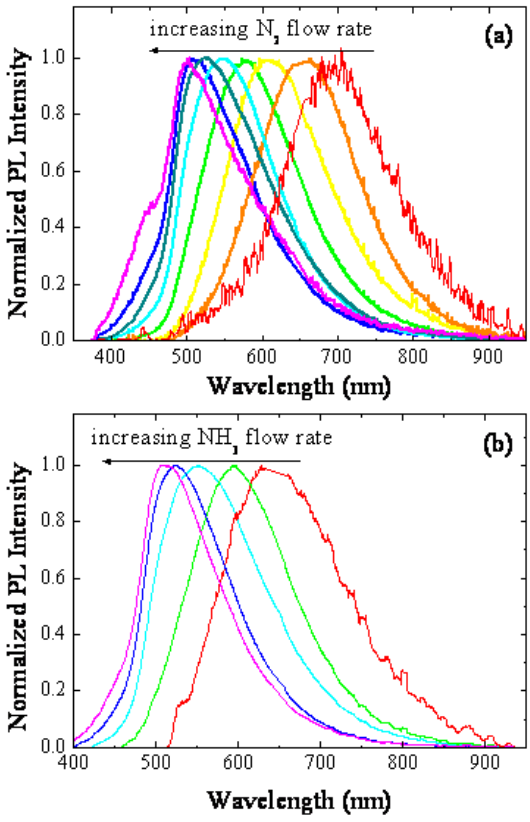

Figure 3. 4 – Normalized PL spectra (excited at 325 nm) for N_2-type **(a)** and NH_3-type **(b)** samples.

The origin of PL in SiN_x films is still an object of debate. In defect-related models, the PL peak position cannot be easily controlled because the peak position is observed only near the defect energy levels. Robertsons [10] has defined possible defects that could be involved in radiative recombination in silicon nitride. According to Robertson's theoretical predictions, there are two nitrogen defect states that give rise to levels within the gap, namely N_4^+ and N_2^0, that have been calculated to be near the conduction and valence band, respectively. Also Si dangling bonds should be considered.

Based on Robertson's work [10], Deshpande [11] proposed the model shown in fig. 3.5 giving rise to luminescence at three different energies (1.8, 2.5 and 3 eV). When the samples are amorphous and have varying optical band gaps (depending on the film composition), the energy levels are not very well defined. Furthermore, there is a distribution of states for a given defect giving rise to broad features in the PL spectra.

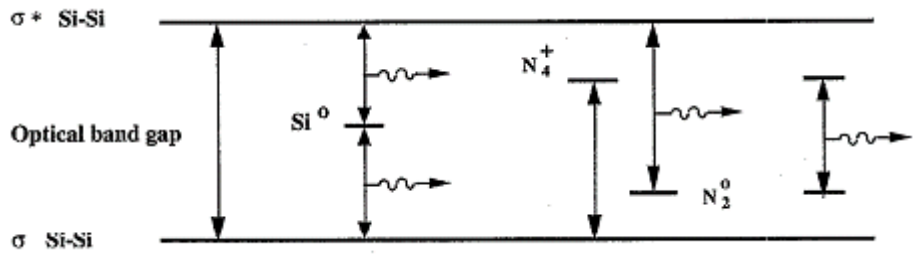

Figure 3. 5 - Model for photoluminescence from radiative defects in *a*-SiN_x:H films [11].

The static disorder model, within the Dunstain and Boulitrop theory [12, 13], instead, attributes the PL line-shape to the band-tail states (fig. 3.6). In this model, the carriers are radiatively recombining within the localized states at the band-tails of the alloy gap. As the nitrogen content increases, the band-gap energy also increases, which leads to a blueshift of the PL energy [14].

In case of non-homogeneous material embedding Si nanoparticles, the PL mechanism could be dictated by quantum confinement. In this model the PL peak position is dependent on the Si-QDs size as shown in Refs. [3], [5], and [15], where the PL peak position could be tuned by controlling the size of Si-

QDs via modulation of growth parameters like N_2 or NH_3 gas flow rate or the pressure. The quantum confinement effect increases the Si inclusions bandgap as their size decreases, which results in a blueshift in optical luminescence and absorption energy.

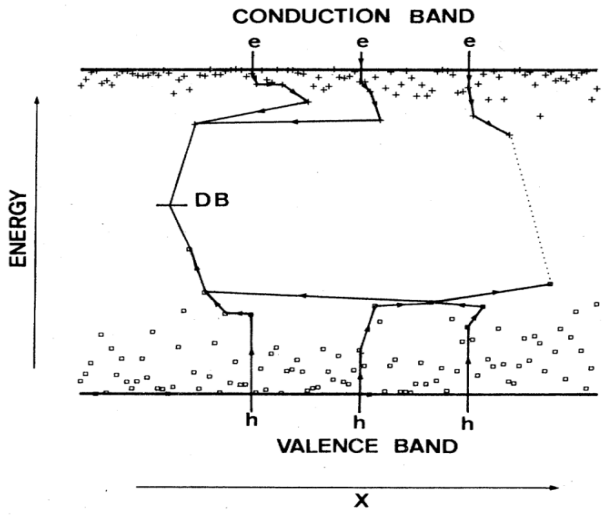

Figure 3. 6 – The static disorder model.

In our case, the controllable dependence of the PL peak position on nitrogen or ammonia flow rate should rule out the possibility of PL emission from radiative defects in the silicon nitride matrix, observed around well defined energy values [11]. In analogy with the results reported in the literature on samples grown in the same conditions [5] the systematic PL evolution has been ascribed to quantum confinement.

In fig. 3.4 (a) and (b), the PL peak blueshift with increasing N_2 or NH_3 gas flow rate could then be interpreted as evidence of the enlargement of the energy gap of Si dots (spontaneously formed in the films) as their size decreases.

At the same time, the variation of dot density as the deposition conditions are varied (as an effect of varied number of nucleation sites) can furnish an explanation to the observed change of the PL peak intensity (fig. 3.7).

Less intense luminescence is indeed found with samples grown with low N_2 or NH_3 flow rate in the mixture (condition for having few nucleation sites during

the film growth). Larger intensities are found for intermediate values, while for higher flow rates the response decreases again: with very low silane partial pressure and many Si dangling bonds there are not enough Si atoms that can aggregate around all the nucleation sites [16].

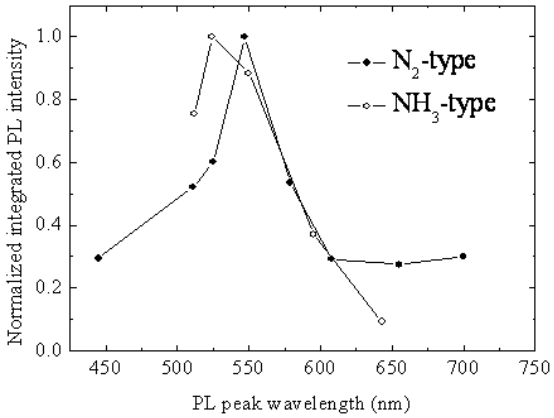

Figure 3. 7 - Normalized integrated PL intensity for N_2-type (solid symbol) and NH_3-type (open symbol) samples.

The presence of a large number of silicon dangling bonds, when high N_2 flow rate is used, could explain the presence of the double luminescence peak observed in fig. 3.4 (a) for the sample grown with the highest N_2 flow rate (180 sccm), where the peak around 500 nm (~2.5 eV) could be associated to radiative recombination at metastable silicon dangling bonds located about midgap [11]. The highest energy peak could be related to very small silicon dots, however the large intensity of the 2.5 eV peak implies a very defective material.

While the PL evolution is similar for both types of samples, the intensity is much stronger in the ammonia-type case (fig. 3.8). The enhanced luminescence has been reported also in [4], where it was related to the extra hydrogen available during the growth process when NH_3 is used in the gas mixture [4]. The effect of this extra hydrogen would be to more efficiently passivate nonradiative defect centres at the surface of the silicon dots.

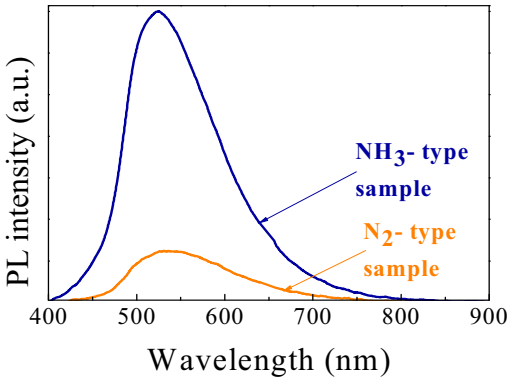

Figure 3. 8 - Comparison of samples with maximum PL intensity within each series.

3.2.2 Evolution of photoluminescence when varying the gas pressure

N_2-type and NH_3-type sample series have been deposited at fixed gas flow rates, while different pressure values have been adopted in the range 0.3 - 1 Torr.

All the samples show clear room temperature PL. Tuning of PL emission with controlled changes of pressure for N_2-type and NH_3-type samples is reported in fig. 3.9 (a) and (b), respectively. Again for both types of samples the PL peak shifts from the blue to the red region of the visible spectrum with larger refraction index, and then larger silicon content, in the layers. Also the PL intensity changes, showing a maximum for some intermediate pressure value, as already seen in the previous section when varying the gas flow rates.

Again we have attempted a description of the evolution of the PL spectra as proposed in ref. [5] since we have adopted similar deposition conditions.

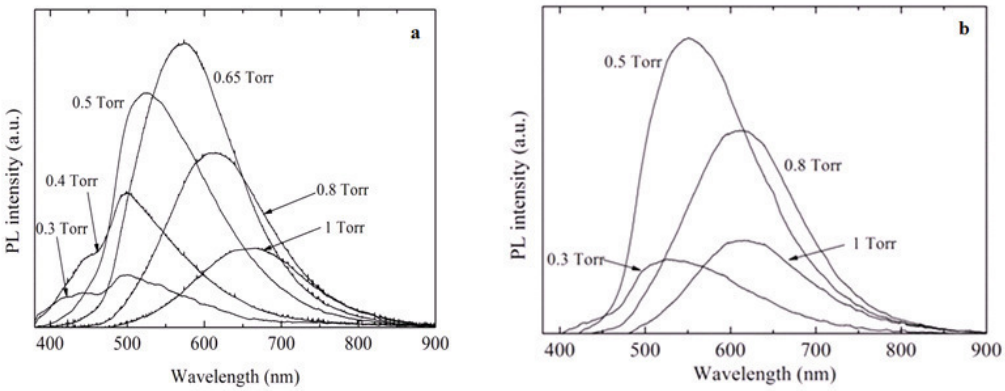

Figure 3. 9 - PL spectra excited at 325 nm for N_2-type samples **(a)** and NH_3-type samples **(b)** grown at fixed gas flow rates with different pressure values.

For a clearer comparison, the shift of the PL peak with pressure for the two sample series is reported in fig. 3.10.

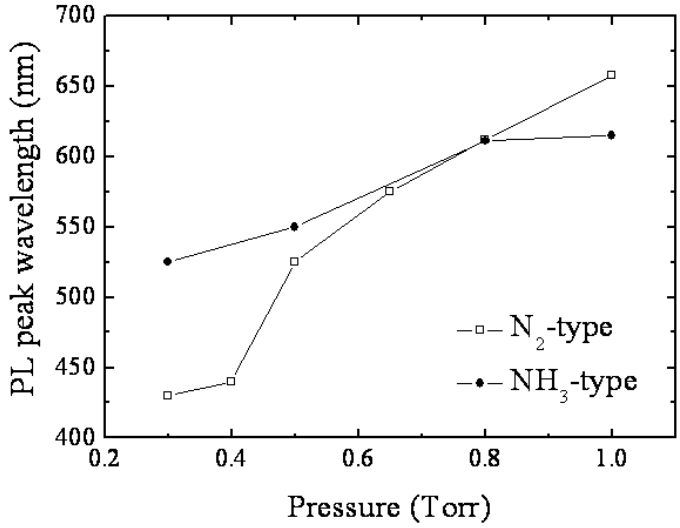

Figure 3. 10 - The shift of the PL peak with pressure for N_2-type and NH_3-type samples.

In general we have found that a pressure increase gives rise to a PL shift towards higher wavelengths, but clearly the pressure has stronger effect in the N_2 case, where the PL peak moves from 430 to 658 nm, while for the ammonia-type samples the spanned range is 525 - 615 nm. The difference can be ascribed to the different behaviour of the gas mixtures with regard to the formation of precursor molecules within the plasma. In the low power regime

used in this work, N_2 stays unactivated and mostly acts as a diluent, while the NH_3 molecule, like SiH_4, is easily dissociated. When only SiH_4 and N_2 are used, with a pressure reduction, lower silane partial pressure is available. Then, the amount of dissociated N_2 molecules, which is not that sensitive on pressure variations, weighs more during the deposition process, enhancing the number of nucleation sites. With the other gas mixture, the partial pressures of the species derived by the dissociation of both SiH_4 and NH_3 are reduced when pressure is lowered, and the effect on the formation of nucleation sites is milder [8].

As already seen with changes of the gas flow rates, also in this case the PL intensity evolution can be explained in terms of dot density variation. Samples grown with a high pressure in the mixture (condition for having few nucleation sites during the film growth) have indeed less intense luminescence, while larger intensities are found when the pressure is decreased (fig. 3.9). However, for very low pressure the response decreases again. It is plausible that for such samples, grown with very low silane partial pressure, there are not enough Si atoms that can aggregate around all the Si dangling bonds, thus resulting in a lower dot density. Such behaviour means that an optimal deposition condition allowing for the realization of high Si dot density combined with intermediate dot size can be identified. The maximum intensity in the N_2 and in NH_3 flow rate series is obtained around 0.5 Torr.

3.3 Structural and morphological analysis: Raman spectroscopy, FTIR, TEM

In the previous section, following some literature [5], presence of Si-QDs in the samples was assumed on the basis of:

1) adoption of the same deposition regime;
2) observation of the same PL evolution.

We have also searched for indirect and direct evidence of a phase separation within the material. Here we focus on structural and morphological analysis of the films.

From now on, we will focus on sample series deposited at fixed pressure and varying gas flow rates. We have, in fact, observed in the previous sections that changing the flow rate ratios (N_2/SiH_4 or NH_3/SiH_4) or the pressure during film growth gives in both cases the means for changing the material stoichiometry. In particular, the results for a N_2-type series will be presented, with samples named from A (the Si richest) to E.

The Si excess presents in the film has been studied by Rutherford backscattering spectroscopy (RBS) when changing the gas flow ratio. The RBS analysis has been carried out on selected samples within the series and the measurements have been performed at CNR-IMM-MATIS, Catania. Since the PECVD-grown material has non negligible hydrogen content that affects the elemental composition analysis, to overcome this problem the measurements have been performed on samples annealed at high temperature (1100°C), where hydrogen has effused. The material is clearly silicon rich in all cases. A mild silicon excess is deduced, up to about 16 % for the material grown with the lowest N_2 flow rate (sample A).

The FTIR spectra of the chosen series is shown in fig. 3.11. Mainly two absorption bands are present: the Si-N asymmetric stretching mode at 830 cm^{-1} and Si-H stretching mode 2100 cm^{-1}, respectively [17]. Some hint of the N-H rocking mode around 1150 cm^{-1} can be also identified.

A decrease of the intensity of the Si-N peak and of the width of the normalized absorption relative to Si-N band (inset on the right in fig. 3.11) with increasing silicon content is evident as an obvious consequence of the reduced number of Si-N bonds when less nitrogen is included in the film. Also a shift of the Si-H stretching mode towards lower wavenumbers is present (inset on the left in fig. 3.11), again due to the lower nitrogen content. In fact, the vibration frequency of the peak at 2100 cm^{-1} depends on the neighboring environment. In correspondence to a lower electronegativity due to the decreased number of N

atoms bond to the same Si, the peak of the Si-H band shifts to lower wavenumbers [18 - 20].

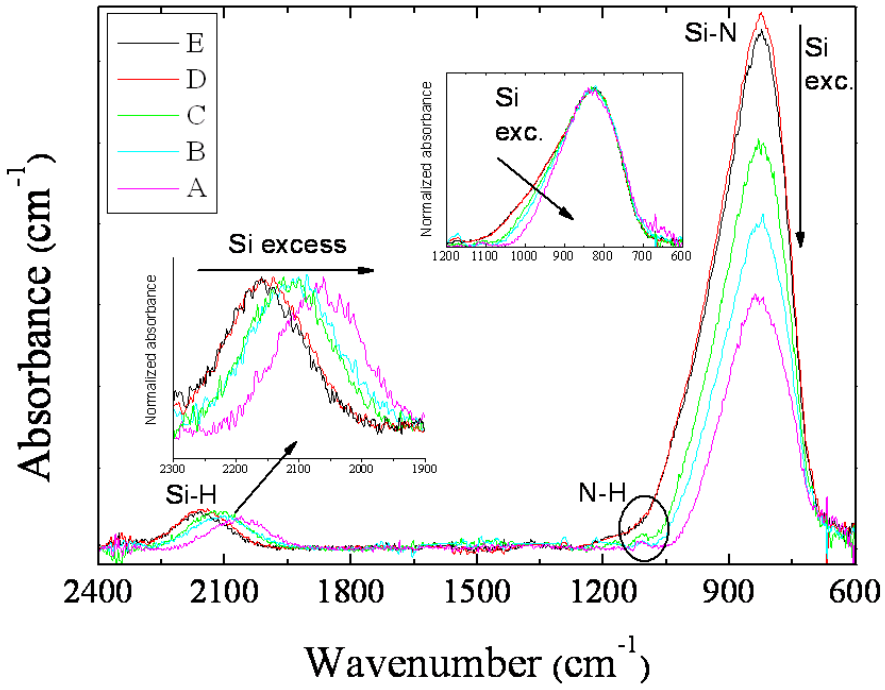

Figure 3. 11 – FTIR spectra of samples with different Si content. **The inset on the left** is the zoom of the Si-H peak, while **the inset on the right** is the normalized absorbance of the Si-N peak.

Raman spectroscopy has been applied to thin films grown on quartz to obtain information about the presence of silicon nanoparticles within the silicon nitride matrix and their amorphous or crystalline structure. The Raman spectra of sample A, after the subtraction of the substrate contribution, is shown in fig. 3.12. For the other samples from B to E the Raman signal is increasingly more difficult to detect due to the decreasing Si content and the high transparency that makes the signal too low with respect to the substrate contribution.

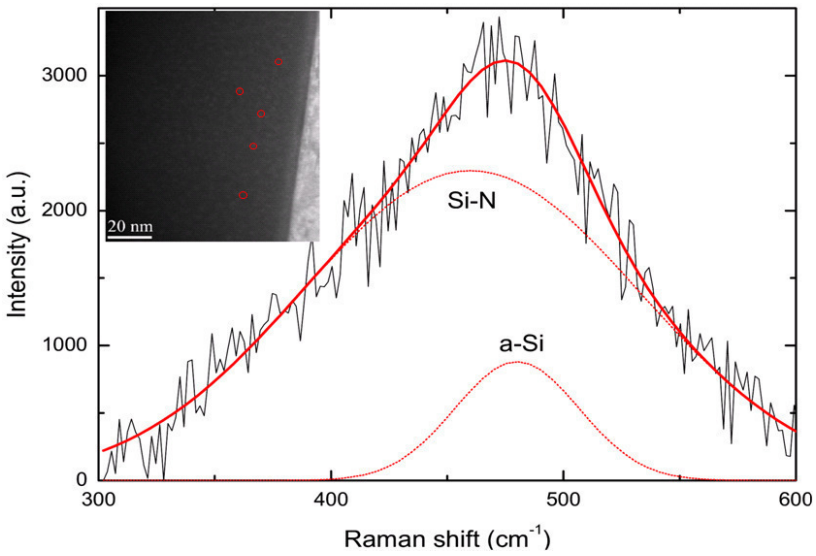

Figure 3. 12 - Raman spectrum of sample A (black line). The thick solid red line is the curve obtained as convolution of the Si-N and *a*-Si Gaussian bands (red dotted lines) centered at 460 and 480 cm^{-1} respectively. **Inset:** EFTEM image acquired 4s after selecting the area: The small light spots correspond to *a*-Si nanoclusters induced as an effect of the electronic annealing (they are absent in the image acquired immediately after selecting the area). Some spots have been evidenced by red circles.

A peak centred at about 480 cm^{-1}, the position of the TO mode for amorphous silicon (*a*-Si), is found. The band is rather wide and asymmetric with a tail extending towards the low wavenumbers, probably due to the large disorder caused by the presence of N atoms within silicon aggregates [21]. A tentative deconvolution of the peak is shown in red in fig. 3.12. The two Gaussian bands centred at 465 cm^{-1} and 480 cm^{-1} (thin red lines) can be assigned to Si-N and *a*-Si modes respectively. Possible presence of *a*-Si clusters could then be deduced. A partially phase-separated structure, constituted by a mixture of a silicon-rich phase and a phase containing more nitrogen, as proposed in ref. [22], is however more plausible. In fact, a homogeneous structure is revealed by EFTEM. It is interesting to note that the material is strongly unstable under electronic irradiation. Very quick formation of pure *a*-Si nanoclusters can be induced simply as an effect of the electronic annealing [23]. The inset to fig. 3.12 is a transverse image from sample A acquired only after 4 seconds of irradiation that shows induced formation of *a*-Si dots.

3.4 Optical absorption properties

The absorption properties of the same N_2-type sample series, discussed in section 3.3, is shown in fig. 3.13. The absorption curves of a 200 nm thick PECVD-grown hydrogenated *a*-Si film and tabulated Si_3N_4 [24] are also shown for reference. In general, with systematic change of Si content, the known tuning of $\alpha(E)$ in between the *a*-Si and Si_3N_4 limits [14] is obtained as expected when weakly absorbing Si-N bonds gradually replace the strongly absorbing Si-Si bonds [25].

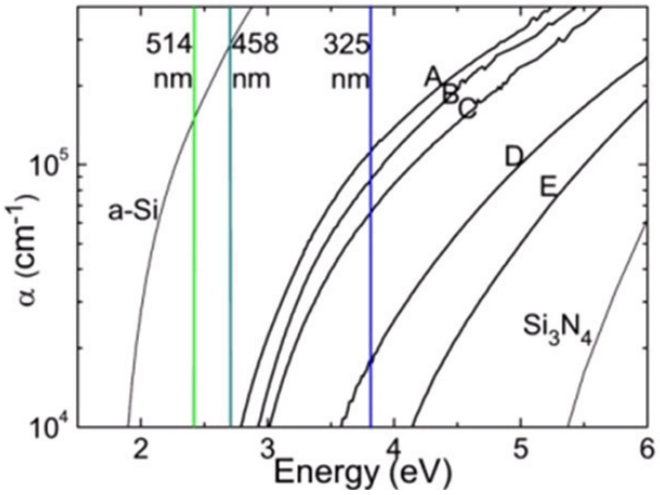

Figure 3. 13 – Absorption coefficient spectra of samples grown with increasing Si content going from right to left (E to A). The vertical lines indicate the energies used in the PL experiments discussed in the next section.

Because of the presence of localized states between valence and conduction band, the optical gap is an ill-defined parameter in amorphous semiconductors. For tetrahedrally bonded semiconductors the so-called Tauc gap (E_g) is typically used, defined through the expression:

$$(\alpha h\nu)^{1/2} = B\left(h\nu - E_g\right) \qquad (3.1)$$

where α is the absorption coefficient, $h\nu$ the incoming photon energy, and B a coefficient that includes information on the convolution of conduction and valence bands and on the matrix element of optical transitions [26]. This formula is valid in the high-photon-energy range, the so-called intrinsic region involving transitions between extended electronic states. The gap value and B coefficient are extracted through the Tauc plot for α higher than $1 \cdot 10^4$ cm^{-1} by fitting the data to a straight line. Figure 3.14 shows the evolution of the Tauc parameter B and the energy-gap: E_g increases from 2.5 to 3.5 when decreasing the Si content, and meanwhile B decreases. Even if at energy levels where the Tauc model applies ($\alpha \geq 10^4$ cm^{-1}) the joint density of states does not include the disorder induced tail states, this B dependence can be interpreted as a signal of the growingly larger disorder in the material with N alloying [27], that manifests with broadened tails. In fact, the Tauc parameter B can be in some cases associated with the topological disorder and with the band-edge modification [28 - 30].

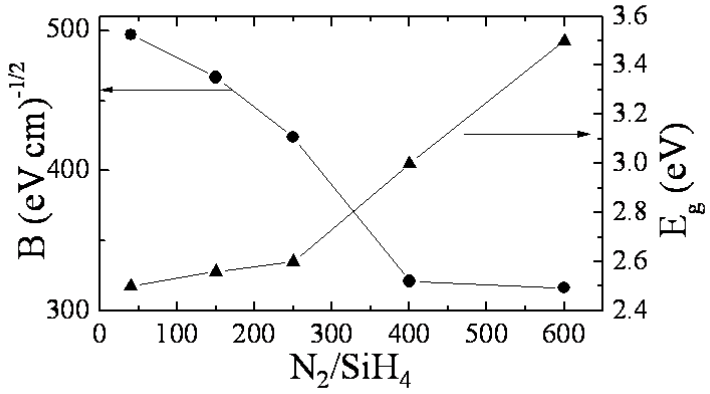

Figure 3. 14 - Evolution with alloying (expressed in terms of nitrogen to silane flow rate ratio) of energy gap values extracted from the upper and lower energy regions in the Tauc plot and the Tauc parameter B.

Similar evolution of the optical absorption properties is observed with NH_3-type samples. In fig. 3.15 two absorption spectra for each type of samples are shown. The curves correspond to sample with similar refraction index (2.0 and 2.3) and photoluminescence response (PL peak energy, E_{PL}, around 1.90 and

2.35 eV). The experimental data are reported together with the absorption curves of a 200 nm thick PECVD grown hydrogenated *a*-Si film and tabulated Si_3N_4 [24], shown for reference.

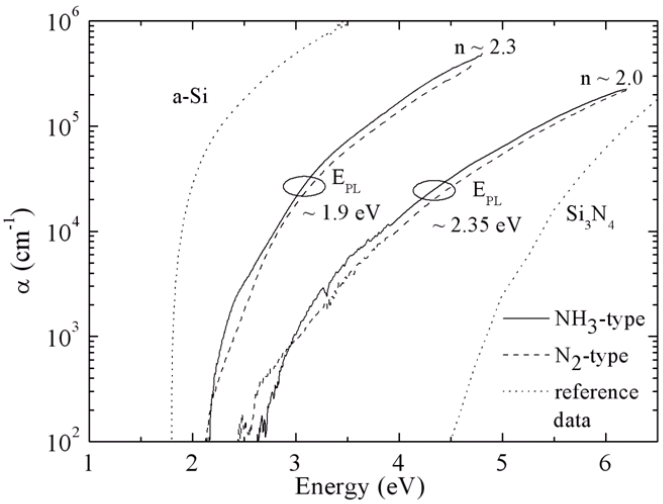

Figure 3. 15 - Absorption coefficient for N_2 (dashed lines) and NH_3-type samples (solid lines) characterized by similar refraction index, *n*, and PL peak energy, E_{PL}. The absorption curves of a PECVD grown *a*-Si film, and tabulated Si_3N_4 [24] are also shown for reference (dotted lines).

The curves look almost the same, with a behaviour in between the *a*-Si:H and tabulated Si_3N_4 curves. With n ~ 2.0, not far from stoichiometric case (n ~ 1.9 for hydrogenated material), the absorption spectra are already very different from the Si_3N_4 curve. The main difference is in the low energy side of the spectrum, where our curves seem to be pulled toward the *a*-Si spectrum. In this discussion it should be considered that, for an accurate determination of α below ~ 10^4 cm^{-1}, other techniques should be applied (like photothermal deflection spectrometry (PDS)). However some rough evolution can still be performed.

Theoretically, in case of some phase separation versus a random bonding model, where Si-Si and Si-N bonds are homogeneously dispersed throughout the alloy, the presence of strongly absorbing Si regions enhances the low energy optical absorption [25].Our results are then compatible with the partial phase separation proposed to explain the Raman data.

Finally, using E_{02}, the energy value at which the absorption coefficient is equal to 10^2 cm^{-1}, as an estimate of the absorption rising edge of the material, a value very close to the PL peak energy is obtained in all cases (the average difference is $E_{02} - E_{PL} \sim 250$ meV) (fig. 3.15 and ref. [8]). This could indicate a mechanism for light emission related to the material tail states.

3.5 PL at different excitation energies and different temperatures

A deeper study on the PL properties has been performed by varying excitation energy and temperature in order to shed some light on the mechanisms governing the luminescence of such materials [31], since this is still a matter of debate.

Samples with different stoichiometry have been investigated. In particular, we show the results for the N_2-type series, whose absorption curves were reported in fig. 3.13, in the section 3.4.

Room temperature photoluminescence has been excited at high energy (above gap), with the 325 nm line of a He-Cd laser source, and at low energy (below gap), with the 514 nm line of Ar^+ (vertical lines in fig. 3.13). PL emission has been also studied also at different temperatures, from room temperature down to 12K, with the 458 nm line of an Ar^+ laser, at the Lyon Institute of Nanotechnology (INL) in France. Different setups have been used in the three cases. With excitation at 325 nm the PL response is collected by an optic guide and registered in the visible range by a calibrated CCD spectrometer (OCEAN-OPTICS S2000). The measurement at 514 nm is performed with a Renishaw inVia Raman microscope. With excitation at 458 nm, light emission is detected with a Jobin-Yvon iHR320 spectrometer coupled to a liquid nitrogen-cooled CCD Hamamatsu camera. In all cases the spectra were corrected for the spectral response of the system.

3.5.1 Room temperature PL at different excitation energies

The tuning of the absorption properties described in the previous section is accompanied by a tuning of the emission spectra. Figure 3.16 shows the PL emission at room temperature of all the samples excited above gap (or close to it for the most transparent film) at 325 nm, as shown by the blue line in fig. 3.13.

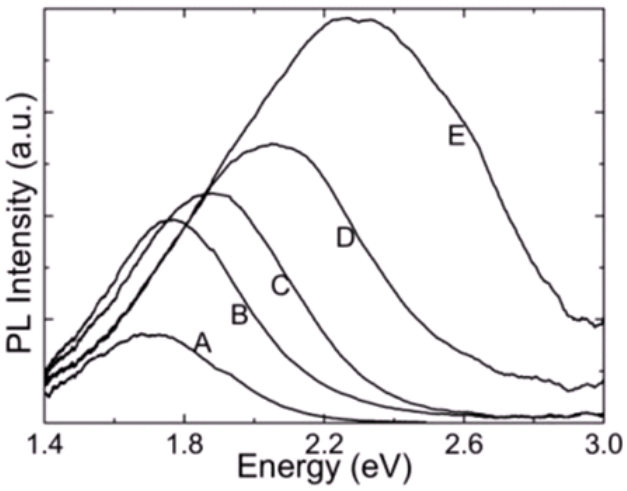

Figure 3. 16 – PL intensity excited at 325 nm for the samples with increasing Si excess going from right to left (E to A).

The emission energy falls in the visible range (1.7 - 2.3 eV) and systematically blue-shifts with decreasing Si content (increasing N_2/SiH_4 flow rate ratio), as already observed with other samples in the previous sections meanwhile intensity increases going from sample A to E.

Figure 3.17 (a) and (b) summarize peak energy (E_{PL}) and bandwidth (ΔE_{PL}) evolutions with N_2/SiH_4 compared to E_g e B respectively from the Tauc plot. The systematic blueshift of E_{PL} follows the E_g increase with decreasing Si content, while ΔE_{PL} increases jointly with the B parameter reduction. With such dependences the dominating PL mechanism is likely the radiative recombination occurring after thermalization of the excited carriers in deep localized tail states [22, 32, 33]. In this case the tunable emission simply

follows from the gap enlargement with nitrogen alloying, while the systematic broadening of the PL spectra is linked with the increasingly larger tails.

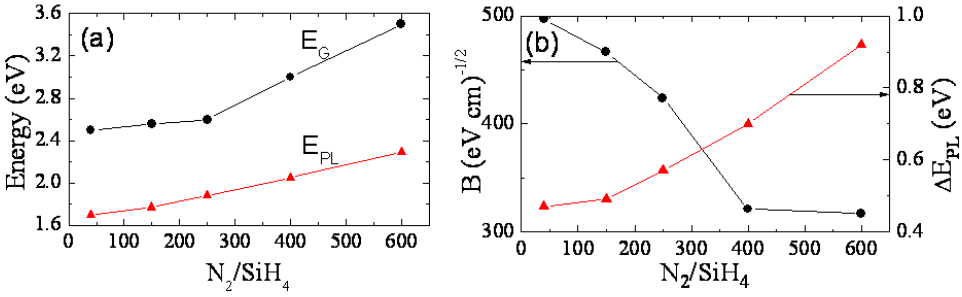

Figure 3. 17 – (a) Evolution with alloying (expressed in terms of nitrogen to silane flow rate ratio) of energy values extracted from the upper and lower regions in the Tauc plot and PL peak energy measured at 325 nm. **(b)** Evolution of Tauc coefficient *B* and PL bandwidth ΔE_{PL} measured at 325 nm.

When lowering the excitation energy within the tails, a red-shift of the emission curve is expected, since deeper localized states are selected [33]. The PL spectra excited at 514 nm are indeed downshifted (fig. 3.18), but with the peculiarity that the response is peaked around 1.7 eV independently on the stoichiometry and is narrower.

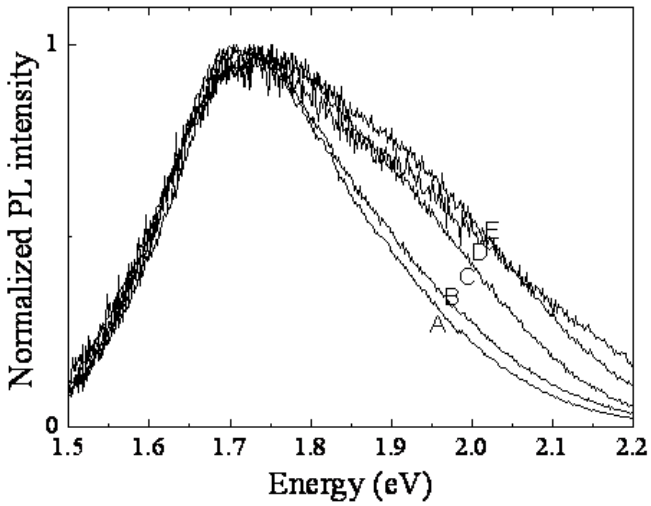

Figure 3. 18 - Normalized PL intensity excited at 514 nm for the samples with increasing Si excess going from right to left (E to A).

In presence of partial phase separation, gap fluctuations due to the compositional dishomogeneity are expected (fig. 3.19) with spatial variation of both gap energy and tail widths. In this case similar response can be reasonably expected for all the samples, with the subgap light absorbed only within the volumes with lower gaps (Si rich regions).

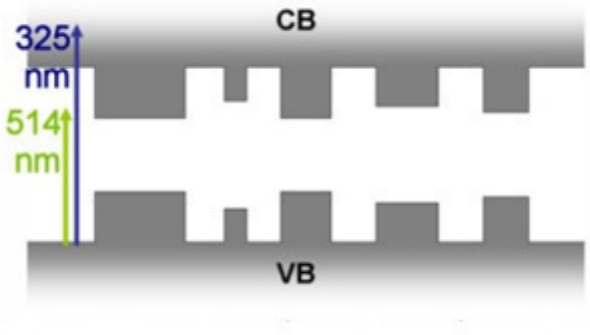

Figure 3. 19 - Schematic illustration of the gap fluctuations.

For the samples with large Si content, where reduced gap variation among the different spatial regions is expected, almost no difference is found in E_{PL} (fig. 3.20), but the band with above gap excitation is wider, especially on the low energy side. Contribution from a wider varieties of states is clearly obtained since the excited carriers do not experience the "fine structure" of the gap and, accessing all spatial regions, can explore all the tail states, including deep states of the nitrogen richer matrix. With the low energy source, excitation and emission selectively occur instead in the Si rich regions only. In this case the excited carriers cannot thermalize everywhere through the whole range of tail states and then their behaviour depends on the local density of states of the region in which they are excited.

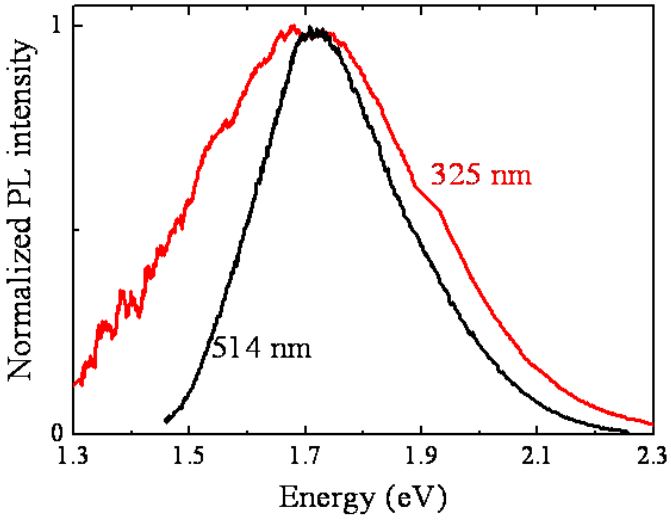

Figure 3. 20 - Comparison of normalized PL spectra of sample A under excitation at 514 nm and 325 nm.

In low-dimensional amorphous semiconductor volumes the number of tail states is strongly reduced and, accordingly, direct band to band recombination could be the dominant process [34]. The emission is indeed peaked around the gap value of hydrogenated *a*-Si [27, 33, 35], blue-shifted but also significantly enhanced with respect to bulk *a*-Si [35], thanks to a likely larger radiative rate. In this picture the peak asymmetry with a sort of cut off on the low energy side (fig. 3.18) would be dictated by this process, while smaller clusters (with tentative diameters below 3 nm) [3, 34] would contribute to the emission at higher energy as an effect of the enlarged gap because of quantum confinement. The diminishing shoulder on the high energy side, moving from sample E to A, would be due to the ripening of the smaller quasi-Si clusters when the Si excess is raised.

3.5.2 Temperature evolution of the photoluminescence

In order to gain more insight on the light-emitting mechanism, the temperature evolution of the PL band excited at 458 nm has been also investigated. No peak shift is observed: The temperature dependence of the peak position in *a*-SiN_x is

highly dependent on the alloying and not as pronounced as in *a*-Si [33]. Already in earlier work this was interpreted invoking long range potential fluctuations (non-homogeneous material) [33]. Figure 3.21 shows the integrated PL intensity for two samples at different excitation levels. The curves are normalized with respect to the room temperature value. With *a*-SiN_x a flat low temperature region followed by a roughly exponential fall is usually observed [32, 33, 36]. This is indeed the behaviour observed with samples with lower silicon excess (the red squares in fig. 3.21 correspond to sample C excited at 11 mW). The data can be described with a simple phenomenological model based on thermally activated diffusion of carriers (thermal ionization of excited carriers from the exponential tails to the mobility edge and then lost to radiative emission). According to this model, the temperature dependent PL intensity at a given temperature *I(T)* can be expressed as:

$$I(T) = I_0/[1 + \beta_a \exp(-E_a/k_B T)] \qquad (3.2)$$

where I_0 is the low temperature PL intensity, β_a is a constant directly proportional to the ionization rate and inversely to the radiative rate, and E_a is the activation barrier or ionization energy [11, 33].

The red solid line in fig. 3.21 is the fit of sample C data to this model, with β_a = 50 and E_a = 85 meV.

The sample with larger Si excess (A) shows, instead, peculiar intensity evolution depending on the excitation intensity. The solid and open black circles in fig. 3.21 correspond to incident power of 200 mW and 11 mW respectively. Under high excitation intensity the temperature dependence is bell-shaped (with maximum intensity at 100K) as found for Si nanoparticles, both crystalline and amorphous, embedded in SiO_2 matrices [21, 37, 38] or for porous Si [39]. In particular, the result closely resembles the data reported for amorphous silicon nanoclusters in SiO_x [38], with a difference between the maximum luminescence intensity at 100K and the room temperature value of a factor of five. At low power the bell-shaped behaviour disappears.

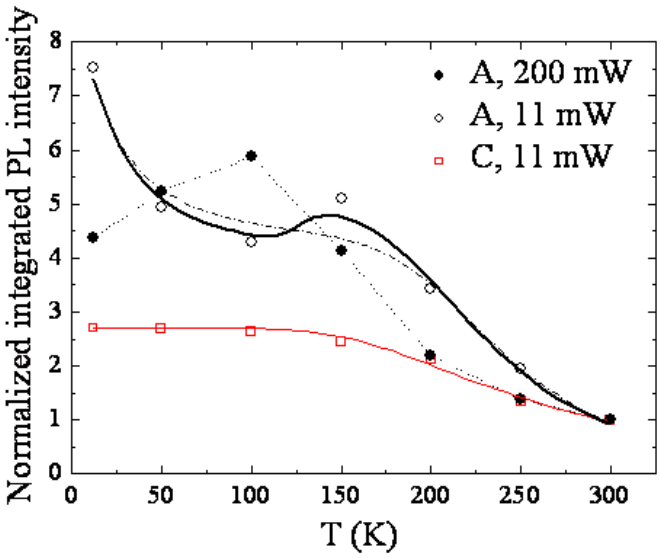

Figure 3. 21 - Temperature dependence of the integrated PL intensity of two representative samples (A, circles, and C, squares) excited at 458 nm at 200 mW and 11 mW. The data are normalized with respect to the room temperature value. The thin dotted line is a guide to the eye. The red solid line is the theoretical fitting curve according to eq. (3.2). The black dash-dotted and solid lines are, respectively, the fitting curves according to eqs. (3.3) and (3.4).

Still the evolution is peculiar (S-shaped) with enhanced emission at low temperature.

The bell-shaped dependence observed for sample A only at high power is probably a spurious effect. While the high temperature region can be still described by a thermally activated process, the reduced emission at low temperature is probably related to a non-radiative process like Auger mechanism. Being a multi-particle mechanism, this is effective at high excitation intensity (with overlapping excited pairs) and essentially evident at low temperature (when the carrier mobility is lower). In fact, the Auger mechanism has been invoked also to explain the reduced PL intensity at low temperature in case of amorphous silicon under high excitation intensity [35]. At low intensity the non-radiative multiparticle process is ruled out, but, instead of a constant low temperature PL emission, an enhancement is found, and globally an S-shaped behaviour appears. A tentative rough description of the data can be accomplished by considering two thermally activated non-radiative channels with different activation energies (E_a and E_e):

$$I(T) = I_0/[1 + \beta_a \exp(-E_a/k_B T) + \beta_e \exp(-E_e/k_B T)] \quad (3.3)$$

where the proportionality constants β_a and β_e reflect the probability of the two events. The black dash dotted line is the model curve applied to our case. The several free parameters and the indetermination on I_0 allow only a rough evaluation. In particular the steep intensity drop at low temperature asks for a low energy barrier (E_e ~ 3 meV), while the high temperature evolution is described with a much larger barrier (E_a ~ 140 meV), with $\beta_e << \beta_a$ ~ 1500. As for the high temperature data, the parameter values are consistent with literature data. The observed increase of both E_a and β_a with Si excess going from sample C to A agrees with previous findings [11]. The model can be refined to reproduce the S-shaped dependence by including an extra term in the denominator of (3.3) due to electron capture into trap states followed by thermal emission [40]:

$$I(T) = I_0/\left\{1 + \beta_a \exp\left(-\frac{E_a}{k_B T}\right) + \beta_e \exp\left(-\frac{E_e}{k_B T}\right) + c_1\left[1 + c_2 \exp\left(-\frac{E_{Trap}}{k_B T}\right)\right]\right\} \quad (3.4)$$

where c_1 and c_2 are some constants somewhat describing this extra process. The black solid line, that reproduces rather well the experimental evolution, is obtained with such improved model adopting a trap energy level E_{Trap} ~ 180 meV.

This uncommon S-shaped dependence has been reported for CdS nanoclusters [40]: in that case the extracted low and high activation barriers were supposed to be related to the processes of capture of electrons at surface states and thermal escape from the nanoclusters respectively. In presence of quasi-Si domains, also in our case a mechanism of capture at interface states (with barrier E_e ~ 3 meV) could take place, while at larger temperature the ionization to the mobility edge dominates (with E_a ~ 140 meV). With lower Si excess and

then likely fewer Si rich domains (sample C) only the classic single activation process is instead evidenced.

CHAPTER 4

Properties of annealed SiN_X thin films

In the previous chapter we have investigated the possibility of producing Si nanoparticles in silicon nitride thin films directly via PECVD by choosing appropriate deposition regimes. We have found that the material indeed cannot be described in terms of a pure random bonding model, however only partial phase separation was observed. Due to the undubious advantages at the implementation stage within multilayered devices, the search for different deposition regimes allowing for in-situ formation of Si nanoparticles is still under way in several laboratories including ENEA, also considering a different material for the matrix [1]. At the same time we have followed a slightly more conventional route that required a post-deposition annealing step. The thermal treatment is used to induce a precipitation transformation where the metastable Si-rich dielectric film decomposes into two stable phases: Si clusters and a matrix, which is closer in composition to the equilibrium (stoichiometric) composition. This technique still guarantees full CMOS compatibility with microelectronics processing and possible implementation in *c*-Si based PV devices. Since we start with a partially phase separated material we have explored the possibility of inducing complete phase separation by applying thermal treatments that were shorter and milder than the typically reported in the literature [2, 3]. With this purpose a series of annealing treatments at increasing temperatures (500 - 1050°C) and decreasing times (≤ 10 minutes) has been applied on our PEDCV-grown Si-rich samples with a rapid thermal

annealing furnace. A more conventional final annealing step at 1100°C for 1 hour has been also performed.

In this chapter the annealing effects on various properties of films with different Si content is reported. The evolution of Raman, FTIR, photoluminescence, and optical absorption spectra has been investigated. The partial phase separation, with silicon-rich and nitrogen-rich regions, evidenced in the as-grown material, is emphasized by the thermal treatments that induce further reorganization of the two phases. Crystallization of silicon aggregates has been detected only after the highest temperature treatments (1100°C), with both temperature and time probably playing a crucial role. The presence of Si nanoparticles in this case has been confirmed by EFTEM analysis. Among the various characterization techniques we have concentrated our attention on an extensive Raman analysis, pointing out its significant potentialities when investigating Si nanoparticles as opposed to destructive and time consuming TEM.

4.1 Sample fabrication

Si rich samples have been deposited by PECVD using the deposition parameters reported in the previous chapter. Again, quartz and *c*-Si substrates, that can stand high temperature treatments, have been used. Short annealing treatments have been applied using a rapid thermal annealing furnace in nitrogen flow. The annealing temperature (T_a) has been increased in the range 500 – 1050°C, and correspondingly, shorter times have been set. In particular the applied treatments are: (500°C for 30 min), (600°C for 10 min), (700°C for 10 min), (800°C for 5 min) and (1050°C for 3 min). The highest temperature has been applied again two more times consecutively for a total of 7 min, reaching 10 min in the overall at 1050°C.

Only as a final step, a conventional treatment at 1100°C for 1 hour has been performed. This treatments has been carried out in nitrogen atmosphere in a quartz tube furnace.

Samples with different stoichiometry have been considered by growing the films with different SiH_4/N_2 flow rate ratios. From RBS analysis the Si excess with respect to the stoichiometric composition goes from 11% up to about 45%. Most of the results reported in this chapter, however will be related to two samples with mild Si excess, 18% and 11%, named A and B respectively (with the warning that these are not the same A and B samples as in chapter 3), essentially because these have been already published.

4.2 Structural and morphological properties vs annealing: FTIR, Raman spectroscopy, EFTEM

The evolution of the bonding structure has been analyzed by Fourier transform infrared spectroscopy (FTIR), in the range 400 – 4000 cm^{-1} (fig. 4.1).

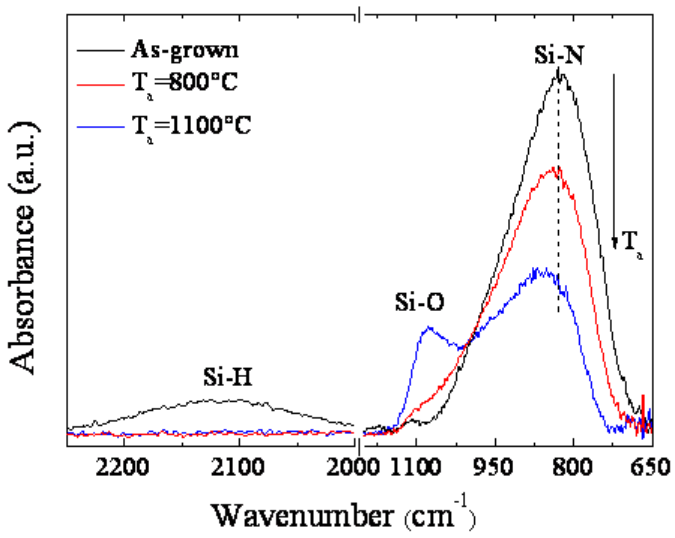

Figure 4. 1 - IR absorbance of a sample in as-grown condition and after annealing.

Mainly two absorption bands are present: the Si-N asymmetric stretching mode around 825 cm^{-1} and the Si-H stretching mode at 2100 cm^{-1}. Besides the flattening of the hydrogen related mode after the annealing step at 800°C, the Si-N mode shifts from ~ 825 to ~ 850 cm^{-1}, indicating an increased number of nitrogen atoms bonded to the same Si, with increasing annealing temperature. These are signatures respectively of dehydrogenation and bond rearrangement. The Si-N peak shift, already reported in [4, 5] indicates that the number of nitrogen atoms bonded to a silicon one is increasing (for example, a $N_2Si–SiN$ bond is replaced by a $N_3–SiN$ one). There is then an enrichment of nitrogen atoms in the silicon nitride phase approximating it to Si_3N_4 as T_a increases. At the same time the film stoichiometry remains the same with T_a. The only possibility to explain the shift is that the enrichment of the silicon nitride phase in nitrogen is occurring with a parallel appearance of a pure silicon phase (not detectable in infrared absorption measurements). The sub-stoichiometric nitride phases in the as-deposited films change then toward a biphasic Si/Si_3N_4 mixture. This phase separation process has been evidenced also in SiO_x films, in that case through a similar of the Si–O stretching band toward higher wave numbers [6].

It should be noted that after the last annealing step a shoulder between 1000 and 1100 cm^{-1} is also visible. This absorption band can be ascribed to the Si–O stretching mode and is likely due to a non-intentional oxidation of the sample surface. This hypothesis is confirmed by RBS spectroscopy and TEM, that indicate the presence of some superficial oxide after the last annealing step.

The structural evolution with annealing treatments appears also from the micro-Raman analysis. The Raman spectra of as-grown and annealed sample A, after the subtraction of the substrate contribution, are shown in fig. 4.2.

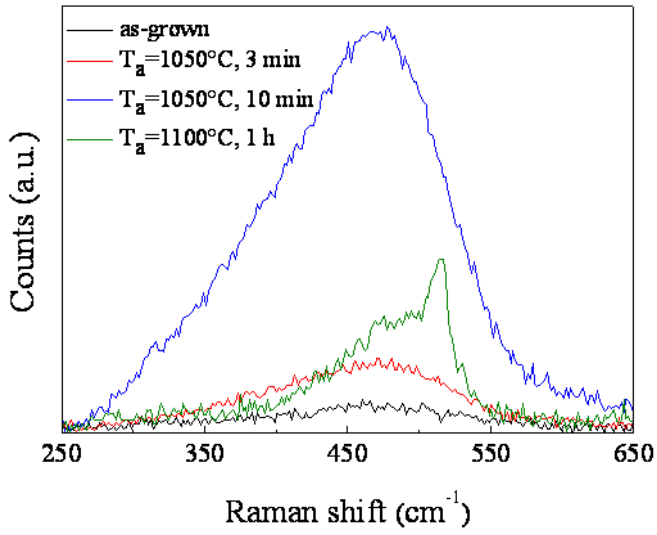

Figure 4. 2 - Raman spectra of sample A (18% of Si excess) in as-grown condition and after selected thermal treatments

A weak signature of the presence of Si-Si bonds (wide peak around 470 cm^{-1}) is present in the spectrum of the as-grown material. As shown in the previous chapter this peak can be described as convolution of Si-N and *a*-Si modes, thus indicating some partial phase separation in the material. The thermal treatments gradually enhance the Raman signal (the huge increase observed after 10minutes at 1050°C will be discussed in section 4.4) while not influencing the shape of the curve. The spectrum is strongly modified only after the annealing at 1100°C with a sharp peak appearing at ~ 512 cm^{-1}. The enhanced Raman signal after the thermal treatments (up to 1050°C) can be read as a modification occurring within the material with an increase of Si-Si bonds, both after dehydrogenation (reduction of Si-H bonds) and rearrangement of Si-N bonds. The narrow sharp peak appearing at ~ 512 cm^{-1}, after the annealing at 1100°C, is a clear indication that, inside the material, crystallization of small silicon regions has occurred. Due to phonon confinement, the position of the Raman peak strongly depends on the size of the nanocrystals, approaching 520 cm^{-1} (position of the TO mode in bulk crystalline Si) when the size of the crystal cluster grows up. From the Raman line shift it is possible to estimate the average nanocrystal size. The quickest way is to recur to the relation between

the Raman shift $\Delta\omega$ (taking as reference position the *c*-Si peak at 520 cm^{-1}) and the nanocrystal size *L* derived in ref. 7 (bond polarizability model):

$$\Delta\omega = -A(a/L)^{\gamma} \qquad (4.1)$$

Here *a* is the Si lattice constant (0.543 nm), while *A* and γ are fitting parameters describing the phonon confinement, that in the case of nanometric spheres are equal to 47.41 cm^{-1} and 1.44, respectively. So for sample A the average nanocrystal size is 1.9 nm for $\Delta\omega$ = (520 – 512) cm^{-1} = 8 cm^{-1}. It should be noted that the spectrum shows also a peak around 480 cm^{-1}. Then amorphous Si aggregates should be also present in the material.

The aggregation of Si nanoclusters after the final annealing step is confirmed by EFTEM. In fig. 4.3 the light spots of samples A and B are reported. The diffraction patterns (insets in fig. 4.3) clearly indicate the crystalline nature of the clusters in sample A (Si excess = 18%), while only some hints of the rings are present in the other case (Si excess = 11%), where however the aggregates are very small.

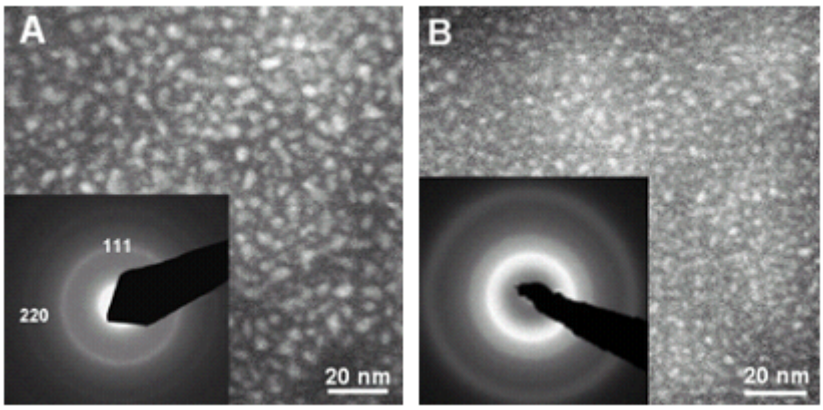

Figure 4. 3 - EFTEM plan view images and electron diffraction patterns of samples A and B annealed at 1100°C.

As for the intermediate annealing steps, no pure nanoparticles are detected by TEM until the treatment at 1050°C. In fig. 4.4, we report a cross-sectional

EFTEM image of the sample with Si excess ~ 20% annealed at 1050°C for 10 min. The image and the electron diffraction pattern, shown as inset, confirm the aggregation of amorphous Si-QDs. This is an important result, because prove the possibility to obtain *a*-Si-QDs after a short thermal annealing, even if rather high temperature is still required.

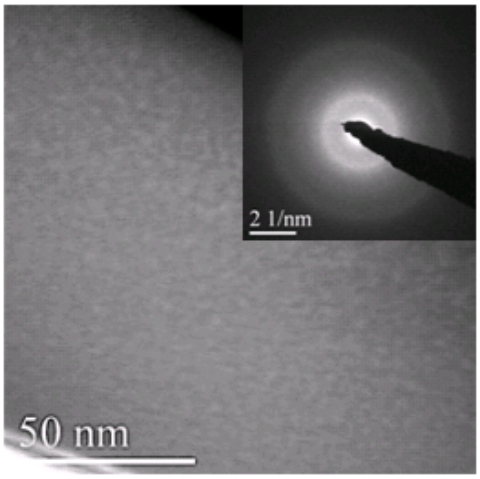

Figure 4. 4 – EFTEM cross-section image and electron diffraction pattern of an annealed sample at 1050°C.

4.3 PL and optical absorption coefficient vs. annealing treatments

In this paragraph the effect of the annealing treatments on optical properties is reported [8, 9]. Data for the A and B previously defined samples, is shown.
The two as-grown samples show room temperature photoluminescence peaked at 1.85 eV and 2 eV, for the films A and B respectively (fig. 4.5).

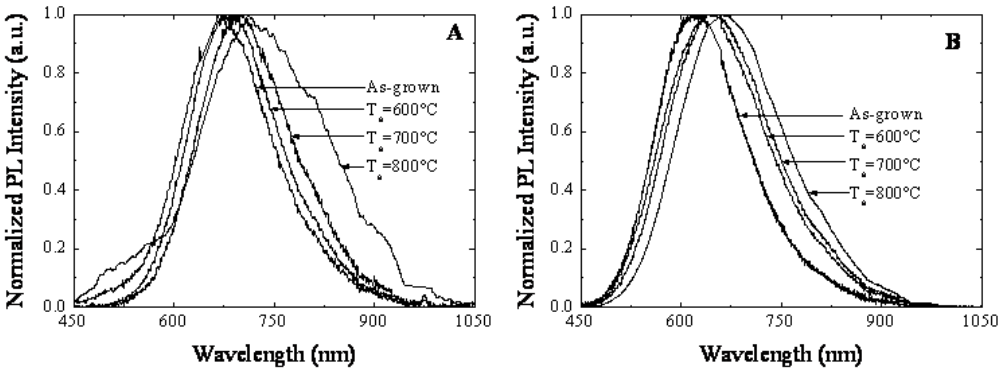

Figure 4. 5 - Normalized PL spectra of as-grown and annealed samples A and B under excitation at 325 nm.

The evolution of the normalized PL intensity with T_a is shown in fig. 4.5. In both cases a redshift with the increase of the annealing temperature up to 800°C is observed, while above 800°C the PL is quenched.

The PL redshift with increasing T_a in the quantum confinement model would be explained in terms of a thermally induced nanoparticle enlargement. However, the dominating PL mechanism in our samples, as shown in chapter 3, seems to be the tail to tail radiative recombination. In this model, the PL redshift following the thermal treatments (fig. 4.5) could be related to a thermally induced change in the energy gap. But, essentially, after high temperature annealing the PL intensity is strongly reduced. We believe that this is due to the formation of a large number of non-radiative recombination channels (large number of dangling bonds after the break of Si-H and N-H bonds in the process of hydrogen desorption).

In fig. 4.6 the absorption spectra of the two samples in the as-grown and annealed conditions are shown. In both cases, as T_a is raised (up to 1050°C), the spectra shift toward lower energy, meanwhile developing pronounced tails, and the films become increasingly more absorbent essentially due to hydrogen release and rearrangement of Si-Si and Si-N bonds [4]. After the treatment at 1100°C an inversion is observed in the medium energy range (thick line in fig. 4.6 (a) and (b)), which is a signal of a different structural change making the material less absorbent. In particular this is a consequence of the formation of

Si nanocrystals evidenced through Raman and TEM analysis in the previous paragraph, since *c*-Si has lower absorption coefficient than *a*-Si in this range.

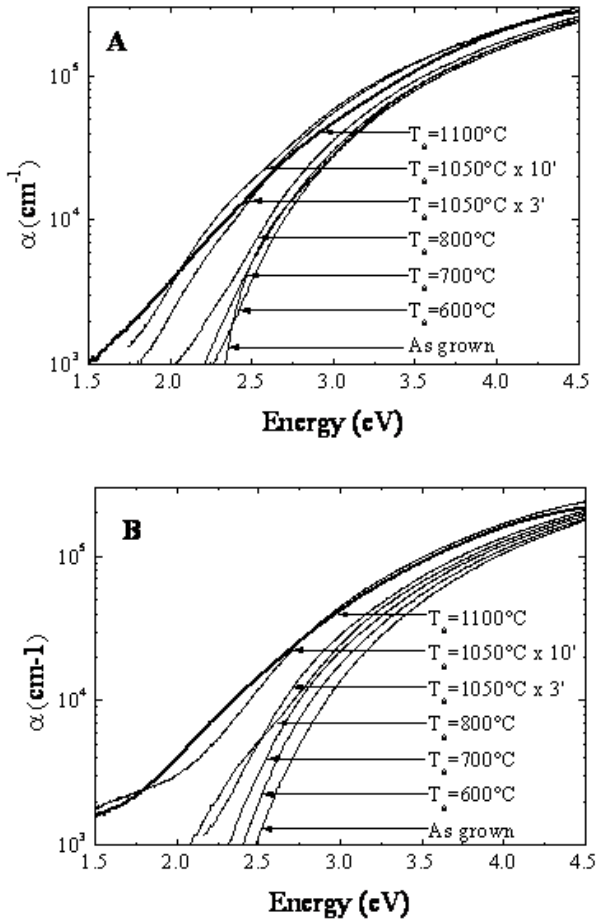

Figure 4. 6 – Optical absorption spectra of as-grown and annealed samples A and B.

Applying the Tauc formula [10, 11] (eq. 3.1 in chapter 3), the gap energies, E_g, have been evaluated after each annealing step and the plot of E_g vs T_a is shown in figure 4.7. As already mentioned, the general trend is that E_g decreases with increasing T_a.

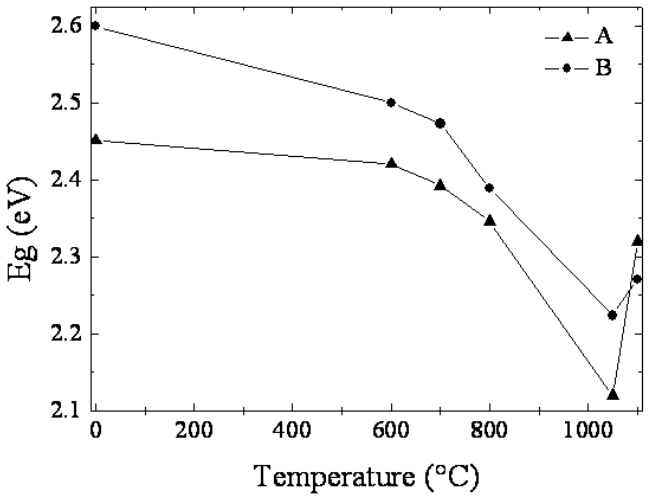

Figure 4. 7 - Gap energy (E_g) plotted as a function of annealing temperature (T_a).

In both cases first a slower and then a faster decrease of E_g with increasing T_a up to 1050°C is observed, likely signalling two different mechanisms influencing the variation in the absorption properties, such as hydrogen release below 600 - 700°C and Si and N atoms diffusion, with rearrangement of Si-Si and Si-N bonds, above it. This interpretation is consistent with the FTIR results and other literature data [4] on evaporated SiN_x, where absence of hydrogen in the films treated above 800°C is reported. A sudden increase of E_g is afterwards found following the final annealing step (1100°C), but this is only an artefact, because of the inappropriateness of the Tauc procedure to evaluate E_g in presence of a crystalline phase.

4.4 Extensive micro-Raman analysis

Confinement effects in reduced dimension systems lead to major modifications of electronic, optical and vibrational properties. All of these contain information about many parameters that are essential to understand the physics of the materials, in view of designing new generation devices. Among the

various characterization techniques, Raman spectroscopy is an excellent nondestructive optical tool to study the change in the vibrational properties. More flexible and straightforward than transmission electron microscopy (TEM), Raman spectroscopy can provide direct evidence of nucleation of Si nanocrystals (Si-ncs) and quantitative information regarding mean size and in principle size distribution. For this reason first-order Raman spectra of nanocrystalline silicon have been studied extensively [7, 12 - 16]. On the other hand very few reports of higher-order modes can be found because of their usually weak intensity.

In this section we report on first and second-order Raman analysis on silicon nitride films embedding Si nanoparticles to show the potentialities of this characterization technique [17]. Structural information, compatible with the fundamental description derived by time-consuming and destructive TEM, are obtained and indication of a possible enhancement of the electron-phonon interaction strength both in amorphous and crystalline Si nanoparticles is inferred.

4.4.1 Theoretical background

In bulk crystalline material, the Raman technique samples only optical phonons close to the Brillouin Zone (BZ) centre. This selection rule is essentially a consequence of the translational symmetry in crystals that implies conservation of momentum, so, for scattering photons in the visible range (with wave vector about three orders of magnitude smaller than the BZ edge), only phonons with very small momentum are active. For silicon these modes have frequency of 520 cm^{-1} and the Raman spectrum of *c*-Si is characterized by a narrow peak at this position (red curve in fig. 4.8 (a)). In Si-ncs, where the periodicity of the crystal is interrupted, the limitation of the translational symmetry leads to relaxation of the momentum selection rule. Following the uncertainty principle, phonons from a region around the BZ center, determined by the size of the

nanocrystal, contribute to the scattering. This causes a line broadening. Moreover, due to the decrease in the frequency of optical phonons when moving away from the BZ center, the Raman line is shifted to lower energies. This peak shift and broadening is a direct signature from nanocrystals. Several models were developed to explain these modifications upon confinement and possibly derive an expression allowing to extract the nanocrystal size from the spectra. The most commonly used are: (i) the model of Richter et al. [12], Campbell and Fauchet [13] and (ii) the bond-polarizability (BP) model of Zi et al. [7] (already used in section 4.2). The former, using a phenomenological confinement function, allows to calculate the lineshape of the Raman peak as a function of the Si-ncs size. In the latter, following a microscopic approach, a relation between the Raman shift $\Delta\omega$ and the nanocrystal size L is derived [eq. (4.1) in Sec. 4.2]. This relation allows to quickly determine the average nanocrystal diameter, but is appropriate only for very small particles and does not include a possible size dispersion. On the other hand within the phenomenological approach (i), with appropriate choice of the confinement function, significant Raman analysis can be performed that applies also in presence of non-negligible size dispersion [15, 16, 18]. In this model the first order Raman spectrum of spherical Si nanocrystals with mean diameter L_0, size dispersion σ, and size distribution described by $\Phi(L, \sigma)$, can be written as [15, 18]:

$$I(\omega, L_0, \sigma) \propto \int dL \Phi(L, \sigma) \int_{BZ} \frac{|C(q,L)|^2 d^3q}{[\omega - \omega(q)]^2 + (\Gamma_0/2)^2} \qquad (4.2)$$

where $C(q,L)$ is the Fourier coefficient of the phenomenologically chosen phonon confinement function, $\omega(q)$ the phonon-dispersion relation (the analytic form $\omega(q) = \omega_0(1 - 0.20q^2)$ is typically used) and Γ_0 the linewidth of the bulk *c*-Si peak. A Gaussian confinement function, that usually provides good agreement with experiments [13, 15, 18], and a normal size distribution function, that allows to incorporate the dispersion analytically into the Raman

intensity profile expression, have been here selected. In this case the Raman intensity is given by [15]:

$$I(\omega, L_0, \sigma) \propto \int_0^1 \frac{dq\, q^2 f(q) exp[-q^2 f^2(q) L_0^2/2\beta]}{[\omega - \omega(q)]^2 + (\Gamma_0/2)^2} \left\{1 + erf\left[\frac{L_0 f(q)}{\sqrt{2}\sigma}\right]\right\} \quad (4.3)$$

where $f(q) = [1 + (q\,\sigma)^2/\beta]^{-1/2}$, L_0 and q are in units of lattice constant a and wavevector $2\pi/a$ respectively, and β is the localization parameter, that for strong localization is equal to 2. To apply the model to our case the *c*-Si peak position (ω_0 = 520 cm^{-1}) and linewidth (Γ_0 = 5 cm^{-1}) have been extracted from measurements performed on bulk *c*-Si with the same instrumental set-up in order to account for the experimental spectral resolution.

In case of monodispersed particles (σ = 0), the model well reproduces the characteristic peak shift and asymmetric broadening of the Raman spectra of Si nanocrystals when their size decreases, as shown by the simulation in fig 4.8 (a) with diameters in the range 2 – 10 nm.

Figure 4.8 (b) shows, instead, the effect of σ on the Raman line shape. Here the calculated Raman profiles from an ensemble of Si nanocrystallites having a mean crystallite diameter of 3.5 nm and variable dispersion are plotted. The introduction of a dispersion shifts the peak only slightly, but considerably increases the bandwidth, enhancing the asymmetry of the curve (the increase in FWHM is almost entirely due to the increase in the low frequency tail, while the line-shape at the high frequency side remains practically unchanged).

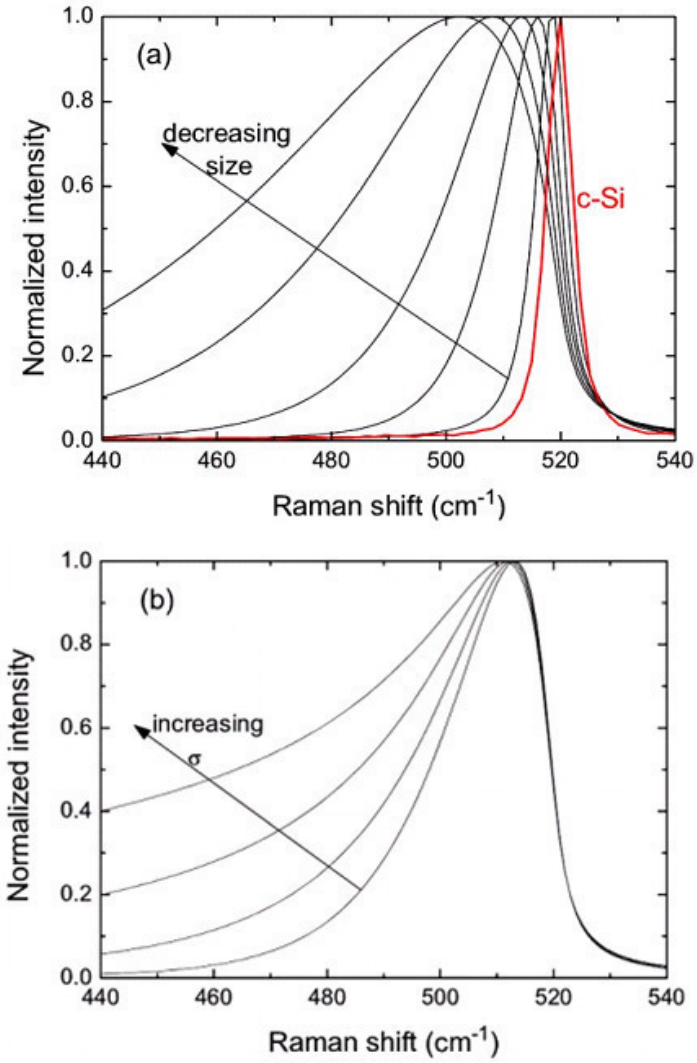

Figure 4. 8 - Simulated Raman profiles for ensembles of Si nanocrystals: **(a)** with decreasing size from 10 to 2 nm and σ = 0, and **(b)** with fixed mean size (3.5 nm) but different size dispersion (0 - 40%). In (a) also the TO mode for *c*-Si is reported for reference (red curve).

4.4.2 Comparison of first-order Raman spectra and TEM results

The first-order Raman spectra of samples A and B annealed at 1100°C are reported in fig. 4.9 (a) and (b). A clear peak at 512 cm^{-1} is found for sample A while for sample B only a weak shoulder around 508 cm^{-1} is detected. The statistical analysis of the particle size distribution obtained from the EFTEM

micrographs is also reported as histogram (insets in fig. 4.9 (a) and (b)). Both the films show rather large size dispersion, as expected since no attempt was made at containing the cluster size. The average size in the two films however scales with the Si excess.

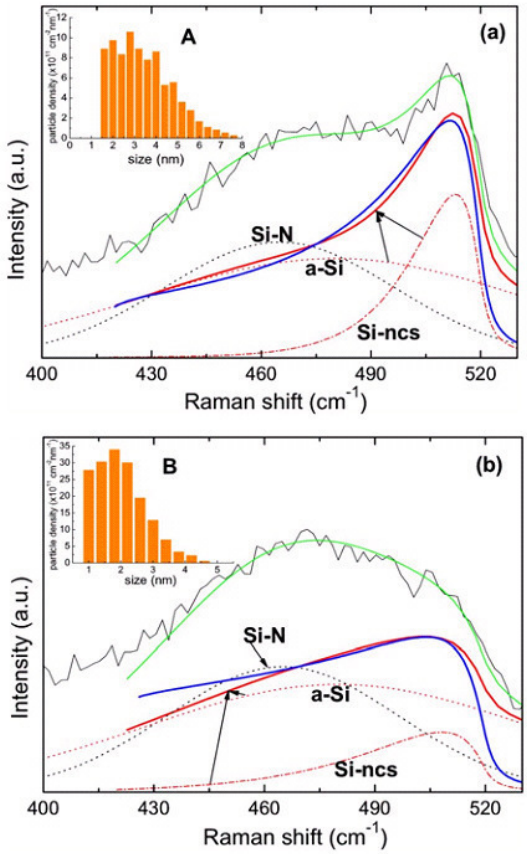

Figure 4. 9 - First-order Raman spectra of sample A **(a)** and B **(b)** after annealing at 1100°C with the respective size dispersion histograms deduced from EFTEM as **insets**. The green line is the theoretical curve obtained as convolution of the Si-N and *a*-Si Gaussian bands (black and red dotted lines respectively), and the asymmetrically broadened peak from Si-ncs in the $\sigma = 0$ approximation (red dash-dotted line). The blue curve is the calculated Raman spectrum for Si-ncs in presence of size dispersion and the solid red line is the sum of the peaks of *a*-Si and Si-ncs with $\sigma = 0$.

When applying the BP model [7], with our measured shifts, sizes of 1.9 nm and 1.4 nm are calculated for sample A and B respectively. Only for sample B the result is not far from the average dimension evaluated from EFTEM analysis. The application of the Gaussian phonon confinement model [15] is shown in

fig. 4.9. The difficulty with this material is that there is contribution from Si-N (expected around 465 cm^{-1}, as found in the as-grown case) and possibly *a*-Si modes, both very close to the Si-ncs peak. As a first attempt the contribution of Si-ncs to the first-order Raman spectrum has been evaluated with eq. (4.2) in the monodisperse approximation ($\sigma = 0$). The line-shape for both the samples can be reproduced as a convolution of three contributions: two Gaussian bands centred at 465 cm^{-1} and 480 cm^{-1} (dotted lines in the figure 4.9), assigned to Si-N and *a*-Si respectively, and the asymmetrically broadened peak from Si-ncs (dash-dotted line) with diameter 3.5 nm and 2.5 nm for sample A and B respectively, rather close to the average size estimated through TEM. It should be noted that, using exactly the same Gaussian contributions from *a*-Si and Si-N for the two films and different contributions only for the Si-ncs, the agreement between model and experiment is satisfactorily good. From the integrated intensities of the Si-ncs and *a*-Si peaks (I_c and I_a respectively) the crystalline volume fraction $\rho_c = I_c / (I_c + y\, I_a)$ can be estimated, where y is the ratio of the integrated Raman cross-section for Si-ncs to *a*-Si, that was shown to approach 1 for small nanocrystals [14]. The estimated ρ_c values are only 25% and 16% for sample A and B respectively. However, the effect of the size distribution (neglected for the moment) is to enhance the asymmetry of the Raman peak for Si-ncs on the low wavenumber side (fig. 4.8 (b)), where the *a*-Si peak is located. Therefore, in the present approximation, a probably unreal large contribution from *a*-Si is deduced. A better estimate should be extracted when including the size dispersion. The blue thick lines in fig. 4.9 have been obtained using eq. (4.2), with the same mean sizes as before and $\sigma = 35\%$ for sample A and 50% for sample B. Such σ values are consistent with the size distribution obtained from EFTEM (where an even larger dispersion is observed). Besides the tail on the high wave-number side, the curves are almost coincident with the thick red lines in fig. 4.3 obtained by adding up the peak from *a*-Si and from Si-ncs with $\sigma = 0$. Thus the contribution from *a*-Si could be very well accounted for by the increased asymmetry of the Si-ncs peak in presence of large σ. In this extreme case, complete crystallization would be deduced.

Summarizing, with eq. (4.3), even without including the size dispersion, reasonable values of the average diameter can be deduced. Such values are only slightly overestimated with respect to the fundamental data from TEM, while the BP model underestimates the sizes with larger discrepancy the bigger the nanocrystals. Some indetermination is however left about the crystalline phase fraction, since the extracted value strongly depends on σ. As for samples A and B in particular, even if the large σ used to generate the blue curves in fig. 4.9 is consistent with the wide size distribution obtained from TEM, at least in sample B, where a much larger value has been used to cancel out the *a*-Si contribution, the amorphous fraction is likely non negligible, as suggested also by the diffraction pattern (fig. 4.3).

4.4.3 Intensity evolution of Raman spectra with annealing

The Raman spectra for as grown and annealed sample A in an extended wavenumber range is reported in fig. 4.10. When looking at the intensity, it is interesting to note that after the annealing step for 10 min at 1050°C the spectrum is strongly enhanced (as anticipate in sec. 4.2) as for a resonance. This effect has been observed for several Si-rich samples.

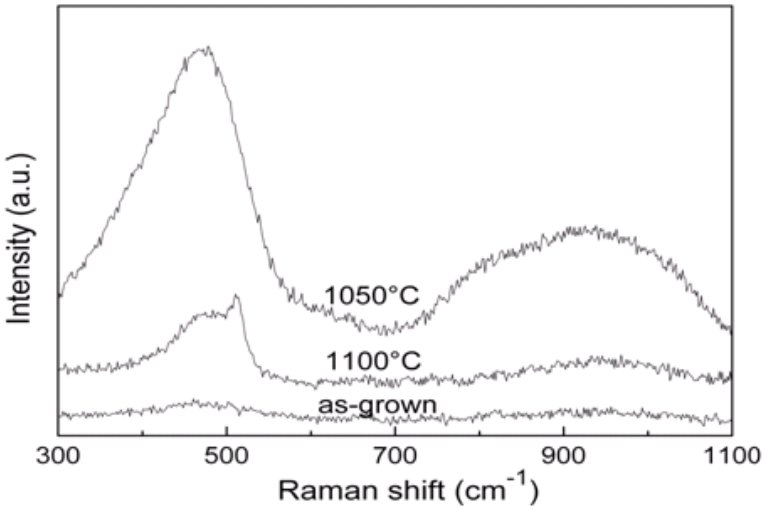

Figure 4. 10 – Raman spectra of as-grown and annealed sample A shown with an arbitrary offset after subtraction of the baseline.

Supposing a realistic thermally-induced formation of *a*-Si nanoparticles [19], a possible interpretation is that the probing laser energy matches the enlarged nanoparticle band gap [20, 21]. Tentative diameters of the *a*-Si dots would then be around 1.7 nm, according to Ref. 22. With the following annealing step at 1100°C an enlargement and crystallization of the aggregates is induced, likely moving the material away from the resonance condition. However, when considering the estimated nanocrystal sizes and their potential band gaps [3], also in this case the samples should not be far from resonance.

The proposed resonance condition has been tested by acquiring the Raman spectra also at different excitation wavelength. In fig. 4.11, we illustrate a schematic of the experiment with laser light of 514 and 633 nm.

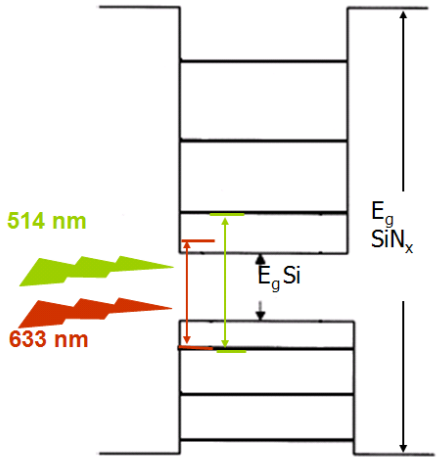

Figure 4. 11 - Schematic illustration of the matching condition of the green light (514 nm) with the enlarged Si nanoparticle band-gap and non-matched condition with the red light (633 nm).

The Raman spectra for the sample with 30% silicon excess (C) at 633 nm is reported in fig. 4.12. In this case the intensities of the spectra for the sample annealed at 1050 and 1100°C are comparable indicating that at 633 nm we are out of resonance.

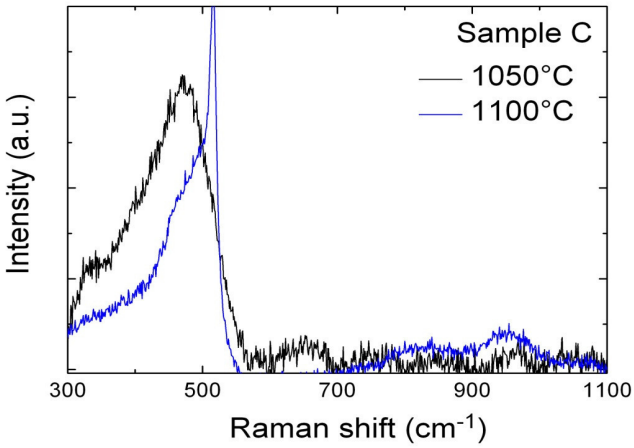

Figure 4. 12 – Raman spectra of annealed sample C at 633 nm.

The hypothesis of formation of *a*-Si-QDs has been indeed confirmed by EFTEM (fig. 4.4), and the average radius is 1.3 nm as reported in fig. 4.13 (a). This average size is a bit larger than the value that could be estimated from literature data (fig. 4.13 (b)).

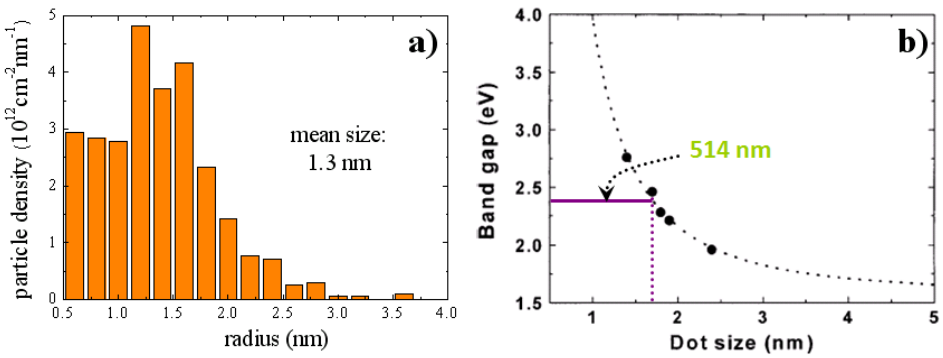

Figure 4. 13 – (a) Size dispersion histogram from EFTEM for sample C annealed at 1050°C; **(b)** Relation between band-gap and dot size found by Park et al. [22].

4.4.4 Second-order Raman spectra

Valuable information can be extracted also from the second order spectra, usually not much investigated because of the strongly reduced intensity. Shift

and broadening is expected also for the 2TO mode (the 2TO(W) and 2TO(L) modes of *c*-Si are located at 940 cm^{-1} and 975 cm^{-1} respectively [23]). However in case of *a*-SiN_x this can be difficult to study because of the contribution from the Si-N mode around 850 cm^{-1} that is IR and Raman active [24].

A very wide and intense band in the range 750 - 1100 cm^{-1} is observed (fig. 4.14).

Enhanced 2TO mode was reported also in ref. 25 regarding alike samples. The band can be deconvoluted in two contributions (blue lines): (i) the Si-N mode centred at 830 cm^{-1} after annealing at 1050°C and at 860 cm^{-1} after annealing at 1100°C (following the trend observed with the IR measurements), and (ii) a mode around 960 - 965 cm^{-1}, that can be assigned to silicon. After subtraction of the Si-N contribution from both first and second order spectra, still the intensity of the overtone peak is substantially enhanced with respect to the *a*-Si and *c*-Si cases.

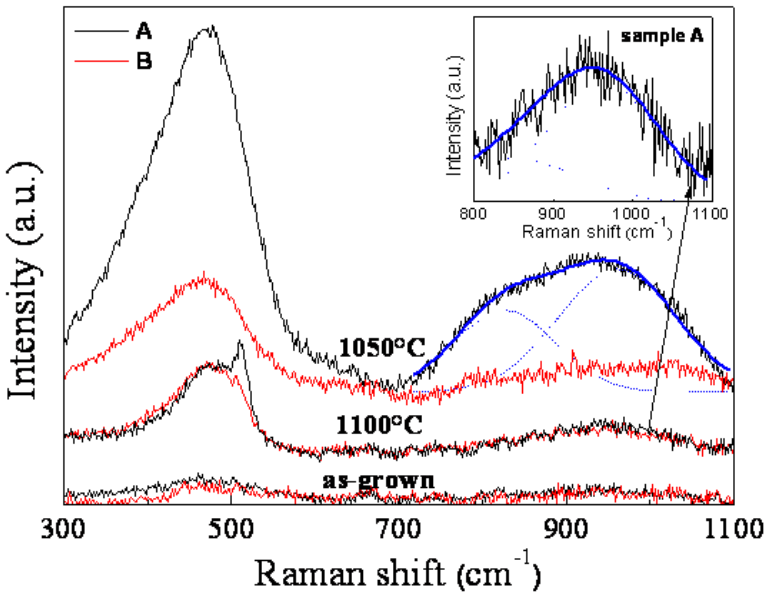

Figure 4. 14 - Raman spectra of as-grown and annealed sample A shown with an arbitrary offset after subtraction of the baseline. The blue line shows the analysis of the 2TO mode. **Zoom**: deconvolution of the second-order spectrum of sample A annealed at 1100°C.

For sample A annealed at 1050°C (likely in resonant condition, as discussed previously) the integrated intensity ratio $\eta = I(2TO)/I(TO)$ is 1.3 against 0.25 for *a*-Si. The η ratio is similarly increased (~ 0.9) also in the spectra measured for both the samples after annealing at 1100°C that, though not exactly resonant, should also be close to resonance when considering the estimated cluster size. In resonant Raman scattering experiments, in principle the electron-phonon interaction can be directly probed through the two-phonon to one-phonon scattering cross section ratio η [21]. Size dependent enhanced strength of the electron–phonon coupling is therefore suggested for both amorphous and crystalline Si nanoparticles in analogy with similar results on CdS_xSe_{1-x} nanocrystals [21]. With the electron–phonon interaction influencing at various extent physical attributes like transport, light emission, linear, and nonlinear optical properties, this is a relevant result in application prospect.

CONCLUSIONS

This work concerns the realization and characterization of silicon nitride thin films embedding Si nanoparticles. Such material class is receiving a great deal of attention for the possible application in new-generation optoelectronic devices, both in photonics, for the prospects of monolithic integration of photonic layer and electronic substrate (all Si-based), and in photovoltaics (PV) to boost the efficiency of solar cells.

The objectives of this thesis are: 1) to investigate convenient fabrication procedures in view of a straightforward application of the material in multilayered devices (among which, in particular, the so-called all-silicon tandem solar cells), 2) to improve upon the characterization techniques regarding this material class, and, more in prospect, 3) to possibly provide a proof of concept study of quantum confinement to support the implementation of new-generation optoelectronic devices.

Regarding the fabrication stage, two different approaches have been followed: a simpler in-situ route and a procedure involving a post-deposition annealing step. First of all the possibility of producing Si nanoparticles in silicon nitride thin films in-situ has been explored, because of the undubious advantage of possible use of low cost substrates and straightforward implementation within multilayered devices. Amorphous hydrogenated silicon nitride films have been grown by PECVD at 300°C, using two different gas mixtures [a) silane and nitrogen and b) silane and ammonia diluted in nitrogen]. Series of samples with different stoichiometry have been realized, intentionally adopting a low growth rate regime, which, according to literature, would favour a non homogeneous material growth. All the samples show room temperature photoluminescence (PL) in the visible range, with a systematic shift and intensity evolution of the PL spectra with gradual changes in the stoichiometry of the films.

Firstly, following the literature, this PL behavior has been ascribed to size and density change of silicon quantum dots spontaneously formed in the silicon

nitride matrix thanks to the selected growth process. When searching for evidence of phase separation within the material, however, EFTEM analysis does not show presence of Si nanoparticles. Only hints of a partial separation, with Si rich regions in SiN_x matrix, are deduced through Raman spectroscopy. Based on this structural/morphological data, we have concluded that the band-tail states model is more appropriate to explain the PL mechanism. In this case the luminescence is ascribed to radiative recombination of carriers that thermalize in the conduction and valence band tails, and the PL peak blue-shifts because of the enlargement of the bandgap when the concentration of alloying N atoms is raised. However, when exciting the material with below-gap light, peculiar PL spectra have been observed, likely because band gap fluctuations due to the compositional dishomogeneity come into play and PL from Si-rich domains is induced. In particular, we have found that both PL intensity and emission energy from the quasi-Si regions are increased with respect to amorphous Si, thanks to the spatial localization of the excited carriers. The peculiar PL spectra measured with below-gap excitation can be therefore regarded as another proof of the partial phase separation within the material.

By following the in-situ fabrication path, then, we have succeeded at realizing only partially separated material. Meanwhile we have also explored the possibility of inducing complete phase separation by applying short mild thermal treatments. A series of subsequent annealing treatments has been performed at increasing temperatures in the range 500 - 1100°C on Si-rich samples with different stoichiometry. In particular, short (≤ 10 minutes) post-deposition annealing treatments up to 1050°C have been applied using a rapid thermal annealing furnace in nitrogen flow. A more conventional final annealing step (1100°C for 1 hour) in nitrogen atmosphere in a quartz tube furnace has been also performed. The evolution of Raman spectra, room temperature photoluminescence, and optical absorption of the samples has been investigated, searching for evidence of thermally induced effects, such as phase separation and nanoparticle crystallization within the material.

Through FTIR analysis, hydrogen desorption and bond rearrangement have been observed, with the organization of a silicon phase (not directly detectable in infrared absorption measurements) in a matrix evolving toward stoichiometric ratio. Dehydrogenation and rearrangement of bonds explain the evolution of the absorption coefficient spectra with the annealing treatments (decreasing bandgap and gradually more absorbent material). Interestingly, an inversion in this systematic evolution of the optical absorption curves has been observed in the medium energy range (~ 2.3 - 4 eV) after the final step at 1100°C. This is a signal of crystallization occurring within the material, as crystalline Si is less absorbent than amorphous Si in this energy range. Aggregation of Si nanocrytals after the final annealing step has been indeed confirmed by EFTEM, with average particle size scaling with the Si content in the starting material. Formation of amorphous Si nanoparticles (not easy to identify through the analysis of the evolution of the absorption coefficient spectra) has been instead revealed by EFTEM after the previous rapid (10 minutes) annealing step at 1050°C. Therefore, rather high annealing temperatures seem to be necessary to induce complete phase separation. However rapid treatments might be already appropriate to produce at least amorphous Si nanoparticles.

As for our goal of providing a proof of concept study of quantum confinement, we have observed a strong quenching of the photoluminescence with the annealing steps above 800°C, probably due to the creation of a large amount of non-radiative defects, not passivated by hydrogen anymore after the material dehydrogenation. In this condition it has not been possible to study quantum confinement effects through PL.

In view of improving upon the characterization techniques, we have focused particularly on Raman spectroscopy and proved its significant potentialities when investigating nanostructured Si and in particular Si nanoparticles embedded in silicon nitride (where fundamental and overtone spectra are influenced by Si-N vibrational modes). Studying the first-order spectra in presence of Si nanocrystals, we have shown that with a model description (a Gaussian phonon confinement model including normal size distribution) it is

possible to access information regarding mean radius (quantitatively), size dispersion, and crystalline phase fraction (indicatively) consistent with the fundamental data derived from time-consuming and destructive TEM. Moreover, a resonance phenomenon has been observed for samples with amorphous Si nanoparticles and a strongly enhanced two-phonon band has been detected in several cases (after annealing at 1050°C and 1100°C). We have been able to conclude that the occurrence of a resonance can be one way to establish the presence of amorphous Si nanoparticles with appropriate size within the material, and that precious information on the physics at the nanoscale (the electron-phonon coupling in this case) can be extracted from second-order spectra.

In conclusion, by applying post deposition annealing treatments we have succeeded at fabricating silicon nitride thin films with Si nanoparticles (both amorphous and crystalline). Rather high temperatures were necessary, but the procedure still guarantees full CMOS compatibility with microelectronics processing and possible implementation in c-Si based PV devices. The characterization analysis has provided 1) some insight into the correlation between structural and optical properties and 2) an improvement upon the characterization techniques of low-dimensional silicon also through non-destructive and faster techniques than TEM. Of course, further research is still needed if the successful implementation of these material systems into a device is to be achieved.

References

Chapter 1

[1] S. Tiwari, F. Rana, K. Chan, H. Hanafi, W. Chan, and D. Buchanan, "Volatile and non-volatile memories in silicon with nano-crystal storage", IEDM, 521(1995).

[2] L. Guo, E. Leobandung, S. Y. Chou, "A Silicon Single-Electron Transistor Memory Operating at Room Temperature", Science 275, (1997) 649.

[3] T. Gebel, L. Rebohle, J. Zhao, D. Borchert, H. Fröb, J. V. Borany, and W. Skorupa, "Ion beam synthesis based formation of Ge-rich thermally grown SiO_2 layers: a promising approach for a silicon based light emitter", Mat. Res. Soc. Symp. Proc. 638, (2001) F 18.1.

[4] J. Kirby, "Nobel lectures, Physics 1996-2000", edited by Ekspong G. (World Scientific Publishig Co. Singapore), 474 (2002).

[5] K. Yano, T. Ishii, T. Sano, T. Mine, F. Murai, T. Hashimoto, T. Kobayashi, T. Kure, and K. Seki, "Single-electron memory for giga-to-tera bit storage", Proc. IEEE 87, (1999) 633.

[6] P. Cappelletti, C. Golla, P. Olivo and E. Zanoni, "Flash Memories", (Kluwer Academic Publishers) (1998).

[7] International Technology Roadmap for Semiconductors (ITRS), 2002 Edition, Process Integration, Devices, and Structures and Emerging Research Devices.

[8] W. Wade and D. Lammers, EE Times, July 16 (2001).

[9] K. Yoshikawa, "Technology Requirements for Next Decade Flash Memories", in Proceedings of the 30th European Solid-State Device

Research Conference, Cork Ireland, 11-13, September 2000 (Frontier Group, ESSDERC) 72 (2000).

[10] B. De Salvo, S. Lombardo, Proceedings of the Workshop "Non volatile memories with discrete storage nodes", Special issue of Solid-State Electronics, 48 (2004).

[11] L. C. Kimerling, "Silicon microphotonics", Appl. Surf. Sci. 159-160, (2000) 8-13.

[12] D. Kovalev, H. Heckler, M. Ben-Chorin, M. Schwartzkopff, and F. Koch, "Breakdown of the k-Conservation Rule in Si nanocrystals", Phys. Rev. Lett. 81, (1998) 2803.

[13] S. S. Jyer and Y.-H. Xie, "Light Emission from Silicon", Science 260, (1993) 40.

[14] L. T. Canham, Mater. Res. Bull. 18, 22 (1993).

[15] L. T. Canham, "Silicon quantum wire array fabrication by electrochemical and chemical dissolution of wafers", Appl. Phys. Lett. 57, (1990) 1046.

[16] L. T. Canham, Phys. World 5, 41 (1992).

[17] A. G. Cullis, L. T. Canham, and P. G. J. Calcott, "The structural and luminescence properties of porous silicon", J. Appl. Phys. 82, (1997) 909.

[18] T. Shimizu-Iwayama, K. Fujita, S. Nakao, K. Saitoh, T. Fujita, and N. Itoh, "Visible photoluminescence in Si^{+}-implanted silica glass", J. Appl. Phys. 75, (1994) 7779.

[19] J. G. Zhu, C. W. White, J. D. Budai, S. P. Withrow, and Y. Chen, "Growth of Ge, Si, and SiGe nanocrystals in SiO_2 matrices", J. Appl. Phys. 78, (1995) 4386.

[20] K. S. Min, K. V. Shcheglov, C. M. Yang, H. A. Atwater, M. L. Brongersma, and A. Polman, "Defect-related versus excitonic visible light emission from ion beam synthesized Si nanocrystals in SiO_2", Appl. Phys. Lett. 69, (1996) 2033.

[21] E. Werwa, A. A. Seraphin, L. A. Chin, Chuxin Zhou, and K. D. Kolenbrander, "Synthesis and processing of silicon nanocrystallites

using a pulsed laser ablation supersonic expansion method", Appl. Phys. Lett. 64, (1994) 1821.

[22] L. N. Dinh, L. L. Chase, M. Balooch, L. J. Terminello, and F. Wooten, "Photoluminescence of oxidized silicon nanoclusters deposited on the basal plane of graphite", Appl. Phys. Lett. 65, (1994) 3111.

[23] H. Morisaki, F. W. Ping, H. Ono, and K. Yazawa, "Above-band-gap photoluminescence from Si fine particles with oxide shell", J. Appl. Phys. 70, (1991) 1869.

[24] S. Hayashi, T. Nagareda, Y. Kanzawa, and K. Yamamoto, "Photoluminescence of Si-Rich SiO_2 Films: Si Clusters as Luminescent Centers", Jpn. J. Appl. Phys. Part 1 32, (1993) 3840.

[25] Y. Kanzawa, T. Kageyama, S. Takeoka, M. Fujii, S. Hayashi, and K. Yamamoto, "Size-dependent near-infrared photoluminescence spectra of Si nanocrystals embedded in SiO_2 matrices", Solid State Commun. 102, (1997) 533.

[26] Z. H. Lu, D. J. Lockwood, and J.-M. Baribeau, "Quantum confinement and light emission in SiO2/Si superlattices", Nature (London) 378, (1995) 258.

[27] D. J. Lockwood, Z. H. Lu, and J.-M. Baribeau, "Quantum Confined Luminescence in Si/SiO_2 Superlattices", Phys. Rev. Lett. 76, (1996) 539.

[28] G. Conibeer, M. A. Green, R. Corkish, Y. Cho, E-C. Cho, C-W Jiang, T. Fangsuwannarak, E. Pink, Y. Huang, T. Puzzer, "Silicon nanostructures for third generation photovoltaic solar cells", Thin Solid Film, 511-512, (2006) 654.

[29] F. Iacona, G. Franzò, and C. Spinella, "Correlation between luminescence and structural properties of Si nanocrystals", J. Appl. Phys. 87, (2000) 1295.

[30] D. M. Chapin, C. S. Fuller, and G. L. Pearson, "A new silicon p-n junction photocell for converting solar radiation into electrical power", J. Appl. Phys. 25, (1954) 676.

[31] M. A. Green, "Third generation photovoltaics advanced solar energy conversion", Springer series in photonics, Netherlands (2003)

[32] Martin A. Green, "Third Generation Photovoltaics: Ultra-high Conversion Efficiency at Low Cost", Prog. Photovolt: Res. Appl. 9, (2001) 123-135.

[33] E. C. Cho, Y.H. Cho, T. Trupke, R. Corkish, G. Conibeer, and M. A. Green, " Silicon nanostructures for all-Silicon tandem solar cells", the 19th European Photovoltaic Solar Energy Conference and Exhibition, Paris (2004)

[34] Y.H. Cho, M. A. Green, E. C. Cho, Y. Huang, T. Trupke, and G. Conibeer, "Silicon quantum dots in nitride matrix for third generation photovoltaics", the 20th European Photovoltaic Solar Energy Conference and Exhibition, Barcelona (2005).

[35] M. A. Green, E-C. Cho, Y. Cho, Y. Huang, E. Pink, T. Trupke, A. Lin, T. Fangsuwannarak, T. Puzzer, G. Conibeer, and R. Corkish, "Artificial Semiconductor Synthesised Using Si Quantum Dots in a Dielectric Matrix", the 20th European Photovoltaic Solar Energy Conference and Exhibition, Barcelona (2005).

[36] T. Fangsuwannarak, E.C. Cho, G. Conibeer, Y. Huang, T. Trupke and M.A. Green, "Analysis of the effect of silicon quantum dot density on the photoluminescence spectra of silicon dot/silicon dioxide superlattices", Proc. 21th European Photovoltaic Solar Energy Conf. Dresden, Germany, (2006).

[37] W. Shockley and H. J. Queisser, "Detailed balance limit of efficiency of p-n junction solar cells", J. Appl. Phys. 32, (1961) 510-519.

[38] M. A. Green, K. Emery, Y. Hishikawa, and W. Warta, "Solar cell efficiency tables (version 36)", Progress in photovoltaics: research and applications 18, (2010) 346-352.

[39] M. A. Green, "Third Generation Photovoltaics: Advanced Solar Energy Conversion", Springer, Berlin, Germany (2003)

[40] M. A. Green, G. Conibeer, D. König, E. C. Cho, Y. Cho, T. Fangsuwannarak, Y. Huang, G. Scardera, E. Pink, S. Huang, C. Jiang, T. Trupke, R. Corkish, and T. Puzzer, "Progress with all-silicon tandem cells based on silicon quantum dots in a dielectric matrix", in Proceedings of the 21st European Photovoltaic Solar Energy Conference, Dresden, Germany, June 2006.

Chapter 2

[1] P. Y. Yu and M. Cardona, "Fundamentals of Semiconductors-physics and Materials properties", third ed. Berlin: Springer-Verlag, 2005.

[2] B. D. Yacobi, "Semiconductor Materials-An Introduction to Basic Principles", New York: Kluwer Academic /Plenum Publishers, 2003.

[3] O. Manasreh, "Semiconductor Heterojunctions and Nanostructures", New York: McGraw Hill, 2005.

[4] J. A. Wang, U. A. Griesinger, F. Adler, H. Schweizer, V. Harle, and F. Scholz, "Size effect upon emission dynamics of 1.5 μm quasi-quantum wire distributed feedback semiconductor lasers", Applied Physics Letters, vol. 69, (1996) 287-289.

[5] R. Heitz, O. Stier, I. Mukhametzhanov, A. Madhukar, and D. Bimberg, "Quantum size effect in self-organized InAs/GaAs quantum dots", Physical Review B, vol. 62, (2000) 11017-11028.

[6] M. V. Maximov, A. F. Tsatsul'nikov, B. V. Volovik, D. A. Bedarev, Y. M. Shernyakov, I. N. Kaiander, E. Y. Kondrat'eva, A. E. Zhukov, A. R. Kovsh, N. A. Maleev, S. S. Mikhrin, V. M. Ustinov, Y. G. Musikhin, P. S. Kop'ev, Z. I. Alferov, R. Heitz, N. N. Ledentsov, and D., "GaAs-based lasers emitting at similar to 1.3 μm", Microelectronic Engineering, vol. 51-2, (2000) 61-72.

[7] T. Winzell, I. Maximov, L. Landin, Y. Zhang, A. Gustafsson, L. Samuelson, and H. J. Whitlow, "Bandgap modification in GaInAs/InP

quantum well structures using switched ion channelling lithography" Semiconductor Science and Technology, vol. 16, (2001) 889-894.

[8] C. Jagadish, G. Li, M. B. Johnston, and M. Gal, "Si and C delta-doping of GaAs grown by metal organic vapour phase epitaxy for fabrication of nipi doping superlattices", Materials Science and Engineering B - Solid State Materials for Advanced Technology, vol. 51, (1998) 103-105.

[9] R. B. Hammond and R. N. Silver, "Temperature dependence of the exciton lifetime in high-purity silicon", Appl. Phys. 36, (1980) 68.

[10] M. A. Tamor and J.P. Wolfe, "Drift and Diffusion of Free Excitons in Si", Phys. Rev. Lett. 44, (1980) 1703.

[11] R. N. Hall, "Electron-Hole Recombination in Germanium", Phys. Rev. 87, (1952) 387.

[12] W. Schockley and W.T. Read, "Statistics of the Recombinations of Holes and Electrons", Phys. Rev. 87, (1952) 835.

[13] J. D. Cuthbert, "Recombination Kinetics of Excitonic Molecules and Free Excitons in Intrinsic Silicon", Phys. Rev. B 1, (1970) 1552.

[14] S. Coffa, G. Franzò, F. Priolo, A. Pacelli, and A. Lacaita, "Direct evidence of impact excitation and spatial profiling of excited Er in light emitting Si diodes", Appl. Phys. Lett., 73, (1998) 93.

[15] M. V. Wolkin, J. Jorne, P. M. Fauchet,G. Allan, and C. Delerue, "Electronic States and Luminescence in Porous Silicon Quantum Dots: The Role of Oxygen", Phys. Rev. Lett. 82, (1999) 197.

[16] C. Delerue, G. Allan, and M. Lannoo, "Theoretical aspects of the luminescence of porous silicon", Phys. Rev. B 48, (1993) 11024.

[17] C. Delerue, G. Allan, and M. Lannoo, "Optical band gap of Si nanoclusters", J. Lumin. 80 (1999) 65-73.

[18] M. A. Green, E.-C. Cho, Y.-H. Cho, E. Pink, T. Trupke, K.-L. Lin, T. Fangsuwannarak, T. Puzzer, G. Conibeer, and R. Corkish, "All-silicon tandem solar cells based on "artificial" semiconductor synthesized using quantum dots in a dielectric matrix", in Proceedings

of the 20th European Photovoltaic Solar Energy Conference and Exhibition, p. 3, Barcelona, Spain, June 2005.

[19] F. Iacona, G. Franzò, and C. Spinella, "Correlation between luminescence and structural properties of Si nanocrystals", J. Appl. Phys. 87, (2000) 1295.

[20] M. Zacharias, J. Heitmann, R. Scholz, U. Kahler, M. Schmidt, J. Blasing, "Size-controlled highly luminescent silicon nanocrystals: A SiO/SiO_2 superlattice approach", Appl. Phys. Lett. 80, (2002) 661-3.

[21] N-M Park, T-S Kim, and S-J Park, "Band gap engineering of amorphous silicon quantum dots for light emitting diodes", Appl. Phys. Lett. 78, (2001) 2575-7.

[22] N-M Park, C-J Choi, T-Y Seong, and S-J Park, "Quantum Confinement in Amorphous Silicon Quantum Dots Embedded in Silicon Nitride", Phys. Rev. Lett. 86, (2001) 1355-7.

[23] Y. Q. Wang, Y. G. Wang, L. Cao, and Z. X. Cao, "High-efficiency visible photoluminescence from amorphous silicon nanoparticles embedded in silicon nitride", Appl. Phys. Lett. 83, (2003) 3474-6.

[24] M. Molinari, H. Rinnet, and M. Vergnat, "Visible photoluminescence in amorphous SiN_x thin films prepared by reactive evaporation", Appl. Phys. Lett. 77, (2000) 3499-3501.

[25] M. Molinari, H. Rinnet, and M. Vergnat, "Evolution with the annealing treatments of the photoluminescence mechanisms in a-SiN_x:H alloys prepared by reactive evaporation", J. Appl. Phys. 101, (2007) 123532.

[26] M-S Yang, K-S Cho, J-H Jhe, S-Y Seo, J.H. Shin, K.J. Kim, and D.W. Moon, "Effect of nitride passivation on the visible photoluminescence from Si-nanocrystals", Appl. Phys. Lett. 85, (2004) 3408-10.

[27] Y. Cho, E.-C. Cho, Y. Huang, T. Trupke, G. Conibeer, and M. A. Green, "Silicon quantum dots in SiN_x matrix for third generation

photovoltaics", in Proceedings of the 20th European Photovoltaic Solar Energy Conference and Exhibition, p. 47, Barcelona, Spain, June 2005.

[28] L-Y Chen, W-H Chen, and F. C-N Hong, "Visible electroluminescence from silicon nanocrystals embedded in amorphous silicon nitride matrix", Appl. Phys. Lett. 86, (2005) 193506.

[29] L. Dal Negro, J.H. Yi, L. C. Kimerling, S. Hamel, A. Williamson, and G. Galli, "Light emission from silicon-rich nitride nanostructures", Appl. Phys. Lett. 88, (2006) 183103.

[30] T-Y Kim, N-M Park, K-H Kim, G. Y. Sung, Y-W Ok, T-Y Seong, and C-J Choi, "Quantum confinement effect of silicon nanocrystals in situ grown in silicon nitride films", Appl. Phys. Lett. 85, (2004) 5355-7.

[31] T-W Kim, C-H Cho, B-H Kim, and S-J Park, "Quantum confinement effect in crystalline silicon quantum dots in silicon nitride grown suing SiH_4 and NH_3", Appl. Phys. Lett. 88, (2006) 123102.

[32] J. I. Pankove, "Optical Processes in Semiconductors", Dover Publications Inc., New York, 1971, p. 34.

[33] H. T. Grahn, "Introduction to Semiconductor Physics", World Scietific Publishing, Singapore, 2001, p.130.

[34] S. Mirabella, R. Agosta, G. Franzò, I. Crupi, M. Miritello, R. Lo Savio, M. A. Di Stefano, S. Di Marco, F. Simone, and A. Terrasi, "Light absorption in silicon quantum dots embedded in silica" J. Appl. Phys. 106, (2009) 103505.

[35] F. Giorgis, C. Vinegoni, and L. Pavesi, "Optical absorption and photoluminescence properties of a-$Si_{1-x}N_x$:H films deposited by plasma-enhanced CVD", Phys. Rev. B. 61, (2000) 4693-4698.

[36] ROUESSAC F. and ROUESSAC A., "Analyse chimique, méthodes et techniques instrumentales moderns", 5ème edition. Paris: Dunod, 2000.

[37] DALIBART M. and SERVANT L., "Spectroscopie dans l'infrarouge". In Techniques de l'Ingénieur, Dossier: P2845, vol. TA4 [en ligne]. Editions T.I. Sciences et Techniques, 2000, 26p.

[38] W. S. Lau, "Infrared Characterization for Microelectronics", World Scientific Publishing, Singapore (1999), Chapter 1.

[39] D. V. Tsu, G. Lucovsky, M. J. Mantini, "Local atomic structure in thin films of silicon nitride and silicon diimide produced by remote plasma-enhanced chemical vapour deposition", Phys. Rev. B. 33, (1986) 7069-76.

[40] G. Scardera, T. Puzzer, I. Perez-Wurfl, G. Conibeer, "The effects of annealing temperature on the photoluminescence from silicon nitride multilayer structures", Journal of Crystal Growth 310, (2008) 3680–3684.

[41] F. Giorgis, F. Giuliani, C. F. Pirri, E. Tresso, C. Summonte, R. Rizzoli, R. Galloni, A. Desalvo, and P. Rava, "Optical, structural and electrical properties of device-quality hydrogenated amorphous silicon-nitrogen films deposited by plasma-enhanced chemical vapour deposition", Phil. Mag. B. 77, (1998) 925-944.

[42] C. V. Raman and K. S. Krishnan, "A New Type of Secondary Radiation", Nature 121/3048 (1928) 501.

[43] Z. Iqbal, S. Veprek, A. P. Webb, and P. Capezzuto, " Raman scattering from small particle size polycrystalline silicon", Solid State Commun. 37, (1981) 993.

[44] G.-X. Cheng, H. Xia, K.-J. Chen, W. Zhang, and X.-K. Zhang, "Raman measurement of the grain size for silicon crystallites", Phys. Status Solidi A 118, (1990) K51.

[45] H. Kakinuma, M. Mohri, M. Sacamoto, and T. Tsuruoka, "Structural properties of polycrystalline silicon films prepared at low temperature by plasma chemical vapor deposition", J. Appl. Phys. 70, (1991) 7374.

[46] Wei Cheng, Shang-Fen Ren, "Calculations on the size effects of Raman intensities of silicon quantum dots", Phys. Rev. B, 65, (2002) 205305.

[47] Jian Zi, Kaiming Zhang, Xide Xie, "Comparison of models for Raman spectra of Si nanocrystals", Phys. Rev. B, 55, (1997) 9263.

[48] P. Parayanthal, Fred H. Pollak, "Raman Scattering in Alloy Semiconductors: "Spatial Correlation" Model", Phys. Rev. Lett., 52, (1984) 1822.

[49] V. Paillard, P. Puech, M. A. Laguna, R. Carles, B. Kohn, and F. Huisken, "Improved one-phonon confinement model for an accurate size determination of silicon nanocrystals", J. Appl. Phys., 86, (1999) 1921.

[50] Hua Xia, Y. L. He, L. C. Wang, W. Zhang, X. N. Liu, X. K. Zhang, D. Feng, and Howard E. Jackson, "Phonon mode study of Si nanocrystals using micro-Raman spectroscopy", J. Appl. Phys., 78, (1995) 6705.

[51] V. A. Volodin, M, D. Efremov, V. A. Gritsenko, S. A. Kochubei, "Raman study of silicon nanocrystals formed in SiNNx films by excimer laser or thermal annealing", Appl. Phys. Lett. 73, No. 9, (1998), 1212.

[52] Renishaw Raman imaging microscope, WIRE^{TM} (Windows-based Raman environment) user guide, M/8012/1798//02.

[53] V. E. Cosslet, "Introduction to electron optics", Oxford University Press, London (1946).

[54] J. C. H. Spence, "High-Resolution Electron Microscopy", Oxford University Press, third edition, (2003).

Chapter 3

[1] G. Conibeer, M. Green, R. Corkish, Y. Cho, E.-C. Cho, C.-W. Jiang, T. Fangsuwannarak, E. Pink, Y. Huang, T. Puzzer, T. Trupke, B. Richards, A. Shalav, K.-L. Lin "Silicon nanostructures for third generation photovoltaic solar cells", Thin Solid Films 511-512 (2006) 654-662.

[2] M. Zacharias, J. Heitmann, R. Scholz, U. Kahler, M. Schmidt and J. Bläsing, "Size-controlled highly luminescent silicon nanocrystals: A SiO/SiO_2 superlattice approach", Appl. Phys. Lett. 80 (2002) 661.

[3] Nae-Man Park, Chel-Jong Choi, Tae-Yeon Seong, and Seong-JuPark, "Quantum Confinement in Amorphous Silicon Quantum Dots Embedded in Silicon Nitride" Phys. Rev. Lett. 86, No. 7 (2001) 1355-1357.

[4] Tae-Wook Kim, Chang-Hee Cho, Baek-Hyun Kim, and Seong-Ju Park, "Quantum confinement effect in crystalline silicon quantum dots in silicon nitride grown using SiH_4 and NH_3", Appl. Phys. Lett. 88 (2006) 123102.

[5] Nae-Man Park, Sang Hyeob Kim, Yong Sung, and Seong-Ju Park, "Growth and size control of amorphous silicon quantum dots using SiH_4/N_2 plasma", Chem. Vap. Deposition 8, No. 6 (2002), pp. 254-256.

[6] L. V. Mercaldo, P. Delli Veneri, E. M. Esposito, I. Usatii, C. Privato, "Low temperature PECVD in-situ growth of silicon quantum dots in silicon nitride for third generation photovoltaics", Proceedings of the 23rd European Photovoltaic Solar Energy Conference (2008) 629-632.

[7] Lucia V. Mercaldo, Paola Delli Veneri, Emilia Esposito, Ettore Massera, Iurie Usatii, and Carlo Privato, "PECVD in-situ growth of silicon quantum dots in silicon nitride from silane and nitrose", Materials Science and Engineering B 159–160 (2009) 77–79.

[8] Lucia V. Mercaldo, Paola Delli Veneri, Emilia Esposito, Ettore Massera, Iurie Usatii, and Carlo Privato, "Structural and optical properties of silicon quantum dots in silicon nitride grown in situ by PECVD using different gas precursors", Materials Science and Engineering B 159–160 (2009) 74–76.

[9] E. Dehan, P. Temple-Boyer, R. Henda, J. J. Pedroviejo, E. Scheid, "Optical and structural properties of SiO_x and SiN_x materials", Thin Solid Films 266 (1995) 14.

[10] J. Robertson, "Defect and impurity states in silicon nitride", J. Appl. Phys. 54 (8), (1983), 4490.

[11] S. V. Deshpande, E. Gulari, S. W. Brown and S. C. Rand, "Optical properties of silicon nitride films deposited by hot filament chemical vapour deposition", J. Appl. Phys. 77 (1995) 6534.

[12] F. Boulitrop, D. J. Dunstan, "Phonon interactions in the tail states of a-Si:H", Phys. Rev. B 28 (1983) 5923.

[13] D. J. Dunstan, F. Boulitrop, "Photoluminescence in hydrogenated amorphous silicon", Phys. Rev. B 30 (1984) 5945.

[14] F. Giorgis, P. Mandracci, L. Dal Negro, C. Mazzoleni, L. Pavesi, "Optical absorption and luminescence properties of wide-bandgap amorphous silicon based alloys", Journal of Non-Crystalline Solids 266-269 (2000) 588-592.

[15] Nae-Man Park, Tae-Soo Kim,and Seong-Ju Park, "Bandgap engineering of amorphous silicon quantum dots for light-emitting diodes", Appl. Phys. Lett. 78, (2001) 2575.

[16] J. F. Lelievre, H. Rodriguez, J. De La Torre, A. Kaminski, E. Fourmond, S. Quizola, A. Sibai, G. Bremond, M. Lemiti, D. Araujo, C. Monat, P. Ribeyron, Y. Pellegrin, "Formation of silicon nanostructures embedded in SiN_x:H films by different deposition techniques: application to silicon solar cells", Proc. 21st European PV Solar Energy Conf., Dresden (2006), p. 1456-1459.

[17] G. Lucovsky, J. Yang, S. S. Chao, J. E. Tyler, and W. Czubatyj, "Nitrogen-bonding environments in glow-discharge-deposited a-Si:H films", Phys. Rev. B 28, (1983) 3234.

[18] S. Hasegawa, H. Anbutsu, Y. Kurata, "Connection between Si-N and Si-H vibrational properties in amorphous SiN_x:H films", Phil. Mag. B, Vol.59, No. 3, (1989) 365-375.

[19] G. Lucovsky, "Chemical effects on the frequencies of Si-H vibrations in amorphous solids", Solid State Commun. 29, (1979) 571.

[20] K. C. Lin, S. C. Lee, "The structural and optical properties of a-SiN_x:H prepared by plasma-enhanced chemical vapour deposition", J. Appl. Phys. 72 (11), (1992) 5474.

[21] M. L. Brongersma, P. G. Kik, A. Polman, K. S. Min, Harry A. Atwater, "Size-dependent electron-hole exchange interaction in Si-nanocrystals", Appl. Phys. Lett., 76, (2000) 351.

[22] M. Molinari, H. Rinnert, M. Vergnat, "Evolution with the annealing treatments of the photoluminescence mechanisms in a-SiN_x:H alloys prepared by reactive evaporation", J. Appl. Phys. 101, (2007) 123532.

[23] X.-W. Du, M. Takeguchi, M. Tanaka, K. Furuya, "Formation of crystalline Si nanodots in SiO_2 films by electron irradiation", Appl. Phys. Lett. 82 (2003) 1108.

[24] E. D. Palik, Handbook of Optical Constants of Solids, vol. I, 1985.

[25] Z. Yin, F.W. Smith, "Tetrahedron model for the optical dielectric function of hydrogenated amorphous silicon nitride alloys", Phys. Rev. B 42 (1990) 3658.

[26] J. Tauc, in Optical properties of solids, ed. By F. Abeles, North Holland, Amsterdam, 1970.

[27] A. R. Zanatta, I. Chambouleyron, "Absorption edge, band-tails, and disorder of amorphous semiconductors", Phys. Rev. B 53, (1996) 3833.

[28] J. Robertson, "Defects and hydrogen in amorphous silicon nitride", Philos. Mag. B 69, (1994) 307.

[29] I. Sakata, Y. Hayashi, and H. Karasawa, "A new characterization parameter for hydrogenated amorphous silicon: B (the square of the gradient of the $(\alpha\hbar\omega)^{1/2}$ versus $\hbar\omega$ plot)", J. Appl. Phys. 52, (1981) 4334.

[30] J. Bullot and M. P. Schmidt, "Physics of amorphous Silicon-Carbon alloys", Phys. Status Solidi B 143, (1987) 345.

[31] L. V. Mercaldo, E. M. Esposito, P. Delli Veneri, B. Rezgui, A. Sibai, G. Bremond, "Photoluminescence properties of partially phase separated silicon nitride films", submitted to Appl. Phys. Lett..

[32] F. Giorgis, C. Vinegoni, L. Pavesi, "Optical absorption and photoluminescence properties of a-$Si_{1-x}N_x$:H films deposited by plasma-enhanced CVD" Phys. Rev. B 61, (2000) 4693.

[33] I. G. Austin, W. A. Jackson, T. M. Searle, P. K. Bhat, R. A. Gibson, "Photoluminescence properties of a-SiN_x:H alloys", Phil. Mag. B 52, (1985) 271.

[34] K. Nishio, J. Koga, T. Yamaguchi, F. Yonezawa, "Light emission properties of amorphous silicon quantum dots", J. Non-Cryst. Solids 312–314, (2002) 323–326.

[35] R. A. Street, "Luminescence and recombination in hydrogenated amorphous silicon", Adv. Phys. 30, (1981) 593.

[36] L. Dal Negro, J. H. Yi, J. Michel, L. C. Kimerling, T.-W. F. Chang, V. Sukhovatkin, E. H. Sargent, "Light emission efficiency and dynamics in silicon-rich silicon nitride films", Appl. Phys. Lett. 88, (2006) 233109.

[37] H. Rinnert, O. Jambois, M. Vergnat, "Photoluminescence properties of size-controlled silicon nanocrystals at low temperatures", J. Appl. Phys. 106, (2009) 023501.

[38] A. Irrera, F. Iacona, I. Crupi, C. D Presti, G. Franzò, C. Bongiorno, D. Sanfilippo, G. Di Stefano, A. Piana, P. G. Fallica, A. Canino and F. Priolo, "Electroluminescence and transport properties in amorphous silicon nanostructures", Nanotechnology 17, (2006) 1428–1436.

[39] A. G. Cullis, L. T. Canham, and P. D. J. Calcott, "The structural and luminescence properties of porous silicon", J. Appl. Phys. 82, (1997) 909.

[40] E. A. Bagaev, K. S. Zhuravlev, L. L. Sveshnikova, "Temperature dependence of photoluminescence from CdS nanoclusters formed in the matrix of Langmuir-Blodgett film", Phys. Stat. Sol C 3, (2006) 3951.

Chapter 4

[1] U. Coscia, G. Ambrosone, D. K. Basa, S. Ferrero, P. Delli Veneri, L. V. Mercaldo, I. Usatii, and M. Tucci, "Characterizations of nanostructured silicon-carbon films deposited on p-layer by PECVD", Phys. Status Solidi C 7, No. 3–4, (2010) 766– 769.

[2] M. Zacharias, J. Heitmann, R. Scholz, U. Kahler, M. Schmidt and J. Bläsing, "Size-controlled highly luminescent silicon nanocrystals: A SiO/SiO_2 superlattice approach", Appl. Phys. Lett. 80 (2002) 661.

[3] G. Conibeer, M. Green, E.-C. Cho, D. König, Y.-H. Cho, T. Fangsuwannarak, G. Scardera, E. Pink, Y. Huang, T. Puzzer, S. Huang, D. Song, C. Flynn, S. Park, X. Hao, and D. Mansfield, "Silicon quantum dot nanostructures for tandem photovoltaic cells", Thin Solid Films 516, (2008) 6748 - 6756.

[4] M. Molinari, H. Rinnert, M. Vergnat, "Evolution with the annealing treatments of the photoluminescence mechanisms in a-SiN_x:H alloys prepared by reactive evaporation", J. Appl. Phys. 101, (2007) 123532.

[5] G. Scardera, T. Puzzer, G. Conibeer, M. A. Green, "Fourier transform infrared spectroscopy of annealed silicon-rich silicon nitride thin films", J. Appl. Phys. 104, (2008) 104310.

[6] F. Iacona, G. Franzò, C. Spinella, "Correlation between luminescence and structural properties of Si nanocrystals", J. Appl. Phys. 87, (2000) 1295.

[7] J. Zi, H. Buscher, C. Falter, W. Ludwig, K. Zhang, X. Xie, "Raman shifts in Si nanocrystals", Appl. Phys. Lett. 69 (1996) 200.

[8] L. V. Mercaldo, E. M. Esposito, P. Delli Veneri, L. Lancellotti, C. Privato, "Investigation of thermally induced phase separation in PECVD-grown silicon nitride", Proceedings of the 24th European Photovoltaic Solar Energy Conference (2009).

[9] E. M. Esposito, L. V. Mercaldo, P. Delli Veneri, L. Lancellotti, C. Privato, "Annealing effects on PECVD-grown Si-rich a-SiN_x thin films", Energy Procedia 2 (2010) 159-164.

[10] J. P. Conde, V. Chu, M. F. da Silva, A. Kling, Z. Dai, J. C. Soares, S. Arekat, A. Fedorov, M. N. Berberan-Santos, F. Giorgis and C. F. Pirri, "Optoelectronic and structural properties of amorphous silicon–carbon alloys deposited by low-power electron-cyclotron resonance plasma-enhanced chemical-vapour deposition", J. Appl. Phys. 85 (1999) 3327.

[11] Z. Yin, F. W. Smith, "Tetrahedron model for the optical dielectric function of hydrogenated amorphous silicon nitride alloys", Phys. Rev. B 42 (1990) 3658.

[12] H. Richter, Z. P. Wang, and L. Ley, "The one phonon Raman spectrum in microcrystalline silicon", Solid State Commun. 39, (1981) 625.

[13] I. H. Campbell and P. M. Fauchet, "The effects of microcrystal size and shape on the one phonon Raman spectra of crystalline semiconductors", Solid State Commun. 58, (1986) 739.

[14] E. Bustarret, M. A. Hachicha, and M. Brunel, "Experimental determination of the nanocrystalline volume fraction in silicon thin films from Raman spectroscopy", Appl. Phys. Lett. 52, (1988) 1675.

[15] M. Nazrul Islam, A. Pradhan, and S. Kumar, "Effects of crystallite size distribution on the Raman-scattering profiles of silicon nanostructures", J. Appl. Phys. 98, (2005) 024309.

[16] V. G. Kravets and V. Yu. Kolmykova, "Raman scattering of light in silicon nanostructures: First-and second-order spectra", Opt. Spectrosc. 99, (2005) 68.

[17] L. V. Mercaldo, E. M. Esposito, P. Delli Veneri, G. Fameli, S. Mirabella and G. Nicotra, "First and second-order Raman scattering in Si nanostructures within silicon nitride", Appl. Phys. Lett. 97, (2010) 153112.

[18] D. Barba, F. Martin, and G. G. Ross, "Evidence of localized amorphous silicon clustering from Raman depth-probing of silicon nanocrystals in fused silica", Nanotechnology 19, (2008) 115707.

[19] F. Iacona, C. Bongiorno, C. Spinella, S. Boninelli, and F. Priolo, "Formation and evolution of luminescent Si nanoclusters produced by thermal annealing of SiO_x films", J. Appl. Phys. 95, (2004) 3723.

[20] W. J. Salcedo, F. J. Ramirez Fernandez, and J. C. Rubim, "Changes in the porous silicon structure induced by laser radiation", J. Raman Spectrosc. 32, (2001) 151.

[21] G. Scamarcio, V. Spagnolo, G. Ventruti, and M. Lugarà, "Size dependence of electron—LO-phonon coupling in semiconductor nanocrystals", Phys. Rev. B 53, (1996) R10489.

[22] N.-M. Park, C.-J. Choi, T. Y. Seong, S.-J. Park, "Quantum confinement in amorphous silicon quantum dots embedded in silicon nitride", Phys. Rev. Lett. 86, No. 7 (2001) 1355.

[23] P.A. Temple, C.E. Hathaway, "Multiphonon Raman Spectrum of Silicon", Phys. Rev. B 7, (1973) 3685.

[24] J. Bandet, B. Despax, and M. Caumont, "Nitrogen bonding environments and local order in hydrogenated amorphous silicon nitride films studied by Raman spectroscopy", J. Appl. Phys. 85, (1999) 7899.

[25] L. Dal Negro, J. H. Yi, J. Michel, L. C. Kimerling, S. Hamel, A. Williamson, G. Galli, "Light-Emitting Silicon Nanocrystals and Photonic Structures in Silicon Nitride", IEEE Journal of Selected topics in Quantum Electronics 12, (2006) 1628.

Publications and proceedings

- Emilia M. Esposito, Lucia V. Mercaldo, Paola Delli Veneri, Ettore Massera, Iurie Usatii, Carlo Privato, "Low temperature PECVD in-situ growth of silicon quantum dots in silicon nitride", Proceedings of the First Mediterranean Photonics Conference, Edizioni Giorgio Lieto, Ischia, (2008) 69-71.
- Lucia V. Mercaldo, Paola Delli Veneri, Emilia M. Esposito, Iurie Usatii, Carlo Privato, "Low temperature PECVD in-situ growth of silicon quantum dots in silicon nitride for third generation photovoltaics", Proceedings of the 23rd European Photovoltaic Solar Energy Conference (2008) 629-632.
- Lucia V. Mercaldo, Paola Delli Veneri, Emilia Esposito, Ettore Massera, Iurie Usatii, Carlo Privato, "Structural and optical properties of silicon quantum dots in silicon nitride grown in-situ by PECVD using different gas precursors", Materials Science and Engineering B 159–160 (2009) 74–76.
- Lucia V. Mercaldo, Paola Delli Veneri, Emilia Esposito, Ettore Massera, Iurie Usatii, Carlo Privato, "PECVD in-situ growth of silicon quantum dots in silicon nitride from silane and nitrogen", Materials Science and Engineering B 159–160 (2009) 77–79.
- Lucia V. Mercaldo, Emilia M. Esposito, Paola Delli Veneri, Laura Lancellotti, Carlo Privato "Investigation of thermally induced phase separation in PECVD-grown silicon nitride" Proceedings of the 24th European Photovoltaic Solar Energy Conference, Hamburg 2009.
- L. V. Mercaldo, P. Delli Veneri, E. M. Esposito, I. Usatii, and C. Privato. "PECVD in-situ growth of silicon quantum dots in dielectric matrix for third generation photovoltaics" Moldavian Journal of the Physical Sciences, Vol.8, N.2, (2009), 195-200.

- Lucia V. Mercaldo, Paola Delli Veneri, Emilia M. Esposito, and Mario Tucci "Annealing effects on $aSiN_x$ grown by PECVD using different gas mixtures" Phys. Status Solidi C 7, No. 3–4, 832–835 (2010).
- Emilia M. Esposito, Lucia V. Mercaldo, Paola Delli Veneri, Laura Lancellotti, and Carlo Privato "Annealing Effects on PECVD-grown Si rich aSiNx Thin Films" Energy Procedia 2 (2010) 159–164.
- Lucia V. Mercaldo, Paola Delli Veneri, Emilia M. Esposito, Giuseppe Fameli "Micro-Raman investigation of silicon nitride embedding Si nanostructures" Proceedings of the 25th European Photovoltaic Solar Energy Conference, Valencia 2010.
- Lucia V. Mercaldo, Emilia M. Esposito, Paola Delli Veneri, Giuseppe Fameli, Salvo Mirabella, and Giuseppe Nicotra "First and second-order Raman scattering in Si nanostructures within silicon nitride" Appl. Phys. Lett. 97, (2010), 153112.
- Lucia V. Mercaldo, Emilia M. Esposito, Paola Delli Veneri, Béchir Rezgui, Georges Bremond, "Photoluminescence properties of partially phase separated silicon nitride films", submitted to Appl. Phys. Lett.

RINGRAZIAMENTI

Per esprimere la gratitudine verso le persone del mio gruppo le parole, sicuramente, non bastano.

Voglio ringraziare il mio tutor, la Dott.ssa Lucia Mercaldo, per aver avuto fiducia in me ed avermi insegnato tanto, scientificamente ed umanamente; per essere stata sempre presente ed avermi fatto capire che le cose vanno fatte sempre con grande entusiasmo ed impegno.

Vorrei esprimere tutta la mia gratitudine per i ricercatori Paola Delli Veneri e Iurie Usatii, che mi hanno sempre aiutato in tutti i problemi scientifici e non.

Vorrei ringraziare tutte le persone del C. R. - ENEA di Portici per aver reso questi anni ancora più fruttuosi. In particolare, vorrei ringraziare, Brigida Alfano, Giuseppe Nenna, Riccardo Miscioscia, Silvia Masala, Angelica Grimaldi, Fulvia Villani e Tiziana Polichetti per avermi aiutato nei più svariati modi nel corso di questi anni.

Un doveroso grazie va poi al caro Guido Celentano per la sua costante disponibilità.

Un ultimo ma non meno importante grazie va a tutta la mia famiglia, che grazie all'appoggio e alla serenità che mi ha trasmesso ha permesso che anche questo altro traguardo fosse raggiunto, tra le mille difficoltà che si sono presentate nel corso di questi anni.

Grazie quindi di cuore a tutti coloro che, seppur per dimenticanza non sono stati nominati, hanno saputo sostenermi in ogni momento.